THÈSE EN COTUTELLE PRÉSENTÉE

POUR OBTENIR LE GRADE DE

DOCTEUR DE

L'UNIVERSITÉ DE BORDEAUX

ET DE L'UNIVERSITÉ DE MILANO-BICOCCA

École Doctorale des Sciences Physiques et de l'Ingénieur, Bordeaux

PhD School in Nanostructures and Nanotechnologies, Milan

SPÉCIALITÉ MÉCANIQUE

Par **Huu TAN NGUYEN**

Thermal Characterization of In-Sb-Te thin films for Phase Change Memory Application

Sous la direction de Prof. Jean-Luc BATTAGLIA et de Prof. Marco FANCIULLI

Soutenue le 10/07/2015

Membres du jury :

M. Marco Bernasconi	Prof des universités, Université de Milano Bicocca	Président
M. Nadjib Semmar	Prof des universités, Université d'Orléans	Rapporteur
M. Denis Rochais	Dr, HDR, CEA, Le Ripault, France	Rapporteur
Mme. Claudia Wiemer	Dr, HDR, MDM, CNR, Italie	Examinateur
M. Marco Fanciulli	Prof des universités, Université de Milano Bicocca	Examinateur
M. Jean-Luc Battaglia	Prof des universités, Université de Bordeaux	Directeur de thèse

Abstract

Phase change memories (PCM) are typically based on compounds of the Ge-Sb-Te (GST) ternary system. Nevertheless, a major drawback of PCM devices is the failure to fulfill automotive-level or military-grade requirements (125°C continuous operation), due to the low crystallization temperature of GST. To overcome this limitation, alloys belonging to the In-Sb-Te (IST) system have been proposed, which have demonstrated high crystallization temperature, and fast switching. Thermal properties of the chalcogenide alloy and of its interfaces within the PCM cell can influence the programming current, reliability and optimized scaling of PCM devices. The Modulated Photothermal Radiometry (MPTR) technique was implemented to measure the thermal conductivity of IST thin films as well as the thermal boundary resistance at the interface with other surrounding materials (a metal and a dielectric). The experiment was carried out *in situ* from room temperature up to 550^{o}C in order to investigate the intrinsic thermal properties at different temperatures and the significant structural rearrangement upon the phase transition. Two different stoichiometries for the IST ternary alloy were deposited by Metal Organic Chemical Vapor Deposition (MOCVD) on a Si substrate covered with thermal SiO_2 and then capped with a Platinum layer that acts as an optical and thermal transducer. Additional data from Raman and XRD lead to complementary analysis.

Keywords: Phase change memory, In-Sb-Te ternary, Thermal conductivity, Thermal boundary resistance.

Table of contents

Context

The aim of the present work is to measure the thermal conductivity of In-Sb-Te alloy (IST) with a varying quantity of Te. The material is deposited as a thin film using the Metal-Organic Chemical Vapour Deposition (MOCVD) technique. Changing slightly the deposition parameters leads to achieve the variation of the Te content within the alloy. We measured also the thermal boundary resistances at the interfaces between the IST layer with dielectric (SiO_2, Al_2O_3) and metallic (Pt) layers. The measurement of the thermal conductivity and TBR is performed in a broad temperature range from room temperature (RT) up to 550°C in order to follow the phase change and to observe the related variations of the measured quantities.

This work has been realized thanks to an intensive collaborative work between the I2M institute (Institut de Mécanique et d'Ingénierie de l'Université de Bordeaux, UMR CNRS 5225) and the MDM laboratory (Materials and Devices in Microelectronics, University of Milan Biccoca, CNR). This thesis has been founded thanks to a Vinci Grant from the French-Italian University.

My main contribution in this work is related to the thermal properties measurement using both the 3ω and the MPTR methods. 3ω experiments have been performed at the MDM under the supervision of Roberto Fallica and Claudia Wiemer. The MPTR experiments have been carried out at I2M under the supervision of Andrzej Kusiak. Massimo Longo, at the MDM, performed the deposition of the IST using the MOCVD process. However, this work is based not only on the measurement of the thermal properties but also on the structural and chemical analysis of the samples as a reliable way to link the measured thermal quantities with the state of matter at a given temperature. Therefore, several researchers have been involved in this study thanks to their expertise in this field. The SEM, ToF-SIMS, XRD and XRR results presented in this work have been obtained by Claudia Wiemer and Alessio Lamperti at the MDM. Raman, EDS and WDS results have been obtained by Cécile Gaborieau and Yannick Anguy at the I2M. In addition we also used the DOS calculated using the DFT method by Marco Bernasconi at the UMIB that allowed us to calculate the theoretical thermal conductivity and TBR. All those results must be viewed as a whole that lead us to analyse the IST thermal properties when varying the temperature of the sample.

Chapter 1: Phase Change Memory - From Scientific Context to Application

1.1 Introduction

Needless to say, in the modern era of high-tech devices: computer, smart phone, tablet, or even digital cameras, have become ubiquitous and almost essential components of every daily life. Their implementation requires an enormous development of new memory storage technologies to achieve more data by a single cell, thus reducing cost per bit, decreasing energy consumption and also their geometrical dimensions.

The solid-state circuits industry has grown from infancy to become one of the largest industries in the world over these last fifty years. Thanks to the accomplishment of the semiconductor industry, semiconductor memories play a crucial role in modern information processors. However, huge challenges in mass data storage are required with growing demands in density and performance. Moore's law is thus always postponed at the limited as presented in Figure 1 [1]. A huge advancement is expected for the structures to approach the range of nanometers working on nanosecond timescales. Those advancements are reached through an intensive and on-going collaboration between industry and academic research. This present work enters this category.

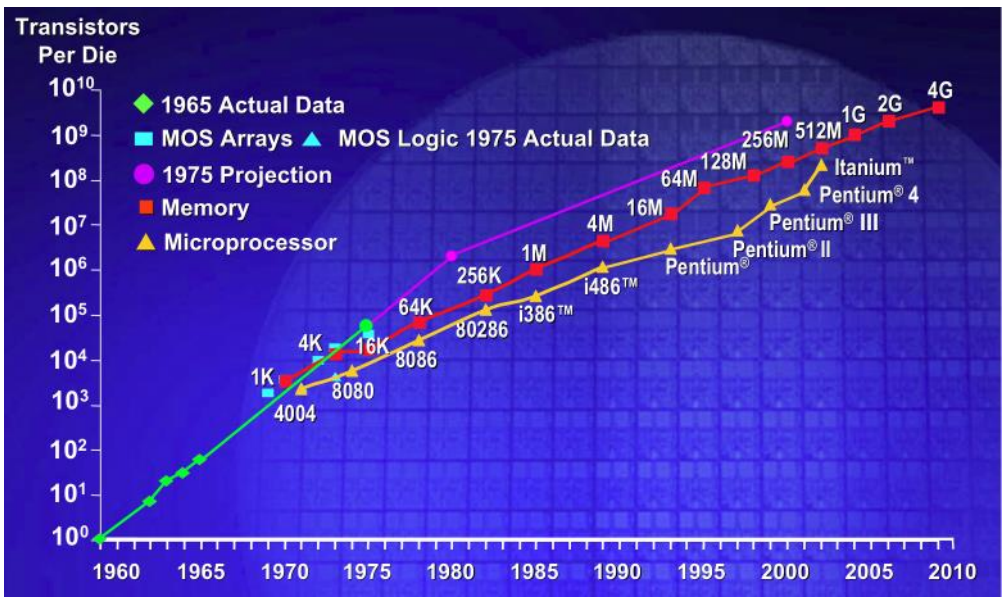

Figure 1: Plot of CPU transistor counts against dates of introduction, after [1].

1.2 Overview on Phase Change Memory

Although their commercial success remains somewhat questionable, numerous memory technologies have been competing in the field of Non Volatile Memory (NVM) market as reported in Figure 2. This specific microelectronic application is divided into two categories, namely volatile and non-volatile. Volatile memory does not retain data when power is turned off. On the contrary Non-volatile memory devices are expected to guarantee data retention along a measurable time even when power is turned off.

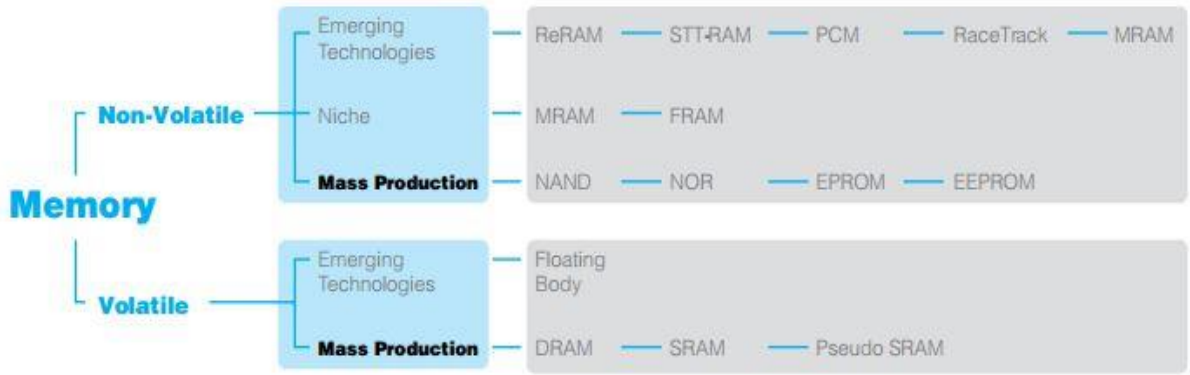

Figure 2: Memory device family (According to Viking technology)

One of the most interesting non-volatile technologies is the Phase Change Memory (PCM). As mentioned in the literature, these novel technologies offer reliable and more promising alternatives to replace Flash memory and even Double Data Rate Random Access Memory (DDR-RAM) [2]-[7]. This fact stands on the scalability of PCMs compared to MRAMs (Magnetic-RAM) and FRAMs (Ferroelectric-RAM), as reported in Table 1. PCMs have also high cycles with respect to Flash memories though the endurance is lower than in the cases of FRAM and MRAM. In addition, few mask steps are required in photolithography for film deposition in PCM technology in contrast to FRAM and MRAM technologies that require the integration of ferroelectric and magnetic materials within the Complementary Metal–Oxide–Semiconductor (CMOS). As maybe the most interesting feature, PCM increases the write speed by at least one order of magnitude compared to Flash memories. In addition PCM is suitable for very low-voltage technologies [14]. To summarize, with the performances in fast SET-RESET process, high-speed random access times, long lifetime [18][19] and potential extended scalability [20][21], PCM technology is a credible alternative to the Flash technology.

Intel-Ovonyx Corporation presented the first memory array with PCM memory cells in the early of the 2000s [15]. STMicroelectronics [16] and Samsung [17] also launched their products shortly after. Figure 3 shows an evolution of PCMs cell size as a function of year compared to the competitive Flash technology. The figure shows the first starting point in 2001 with the 180 nm technology node. The PCM cell size reached the 32 nm node in 2012 and the 16 nm technology node is expected in a very short time. An extraordinary scaling is also achievable very soon due to the income of nanowire technology thanks to the Metal Organic Chemical Vapour Deposition technique (MOCVD). Such a realization has been made at MDM laboratory in the framework of the Synapse European project. Finally, among all those promising expectations one has to emphasize the capability of PCM to store more than two levels per cell, thus giving extra options to further reduce the cost per bit [22].

	DRAM	Flash	FRAM (ferroelectric)	MRAM (magnetic)	PCM (phase change)
Relative bit size 1= DRAM cell size (~NOR Flash)	1	0.25 - 1	3 - 10	1 - 3	0.5 - 2
Relatv. mask count	1	1.1	1	1	1
Scalability	Fair	Fair	Poor	Poor	Good
Endurance	Unlimited	10^5 Block erasing	10^{10} destructive read	$>10^{14}$ Sensing critical	10^{12}
Data retention	10ms	> 10years	> 10years	> 10years	> 10years
Write time	< 100ns	µs/ms	< 100ns	< 100ns	< 100ns
Write power/B (Vxl)	3Vx100µA	5V x 1mA	3Vx100µA	1.8Vx10mA	3Vx1mA
Maturity	Volume prod.	Volume prod.	Limited prod.	Test chips	Test chips

Table 1: Non-volatile memories characteristics [2].

However, several critical issues remain to be resolved before PCM becomes fully commercially competitive. Among these, the challenge of increasing the data density in phase change cells is strongly related to the resistivity drift phenomenon. The drift is not due to cycling, but to structural relaxation of the amorphous. At each cycle the drift restarts from beginning due to the resetting of the resistance. The multi-level storage we discussed just

before seems also an interesting approach to overcome this limitation [7]. Its is not however the only one but it has the advantage to solve an issue as well as to offer a higher storage of bit without increasing the number of cell. Another issue met in PCM is the lower temperature of crystallization (150°C in case of the Ge-Sb-Te alloy) that makes the PCM misfit with applications involving high functioning temperature. This point will be one of the most interest of the present work in this thesis.

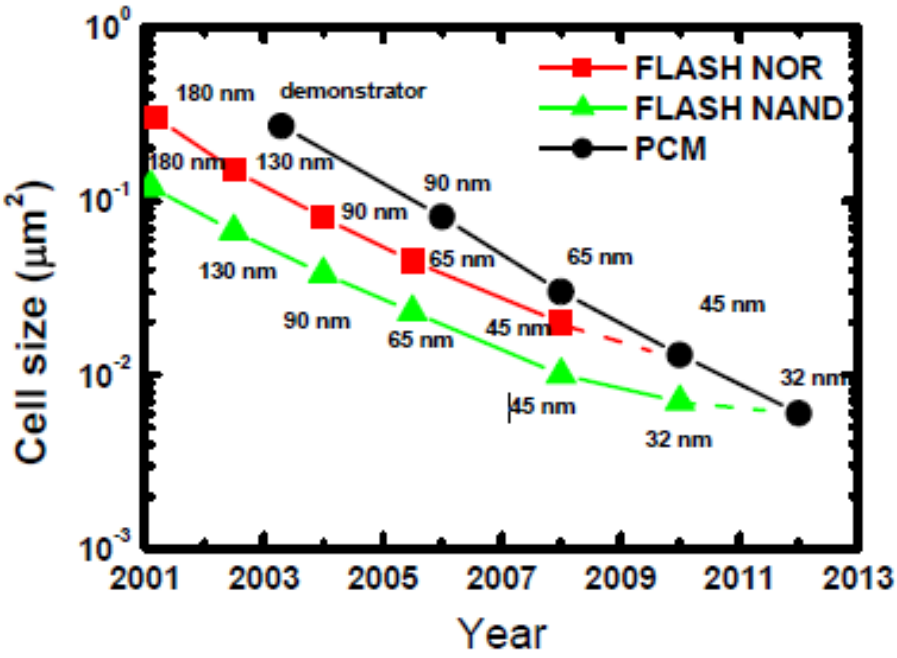

Figure 3: Scaling trends for NAND, NOR and PCM. The phase change memory technology is expected to reach the same Flash NAND size at the 32 technology feature size [18].

1.3 How does it work?

Although this is not the subject of the present work, in order to understand the key challenging issues related to the practical implementation of such materials the main principles of PCM must be presented. Phase change memory (PCM) is relying on the reversible, thermally assisted phase transitions of specific phase change materials. Stanford Ovshinsky was the first to investigate phase change alloys in the 1960s and he discovered their ability to switch between in two stable states of the matter: the amorphous and crystalline state. This process is the so-called phase tranformation. Let us remind that if a solid possesses long range, regularly repeating units, it is classified as a crystalline material. Crystalline solids are only produced when the atoms, ions, or molecules have an opportunity

to organize themselves into regular arrangements, or lattices. On the other side, if there is no long-range structural order throughout the solid, the material is best described as amorphous. The phase change is a reversible phenomenon that is achieved by stimulating the cell with suitable electrical pulses that appropriately heat the material, monitoring the phase change. We must emphasize that phase change relies on a solid-solid phase change as for instance the eutectic or eutectoid transformations in alloys. The key point is that there exists an extreme contrast, over several orders of magnitude, between amorphous and crystalline phase in terms of the electrical resistivity (a few MΩ in amorphous phase and a few kΩ in crystalline state) while the optical [9] reflectivity can change up to 30% (this discovery has been successfully exploited in rewritable optical media (CD, DVD) [10][11]). An example of the electrical resistivity change of a Ge-Sb-Te alloy with temperature, starting from the amorphous state, is represented in Figure 4. The variation lies on a logarithm scale making the resistivity to vary along several decades [13].

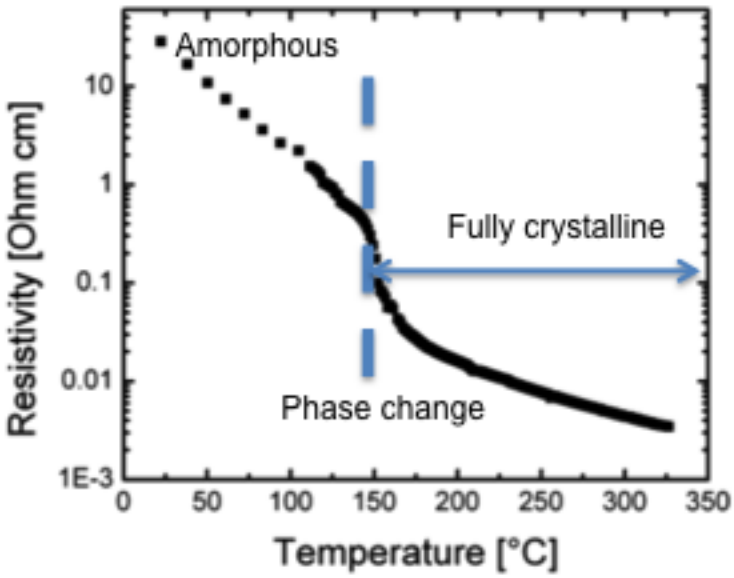

Figure 4: The Ge-Sb-Te electrical resistivity during heating at a constant heating rate of 10 ◦C · min^{-1} from the amorphous state [13].

Phase change materials are inevitably composed by chalcogenide materials that are allotropic (the property of some chemical elements to exist in two or more different forms, in the same physical state) semiconducting elements and alloys belonging to the IV, V, and VI group of the periodic classification, i.e. indium, germanium, tin, antimony, tellurium. Figure 5 shows the ternary phase diagram of the Ge-Sb-Te, In-Sb-Te, Ag-Sb-Te and Sn-Sb-Te systems.

Alloys along the pseudo-binary line between Sb_2Te_3 and GeTe with compositions $(GeTe)_m(Sb2Te3)_n$ have been intensely studied already and they have been implemented in PCM electronic devices. Among them, the $Ge_2Sb_2Te_5$ ternary is very well known and has been studied for several years also at the MDM and I2M laboratories.

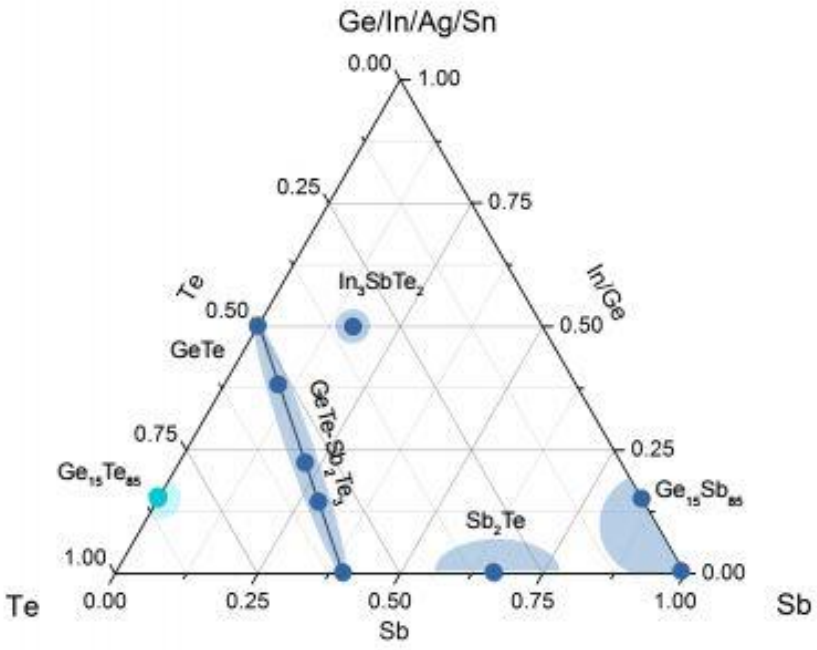

Figure 5: An overview of the phase change alloys that have been investigated using the ternary phase change diagram. It is clearly seen that the $In_3Sb_1Te_2$ (that is investigated in this thesis) shows distinctively different properties from the other alloys. Figure inspired from [37].

It must also be said that a lot of doped binary or ternary systems have been the subject of several studies. This "doping" is expected to improve some features as the switch rate and the data retention. However the term "doping" must be understood mainly as the addition of atomic elements whose some are even constituents of the alloy (as Ge for instance in case of the Ge-Te or Ge-Sb-Te systems).

The incredible electrical resistivity phase change finds its origin at the microscopic scale. Indeed, it is related to a bonding mechanism in the crystalline phase, called resonance or mesomerism) bonding by Linus Pauling. For instance, in the configuration of amorphous $Ge_2Sb_2Te_5$ system, Ge atoms can occupy both threefold and tetrahedral sites with principally covalent bonding (high electrical resistivity). When switching to the cubic crystalline phase at

150°C structure comes to octahedral sub-units described as being 'resonantly' bonded. This bonding is characterized by the fact that a single half-filled *p*-band forms two bonds to its left and right neighbours (low electrical resistivity). Nevertheless, this bonding mechanism is met only for a small subset of group V and VI compounds, which explains the limited number of possible systems, as those presented in Figure 5 [26]. A more physical interpretation of this phenomenon is given in [27] [28][29]. Such a phenomenon explains why the amorphous phase is stable for 10 years at about 100°C, while this state recrystallizes into the crystalline phase in less than 10 ns at elevated temperatures [30][31] (the fastest known switching reported in the literature is less than 1 ns [32]).

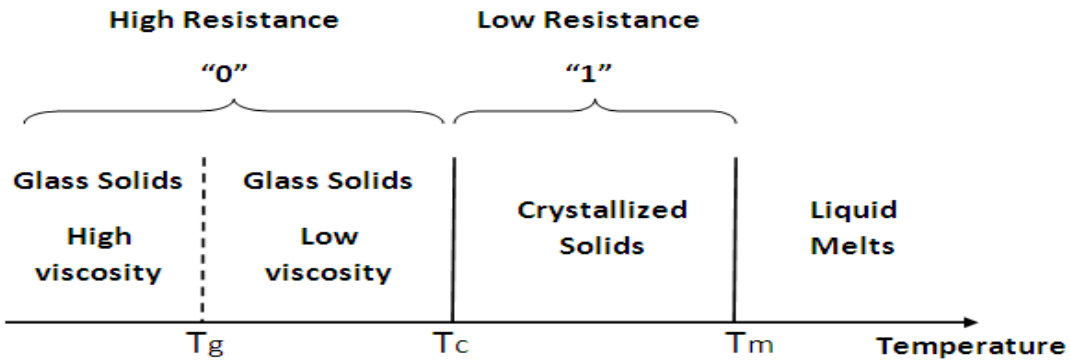

Figure 6: Three critical temperatures are observed versus temperature: glass transition temperature (T_g), crystallization temperature (T_c) and melting temperature (T_m) [23].

Figure 6 shows the three critical temperatures during the operational condition of PCMs [23]. According to its structural change, the switch from the crystalline phase to the amorphous phase is achieved through intense localized Joule heating caused by a controlled current injection making the phase change material above the melting temperature T_m followed by a fast quench. This occurs as the atomic viscosity increases and therefore the atomic mobility decreases drastically with decreasing temperature. The temperature, at which a viscosity threshold value of 10^{12} Pa.s is reached, is known as the glass transition temperature T_g. Herein, glass transition temperature is a signature of significant softening of glasses; it is measured by probing the viscosity of glasses. At this temperature the mobility of the atoms is so low in the order of timescales and would be required to induce the crystallization in the next ten years. Therefore a high T_g is required for memory applications. Alternatively heating an amorphous sample gives rise to crystallization when enough time/energy is available for

the system. As said previously, when temperature of the material is higher than the crystallization temperature T_c, crystallization can occur on very short timescales [24].

1.4 Phase Change Memory Operation

Implementation of the phase change material to achieve the phase change memory device is represented in Figure 7 a). The resistivity difference between the amorphous and the crystalline states of a chalcogenide glass is used to encode the logic '0' and '1' levels. The device consists of a top electrode, the chalcogenide phase change layer, and a bottom electrode. The heater is attached to the underside of the PCM. Heating/melting affects only a small area around the tip of the heater displayed as a mushroom.

As presented in Figure 7 b) and Figure 8, the phase change write operation consists of:

- RESET state: the chalcogenide glass is momentarily melted by a short (ns) electric pulse and then quickly quenched into amorphous solid with high resistivity
- SET state: a lower amplitude but longer pulse (>100 ns) re-crystallizes the amorphous layer back to the crystalline state with low resistance level [22],[25],[36]-[39].

The resistance state of the memory cell is read with a sufficiently small current pulse, which does not alter the state of the memory cell.

As presented in Figure 8, this change of state is only possible because of the threshold switching effect that leads, within a few nanoseconds, to a reduction of the resistance of the amorphous phase when a certain threshold field is surpassed, at a given threshold voltage V_T. Otherwise, it would be impossible to heat the amorphous material using Joule heating with reasonably low voltages.

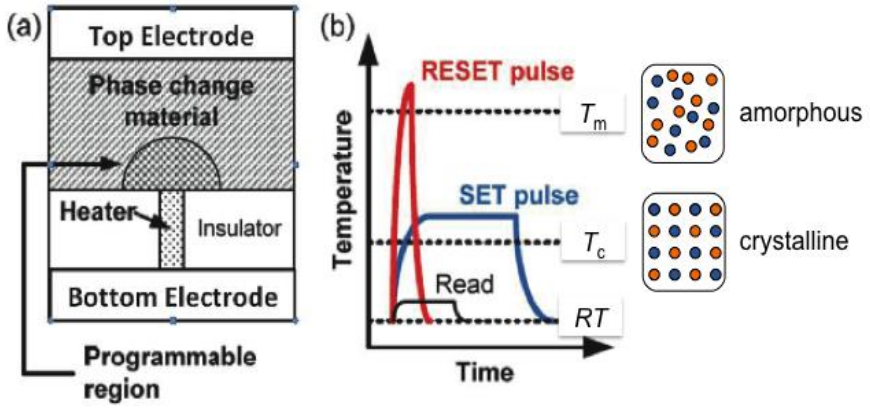

Figure 7: a) The classical implementation of the phase change material between two electrodes in a non-volatile memory cell. b) Electrical program of the cell.

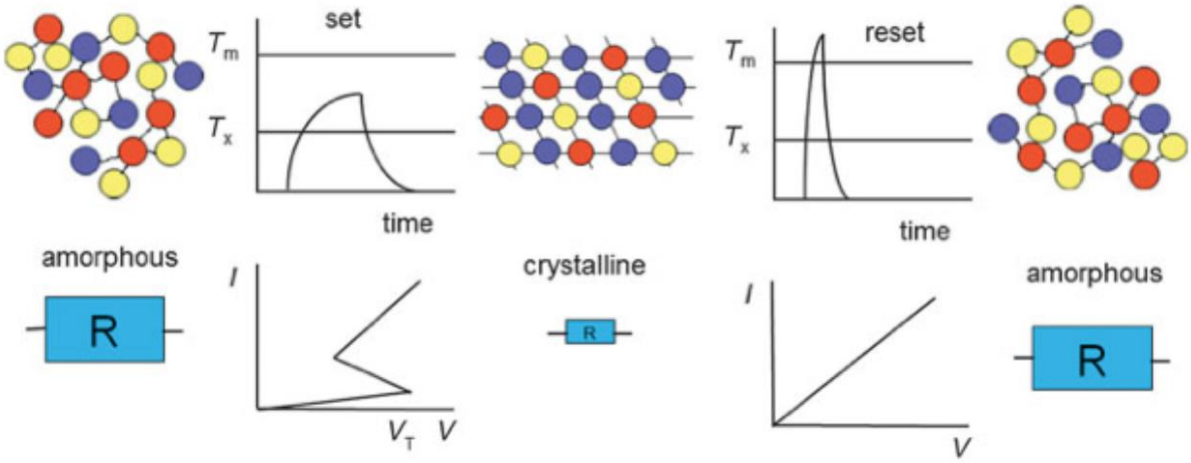

Figure 8: Electrical program of the cell. Starting from the amorphous phase with large resistance *R* (100 Ω.cm), a current pulse is applied. At the threshold voltage V_T, the resistance drops suddenly, and a large current (*I*) flows that heats the material above the crystallization temperature T_c for a sufficiently long time to crystallize (SET operation). In the crystalline state, the resistance is low (1mΩ.cm). A larger, short current pulse is applied to heat the material above the melting temperature T_m. The material is melt-quenched and returns to the amorphous, high resistance state (RESET operation). Figure comes from reference [37].

The threshold voltage in current typical PCM cells is on the order of 1 V, but if devices are scaled to much smaller dimensions, the threshold voltage scales with the size of the amorphous region, and for very small cells, it could become comparable to the read voltage such that every read operation could alter the cell state.

1.5 The In-Sb-Te alloy

One of the main issues of PCM is related to the crystallization temperature that need to be high enough in order to have a better stability of the amorphous phase, thus enabling the fulfilment of high temperature applications requirements. It has been demonstrated that doping the chalcogenide with nitrogen, oxygen, carbon and silicon markedly increased the crystallization temperature, from 150 °C of un-doped $Ge_2Sb_2Te_5$ [42], to above 290 °C [44][44]. Recent studies revealed that $In_3Sb_1Te_2$ demonstrated a high crystallization temperature (290°C) and melting temperature (626°C) [41], enhancing the stability of the amorphous phase and the data retention in phase change memory (PCM) devices for high-temperature applications; it also allows multi-bit storage in a single cell, due to intermediate

phases during operation. Therefore, a straightforward way to achieve this same purpose consists of replacing germanium with indium in the Ge-Sb-Te system. Furthermore, the IST system has the same space group number and atomic structure as the Ge-Sb-Te (GST) and it has nearly same lattice parameter (a=b=c=6.12 A° for IST and a=b=c=6.03 A° for GST). The $In_3Sb_1Te_2$ is called the 4th generation of ternary phase-change material. Interest in this alloy was renewed when Maeda *et al.* started to successfully apply this alloy in optical discs, exploiting the advantageous properties like high crystallization temperature, phase stability, short writing times and high numbers of writing cycles [46][47]. Recent interest was renewed due to the possibility of multilevel storage in In-Sb-Te alloys but also the production of nano wire via metal organic chemical vapour deposition (MOCVD) [41], [48]-[51]. The observed multi resistance states, represented in Figure 9, is due to InSb/InTe segregation [50]. The crystal structure of cubic $In_3Sb_1Te_2$ has a rocksalt geometry with In occupying the cation sub-lattice and Sb and Te atoms occupying the anion sub-lattice in a random manner as shown by recent X-ray and neutron diffraction experiments [41]. It is interesting to note that $Ge_2Sb_2Te_5$ also crystallizes in a metastable rocksalt phase in which, however, the cation sub-lattice is occupied in a random manner by Sb, Ge, and 20% of vacancies, the anionic sub-lattice being occupied by Te only. Antimony is thus cationic in $In_3Sb_1Te_2$ and anionic in $Ge_2Sb_2Te_5$. The octahedral-like bonding geometry of the cubic ternary $In_3Sb_1Te_2$ has to be contrasted with the tetrahedral bonding geometry of the binary compounds InTe and InSb. In fact, InSb crystallizes in a zinc-blende structure, while crystalline InTe is made of chains of edge-sharing $InTe_4$ tetrahedra intercalated by weakly bound, interstitial-like In ions.

(a) (b)

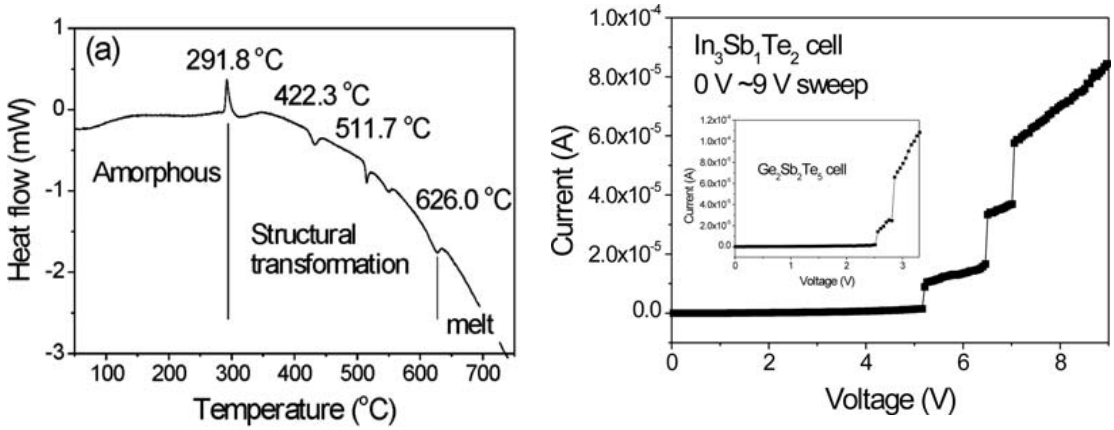

Figure 9: (a) DSC curve for the $In_3Sb_1Te_2$ ternary alloy from 100 °C to 750 °C.

Measured current versus Voltage curve of the $In_3Sb_1Te_2$ PRAM cell. The inset shows the I-V curve of the $Ge_2Sb_2Te_5$ cell. Results obtained by [41]

1.6 Thermal properties of the PCM

The functioning of PCM is a thermally assisted process. Temperature dependent thermal properties of the PCM are thus key parameters that have to be perfectly known in order to simulate the electro-thermal behaviour of the cell. Much work has been done in that sense. Since the process is time dependent, not only the thermal conductivity k but also the thermal diffusivity a or the specific heat C_p have to be measured. As everybody knows, those three parameters are linked as $a=k/C_p$. Obviously, defining the thermal conductivity means that one assumes implicitly that the mean free path (*mfp*) of the heat carriers (phonon and electrons or holes) is lower than the characteristic length of the material (the thickness in case of a film). Indeed, the thermal conductivity is a "macroscopic" parameter that allows relating the heat flux and the temperature gradient in the material. In Chalcogenides alloys, the *mfp* is very small (the order of the nanometer) at room temperature. This means that the thermal conductivity of very thin films can be rigorously defined even for films whose thickness is of the order of some tenth nanometers. One can ask therefore about the meaning of measuring the thermal conductivity on such films whereas a bulk measurement would have been easier to implement. The response is double. First, the alloys are generally deposited from specific processes as: sputtering, Atomic Layer Deposition (ALD), Chemical Vapour deposition (CVD), Metal-Organic Chemical Vapour deposition (MOCVD that will be used in this work) that do not allow depositing thick layers. Secondly, the PCM films thickness must be representative of that implemented in the memory device. This point is quite important since structural configuration of the film could be slightly modified by superimposed layers at the bottom and the top of the PCM layer. Indeed, the PCM is in contact with dielectric materials in the real device that play the role of thermal and electrical insulators (see Figure 7). The classical dielectric materials used in PCM are SiO_2, Al_2O_3 or Si_3N_4. On the other hand, the PCM layer is also in contact with metal electrodes that ensure the current to flow through the PCM. Those metallic materials are TiN or Al. The influence of the contact between layers on the thermal conductivity of the PCM layer can be viewed as an isotropy of the film with respect to the in-plane and transverse values. However, such an anisotropy has never been observed on the PCM film whatever the contact layers and the thickness of the film.

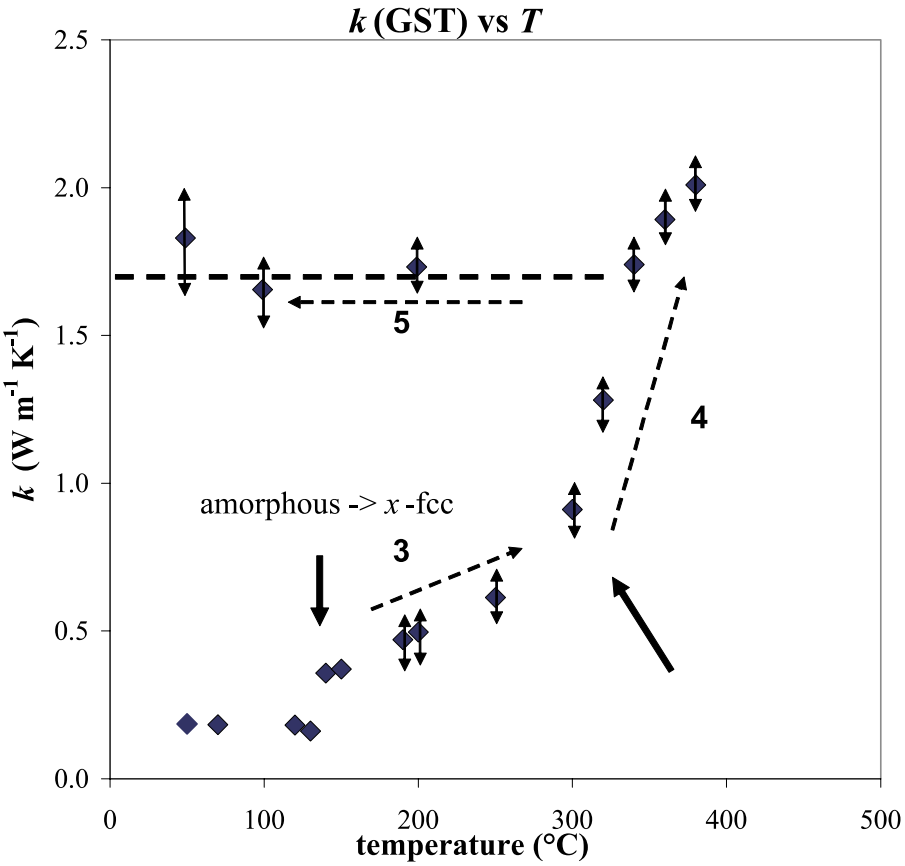

Figure 10: Measured thermal conductivity of $Ge_2Sb_2Te_5$ thin film (thickness in the 210-840 nm range) using the Modulated Photothermal Radiometry experiment [25].

In 2009, I2M and MDM published a paper about the thermal conductivity of the $Ge_2Sb_2Te_5$ starting from the amorphous state [25]. This measurement was achieved using the Modulated Photothermal Radiometry experiment and the result is reported in Figure 10. As expected the phase change occurs well at the crystallisation temperature. However, the thermal conductivity varied only from 0.18 $W.m^{-1}.K^{-1}$ in the amorphous to 0.45 $W.m^{-1}.K^{-1}$ in the *fcc* crystalline state. This change must be compared to that observed over several decades for the electrical resistivity in Figure 4. This result showed that the electronic contribution on the thermal conductivity is absolutely negligible compared to that of phonons. A second phase change occurs at 300°C that leads to the hexagonal *hcp* state where the thermal conductivity is about 1.4 $W.m^{-1}.K^{-1}$. However, this second phase change is generally not exploited in the PCM device.

It is observed that, above the crystallization temperature, an increasing glass-like dependence

of *k* is obtained which is a fingerprint of amorphous materials. This result is surprising since in highly crystalline solids at temperatures above roughly $\Theta_D/10$ (with Θ_D the Debye temperature) *k* decreases with temperature due to the onset of three-phonon processes (e.g. the well-known Umklapp phonon scattering) [53]. It is thus questionable why the thermal conductivity shows a glassy/amorphous solid temperature dependence of a, while the XRD spectrum reveals that the sample is fully crystallized. Furthermore, annealing irreversibly shifts the thermal conductivity to higher values up to 1.8 $W.m^{-1}.K^{-1}$ at 400°C.

The electronic contribution in PCM can be determined employing the Wiedemann-Franz's law, $k_e = s\, L_0\, T$ with L_0= 2.45×10^{-8} $W.K^{-2}$ the theoretical Lorenz constant. The validity of the Lorenz number was verified for GST by calculating L_0 using the procedure described in Zevalkink *et al.* [54] (a Lorenz number of 2.20×10^{-8} $W.K^{-2}$ is calculated, which is in good agreement with the theoretical L_0). After subtracting the electronic contribution, the lattice part develops a negative slope $dk/dT < 0$ around room temperature that is indicative for the onset of Umklapp scattering. Several authors suggested that intrinsic vacancies and interstitials are responsible for the thermal properties of the crystalline phase [55] [54].

The thermal resistance at the interface (TBR: thermal boundary resistance) between the PCM and surrounding materials is of higher interest than the thermal conductivity itself. Indeed, the TBR value is very close to the thermal resistance *e*/*k* of the films with thickness *e* and thermal conductivity *k*. A major attention is thus put on the measure of the TBR in the same temperature range than that of the thermal conductivity variation. In the literature, the thermal conductivity and the TBR are generally studied separately, making the relationship between both parameters rather unclear. TBR has been the subject of very advanced works in the literature. The I2M and MDM laboratories published results about the temperature dependent TBR at the interface between $Ge_2Sb_2Te_5$ and TiN (the heater in the PCM) [56] and between $Ge_2Sb_2Te_5$ and Al (metal electrode). The results are reported in Figure 11: Measurement of the temperature dependent TBR at the interface between $Ge_2Sb_2Te_5$ and TiN using the MPTR [56]. As explicated within the plots, several phenomena are responsible for the TBR change. As expected, the phase change impacts mainly the TBR. A significant parameter that allows forecasting the TBR amplitude is the Debye temperature Θ_D of the materials in contact and more generally the Density of States (DoS). The knowledge of Θ_D and the DoS are at the basis of the Diffuse Mismatch Model (DMM) that are classically used to simulate the TBR.

Additional anharmonic processes of phonons at high temperature are also identified to play a role in the decreasing of the TBR when the temperature increases. This former phenomenon is also strongly related to species diffusion that occurs at elevated temperature.

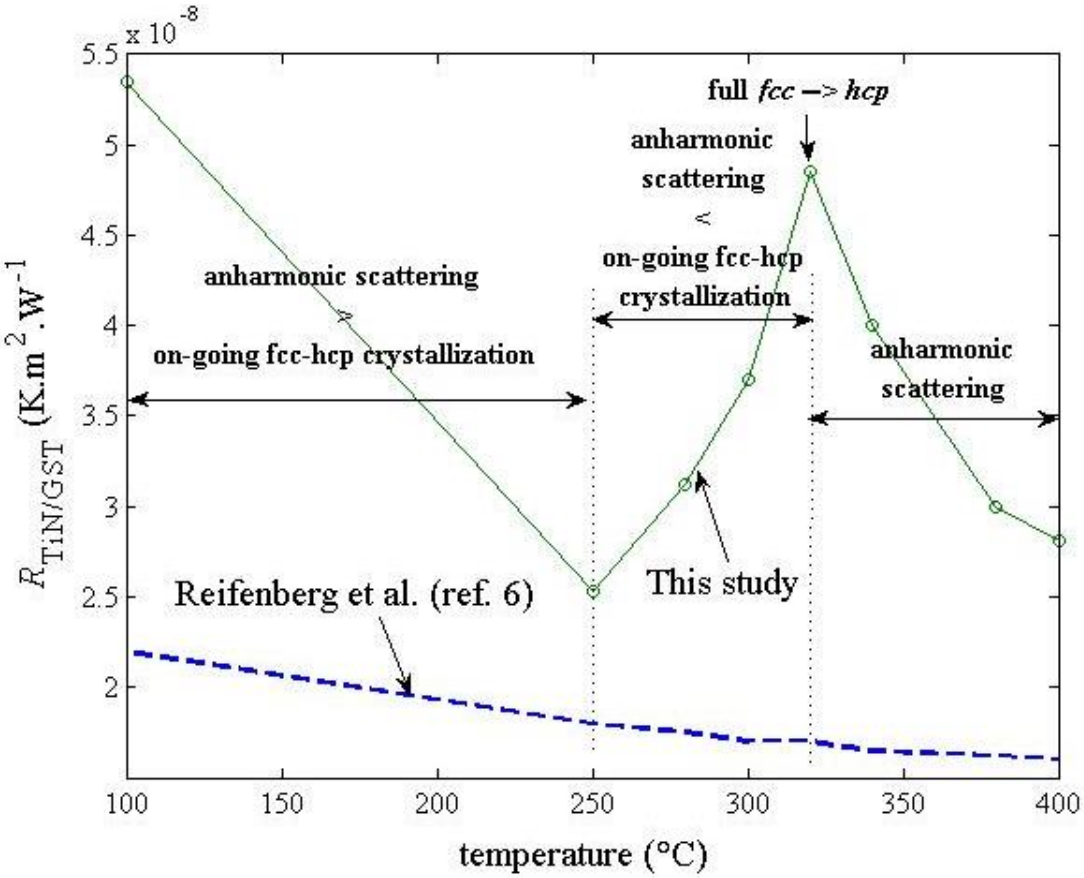

Figure 11: Measurement of the temperature dependent TBR at the interface between $Ge_2Sb_2Te_5$ and TiN using the MPTR [56].

The TBR is also very sensitive to the roughness of the interface. However, this cause is not often cited since the deposited films are very flat and the measured roughness does not vary significantly in the investigated temperature domain. Finally, the TBR appears to be very sensitive to the mechanical adhesion and more particularly the chemical bounding at the interface.

As the reader can imagine, the analysis of the varying TBR with temperature remains a very open topic. Although, significant advances have been realized in the theoretical and experimental domains. The understanding of the contribution of each phenomenon in the

TBR value remains a very complicated task despite the use of lot of experiments that allow relating the TBR to the structural and chemical configuration of the interface.

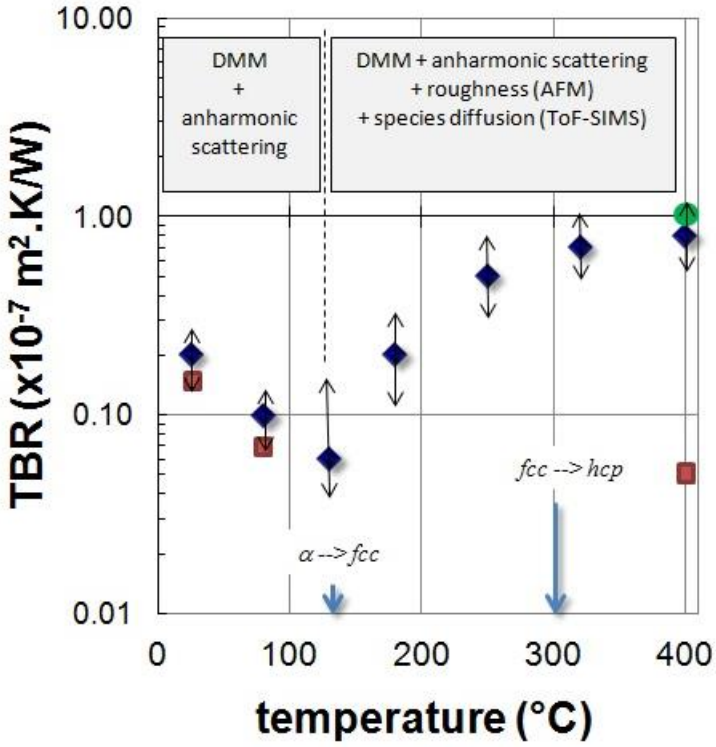

Figure 12: Measurement of the TBR at the interface at the interface between $Ge_2Sb_2Te_5$ and Al using the Time Resolved Thermoreflectance [57].

1.7 Objectives of this research work

The aim of the present work is to measure the thermal conductivity of In-Sb-Te alloy (IST) with a varying quantity of Te. The material is deposited as a thin film using the Metal-Organic Chemical Vapour Deposition (MOCVD) technique. Changing slightly the deposition parameters leads to achieve the Te variation within the alloy. We measured also the thermal boundary resistances at the interfaces between the IST layer with dielectric (SiO_2, Al_2O_3) and metallic (Pt) layers. The measurement of the thermal conductivity and TBR is performed in a broad temperature range from room temperature (RT) up to 550°C in order to have the phase change occurring at the expected temperature and to obverse related variations of the measured quantities.

In this present work, the 3ω contact method and the Modulated Photothermal Radiometry (MPTR) contactless method have been used to carry out an estimation of the IST thermal conductivity as well as the thermal boundary resistance at the interfaces with neighbourhood

layers at the bottom and the top. One can ask why using both 3ω and MPTR? The answer is first because both methods were available at the MDM and the I2M and that they will lead to compare the same physical quantity reached using two different experimental methods. As we said, the 3ω technique deals with absolute values of the temperature and the heat flux. It is thus fully consistent with the thermal conductivity measurement. However, this method is not suited to work with high temperature since the third harmonic becomes undetectable behind that of the first harmonic. On the other hand, the contact method at high temperature becomes really challenging since thermal expansion and temperature dependent hardness come into the game. Using the MPTR experiment, only the first harmonic is considered.

In chapter 2, we present the experimental thermal methods we have used in this work, namely the 3ω and the MPTR. Both lead to measure the same quantity, i.e., the thermal resistance of the deposited films on the silicon substrate. From this measure, it will be possible to extract both the thermal conductivity and the TBR providing several samples with different thickness of the PCM are available.

In chapter 3, the heat transfer model is solved for both the 3ω and MPTR experiments. The solution allows relating the measured quantity to the unknown thermal properties. In this chapter we use abundantly of the integral transforms techniques that are well suited in order to reach analytical solutions. Obviously those solutions stand on assumptions that are presented and comforted. Finally, the classical inverse problem is solved using a non-linear least square algorithm, which allows identifying the unknown thermal resistance.

The chapter 4 is the core of this work. First, thermal conductivity and TBR have been measured using the 3ω method. The samples were measured at room temperature and then annealed at 480°C. Electrical resistivity measurements of the IST have also been performed. The interface between IST and dielectric layers as silicon dioxide, silicon nitride and alumina was also analysed. The 3ω method being not well designed to deal with in-situ temperature variation of the sample, we applied the MPTR with a [RT-550°C] temperature range variation of the sample. As it will be seen, results do not differ significantly from those obtained using the 3ω on annealed samples. A model for both the thermal conductivity and the thermal boundary resistance will be proposed that will help us to understand better the possible raisons for a significant difference with experimental data. Additional details from the chemical and structural characterization led to a better understanding of the phenomenon that occurs during the thermal processing. Therefore, additional measurements (XRD, Tof-

SIMS, Raman, EDS) have been performed that allowed us to better link the thermal properties to the material state at a given temperature.

1.8 References

[1] http://hightechforum.org/100-years-of-moores-law/

[2] M. Wuttig and N. Yamada, *Phase-change materials for rewriteable data storage*, Nature materials **6** (11), 824–832 (2007).

[3] S. Lai and T. Lowrey, *OUM-A 180 nm Non-Volatile Memory Cell Element Technology For Stand Alone and Embedded Applications*, International Electron Devices Meeting, 803–808 (2001).

[4] G. W. Burr, *Overview of candidate device technologies for storage – class memory*, IBM Journal of Research and Development **52**, 449–464 (2008).

[5] F. Bedeschi, R. Fackenthal, C. Resta, E. Donze, M. Jagasivamani, E. Buda, F. Pellizzer, D. Chow, A. Cabrini, G. Calvi, and Others, *A bipolar-selected phase change memory featuring multi-level cell storage*, IEEE Journal of Solid-State Circuits **44**, no. 1, 217–227 (2008).

[6] D. Lencer, M. Salinga, M. Wuttig, I. Physikalisches, and I. Ia, *Design Rules for Phase- Change Materials in Storage Applications*, Advanced Materials **23**, no. 18, 2030– 2058 (2011).

[7] H. – S. - P. Wong, S. Raoux, S. Kim, J. Liang, J. P. Reifenberg, B. Rajendran, M. Asheghi, and K. E. Goodson, *Phase change memory*, Proceedings of the IEEE, **98**, 2201–2227 (2010).

[8] A. L. Lacaita, D. Ielmini, D. Mantegazza,"Status and challenges of phase change memory modeling", *Solid-State Electronics* **52**, 1443–1451 (2008).

[9] W. Wełnic and M. Wuttig, *Reversible switching in phase-change materials*, Material today **11**, no. 6 (2008).

[10] N. Yamada, *Rapid phase-transition of GeTe–Sb_2Te_5 pseudo binary amorphous thin films for an optical disk memory*, J Appl. Phys. **69**(5), 2849 (1991).

[11] A. V. Kolobov, P. Fons, A. I. Frenkel, A. L. Ankudinov, J. Tominaga, U. Tomoya, *Understanding the phase-change mechanism of rewritable optical media*, Nature Mater **3**:703–8 (2003).

[12] R. Bez, *Chalcogenide PCM: a Memory Technology for Next Decade*, Numonyx, IEDM09-90 (2009).

[13] R. Fallica, J.-L. Battaglia, S. Cocco, C. Monguzzi, A. Teren, C. Wiemer, E. Varesi, R. Cecchini, A. Gotti, and M. Fanciulli, *Thermal and Electrical Characterization of Materials for Phase-Change Memory Cells*, J. Chem. Eng. Data **54**, 1698–1701 (2009).

[14] S. Braga, Characterization and modeling of Phase change memories, *Thesis in Microelectronics*, University of Pavia, Italy, Academic Year 2009/2010.

[15] S. Lai and T. Lowrey, *OUM - A 180 nm nonvolatile memory cell element technology for stand-alone and embedded applications*, IEDM Tech. Dig., 803–806 (2001).

[16] F. Pellizzer et *al*., *Novel μ-trench phase-change memory cell for embedded and stand-alone non-volatile memory applications*, Symp. on VLSI Tech., pp. 18-19, 2004.

[17] Y N Hwang et *al*., *Full integration and reliability evaluation of phase-change RAM based on 0.24 mm-cmos technologies*, Symp. VLSI Tech., pp. 173–174 (2003).

[18] A. Pirovano, A. Redaelli, F. Pellizzer, F. Ottogalli, D. Ielmini, A. L. Lacaita, and R. Bez, *Reliability study of phasechange nonvolatile memories*, Trans. Mat. Rel., pp. 422–427, 2004.

[19] K Kim et *al*., *Reliability Investigations for Manufacturable High Density PRAM*, IRPS Tech. Dig., pp. 157–162, 2005.

[20] A. Pirovano, A. L. Lacaita, A. Benvenuti, F. Pellizzer, S. Hudgens, and R. Bez, *Scaling analysis of phase-change memory technology*, IEDM Tech. Dig., pp. 699–702, 2003.

[21] S. Lai, *Current status of phase change memory and its future*, IEDM Tech. Dig., pp. 255–258, 2003.

[22] A. L. Lacaita, *Progress of Phase Change Non Volatile Memory Devices*, Department of Electronics and Information, Politecnico di Milano (invited paper).

[23] F. Wang and X. Wu, *Non-volatile Memory Devices Based on Chalcogenide Materials*, 2009 Sixth International Conference on Information Technology: New Generations.

[24] G. Bruns, P. Merkelbach, C. Schlockermann, M. Salinga, M. Wuttig, T. D. Happ, J. B. Philipp, and M. Kund, “Nanosecond switching in GeTe phase change memory cells,” *Applied Physics Letters*, vol. 95, no. 4, p. 043108, 2009.

[25] J.-L. Battaglia, A. Kusiak, V. Schick, A. Cappella, C. Wiemer, M. Longo, and E. Varesi,“Thermal characterization of the SiO2-Ge2Sb2Te5 interface from room temperature up to 400 °C”, *Journal of Applied Physics* 107, 044314 (2010).

[26] D. Lencer, M. Salinga, B. Grabowski, T. Hickel, J. Neugebauer, M. Wuttig, *Nat. Mater.* **7**, 972 (2008).

[27] J. Kalb, M. Wuttig, F. Spaepen, *J. Mater. Res.* **22**, 748 (2007).

[28] J. Orava, A.L. Greer, B. Gholipour, D.W. Hewak, C.E. Smith, *Nat. Mater.* **11**, 279 (2012).

[29] M. Salinga, E. Carria, A. Kaldenbach, M. Börnhöfft, J. Benke, J. Mayer, M. Wuttig, *Nat. Commun.* **4**, 2371 (2013).

[30] G. Bruns, P. Merkelbach, C. Schlockermann, M. Salinga, M. Wuttig, T. D. Happ, J. B. Philipp, M. Kund, *Appl. Phys. Lett.* **95**, 043108 (2009).

[31] W. J. Wang, L. P. Shi, R. Zhao, K. G. Lim, H. K. Lee, T. C. Chong, Y. H. Wu, *Appl. Phys. Lett.* **93**, 043121 (2008).

[32] D. Loke, T. H. Lee, W. J. Wang, L. P. Shi, R. Zhao, Y. C. Yeo, T. C. Chong, S.R. Elliott, *Science* **336**, 1566 (2012).

[33] D. Ielmini, Y. Zhang, *J. Appl. Phys.* **102**, 054517 (2007).

[34] A. Capelli, E. Piccinini, F. Xiong, A. Behnam, R. Brunetti, M. Rudan, E. Pop, C. Jacoboni, *Appl. Phys. Lett.* **103**, 083503 (2013).

[35] P. Rausch, Thesis "Investigations of binary and ternary phase change alloys for future memory applications", University of Aachen, 2012.

[36] S. Raoux *et al.* "Phase change materials and their application to random access memory technology" *Microelectronic Engineering* 85 (2008) 2330–2333.

[37] S. Raoux, F. Xiong, M. Wuttig, and E. Pop, *Phase change materials and phase change memory*, MRS BULLETIN **39**, 703-710, (2014)**.**

[38] H.- S. Philip Wong, S. Raoux, S. B. Kim, J. Liang, J. P. Reifenberg, B. Rajendran, M. Asheghi, and K. E. Goodson, "Phase Change Memory" *Invited Paper* @2010 IEEE.

[39] G. W. Burr *et al.*, Phase change memory technology, *American Vacuum Society*, J. Vac. Sci. Technol. B 28 (2), Mar/Apr 2010.

[40] R. Fallica, Thesis on "Characterization of Chalcogenide Phase Change Nanostructures", *University of Milano-Bicocca*, 2011.

[41] E. T. Kim, J. Y. Lee, and Y. T. Kim, *Investigation of electrical characteristics of the In3Sb1Te2 ternary alloy for application in phase-change memory*, Phys. Status Solidi RRL **3**, No. 4, 103–105 (2009).

[42] F. Pellizzer, A. Pirovano, F. Ottogalli, M. Magistretti, M. Scaravaggi, P. Zuliani, M. Tosi, A. Benvenuti, P. Besana, S. Cadeo, T. Marangon, R. Morandi, R. Piva, A. Spandre, R. Zonca, A. Modelli, E. Varesi, T. Lowrey, A. Lacaita, G. Casagrande, P. Cappelletti, and R. Bez, Symposium on VLSI Technology, 18 (2004).

[43] S. Privitera, E. Rimini, C. Bongiorno, A. Pirovano, and R. Bez, Nucl. Instrum.Methods Phys. Res. B 257, 352 (2007).

[44] E. Carria, A. M. Mio, S. Gibilisco, M. Miritello, M. G. Gri- maldi, and E. Rimini, Electrochem. Solid-State Lett.14, H124 (2011).

[45] J. Woolley, C. Gillett, and J. Evans, *Some electrical and optical properties of InSb-In_2Te_3InSb-In_2Te_3 alloys*, Journal of Physics and Chemistry of Solids **16**, 138–143 (1960).

[46] Y. Maeda, H. Andoh, I. Ikuta, and H. Minemura, *Reversible phase-change optical data storage in InSbTe alloy films*, Journal of Applied Physics **64**, no. 4, 1715– 1719 (1988).

[47] Y. Maeda, I. Ikuta, H. Andoh, and Y. Sato, *Single-beam overwrite with a new erase mode of In3SbTe2 phase-change optical disks*, Japan. J. Appl. Phys. **31**, pp. 451–455 (1992).

[48] Y. I. Kim, E. T. Kim, J. Y. Lee, Y. T. Kim, *Microstructures corresponding to multilevel resistances of In3Sb1Te2 phase change memory*, Applied Physics Letters **98**, no. 9, 091915 (2011).

[49] J. Ahn, K. Park, H. Jung, S. Pammi, S. Hur, and S. Yoon, *Phase Change Memory using InSbTe Chalcogenide Materials Deposited by Metal-organic Chemical Vapor Deposition*, ECS Transactions **25**, no. 8, 1129–1133 (2009).

[50] J.- K. Ahn, K. - W. Park, H. -J. Jung and S. - G. Yoon, *Phase change InSbTe nanowires grown in situ at low temperature by metal-organic chemical vapor deposition*, Nano letters **10**, no. 2, 472–477 (2010).

[51] J. -K. Ahn, K. -W. Park,S. -G. Hur, C. -S. Kim, J.-Y. Lee, S. G. Yoon, *Structural Properties of Phase-Change InSbTe Thin Films Grown at a Low*

Temperature by Metalorganic Chemical Vapor Deposition, Journal of Nanoscience and Nanotechnology **11**, 189–194 (2011).

[52] N. Miao, B. Sa, J. Zhou, Z. Sun, A. Blomqvist, R. Ahuja, *First principles investigation on the phase stability and chemical bonding of InSb-InTe phase-change random alloys*, Solid State Communications **150**, 1375–1377 (2010).

[53] T. M. Tritt, 2004, Thermal Conductivity (New York: Plenum)

[54] Siegrist T, Jost P, Volker H, Woda M, Merkelbach P, Schlockermann C and Wuttig M, *Disorder-induced localization in crystalline phase-change materials*, Nature Mater. 10202–8 (2011).

[55] Lyeo H - K, Cahill D G, Lee B - S, Abelson J R, Kwon M-H, Kim K-B, Bishop S G and Cheong B, *Thermal conductivity of phase-change material $Ge_2Sb_2Te_5$*, Appl. Phys. Lett. **89**, 151904 (2006).

[56] J.-L. Battaglia, A. Kusiak, A. Saci, R. Fallica, A. Lamperti, C. Wiemer, *Effect of a thin Ti interfacial layer on the thermal resistance of $Ge_2Sb_2Te_5$-TiN stack*, Appl. Phys. Lett. **105**, 121903, (2014).

[57] J.-L. Battaglia, V. Schick, C. Rossignol, A. Kusiak, I. Aubert and C. Wiemer, *Thermal resistance at Al-$Ge_2Sb_2Te_3$ interface*, Appl. Phys. Lett. **102**, 181907 (2013).

Chapter 2: Thermal characterization of IST thin films

2.1 Introduction

The thermal characterization of materials for microelectronics, like those used in PCRAM, requires the use of methods well adapted to the dimensions of the studied devices (sub-micron scale). Moreover, the applied method must be used in environmental conditions that meet the device (material) during functioning (In the present work, temperature is assume to go up to 600°C). The literature presents many methods for metrology of thermal properties based on transient heat transfer in frequency or time domain. Each method is characterized by its spatial resolution that can be evaluated by the thermal diffusion length l_h. The thermal diffusion length is a function of the thermal diffusivity a of the investigated material and the temporal resolution of the used method $\tau = 1/f$ as: $l_h = \sqrt{at/p}$

Therefore, the low frequency methods (kHz-MHz) are well adapted for measuring the thermal resistance of thin films, while metrology using high frequencies will lead to the thermal diffusivity and the thermal boundary resistances (TBR) between the layers. Several methods could be thus adapted for thermal characterization of IST materials studied in this work.

Two main categories of techniques can be distinguished, the contact and contactless methods. The most-well known of them are listed in the Table 2. In a general manner, all the methods are based on the response to a thermal disturbance of the initial state of the investigated material (see Figure 13). This disturbance must be small enough in order to fulfill the linearity requirement whatever the initial temperature of the material. This disturbance will generate a temperature gradient in the material. Assuming the validity of the Fourier law, the thermal conductivity will link this temperature gradient to the disturbance, which is always a heat flux. One requirement is therefore to ensure a uniform initial state all over the material before the application of the disturbance.

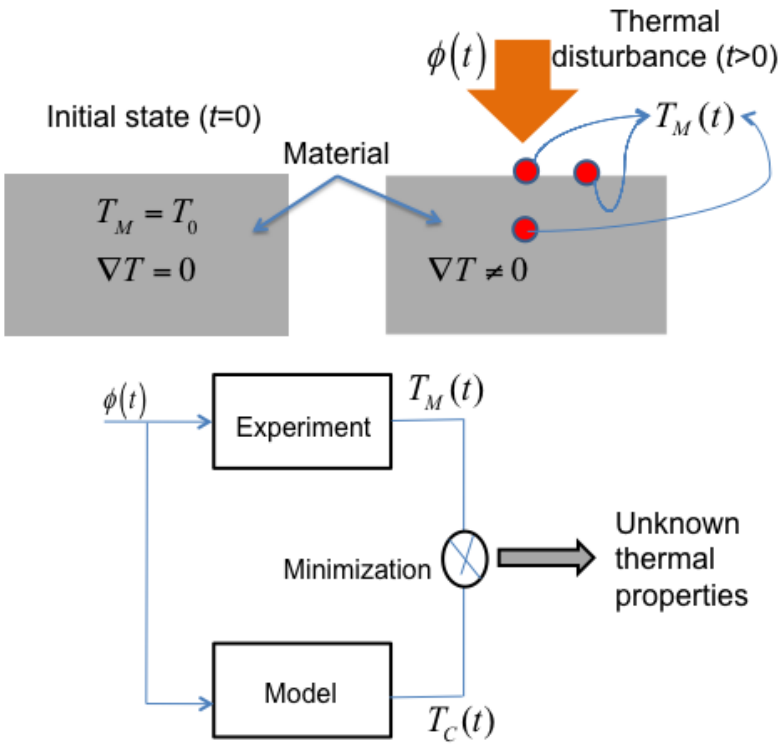

Figure 13: the basic principle in thermal characterization of materials.

Method	$\tau(s)$	$f(Hz)$	$l_h(m)$	Physical quantity linked with temperature	Contact
3ω	$10^{-5}-10^{-4}$	$10^{4}-10^{5}$	10^{5}	Electrical Resistance	YES
SThM	$10^{-5}-10^{-4}$	$10^{4}-10^{5}$	10^{5}	Electrical Resistance	YES
Radiometry	10^{-6}	10^{6}	10^{-7}	Emitted IR	NO
Thermoreflectometry	$10^{-12}-10^{-9}$	$10^{9}-10^{12}$	10^{-9}	Optical Reflectivity	NO

Table 2: The four well-known techniques to measure the thermal properties of thin films; $l(m)$ has been calculated by using a value of the thermal diffusivity in the 10^{-5}-10^{-4} $m^2.s^{-1}$ range.

In this work, two methods have been used to measure the temperature dependent thermal conductivity of thin IST films and related TBRs.

The first method, available at the MDM lab, is the 3-omega (3ω) method. This method is designed to work at room temperature only (or low temperature). In other words, this contact technique is not well appropriated to high temperature since it is based on the electrical resistivity change of the sensitive element. On the other hand, this is a contact method that leads to accurately measure the heat flux and the temperature of the sensitive element.

The second method is the modulated photothermal radiometry (MPTR) available at I2M lab. This is a contactless method that allows working at high temperature (up to 1000°C). However, it is almost impossible to measure the imposed heat flux as well as the temperature on the heated area.

Both techniques are known as front face methods, meaning that the temperature variation induced by the disturbance is monitored on the same surface of application of the disturbance. Moreover, with these methods the temperature is monitored exactly at the same location of the heat flux on the surface. Finally, the two methods are working in the frequency domain, that is known to be very accurate but also more time consuming with regards to the transient technique (flash for instance).

2.2 Description of the 3ω method

The 3ω method has been developed for measuring the thermal conductivity of thin films on a substrate (see references [1] to [6]). Further it has been also applied to measure the thermal conductivity and specific heat of bulk or thicker layers [7]. Up to recently, this method has been reexamined and improved from both the theoretical and experimental point of view, see references [8] to [13].

The 3ω method is based on the measurement of a periodic thermal response consequently to a modulated heat flux.

The method requires depositing a thin (200 to 300 nm) metallic strip onto the thin film surface. This narrow strip acts as both a heater and a temperature sensor. The strip has a special 4 points configuration as depicted in Figure 14. In case of electrically conductive films, the strip must be isolated from the film by depositing first a dielectric thin layer (SiO_2 for instance).

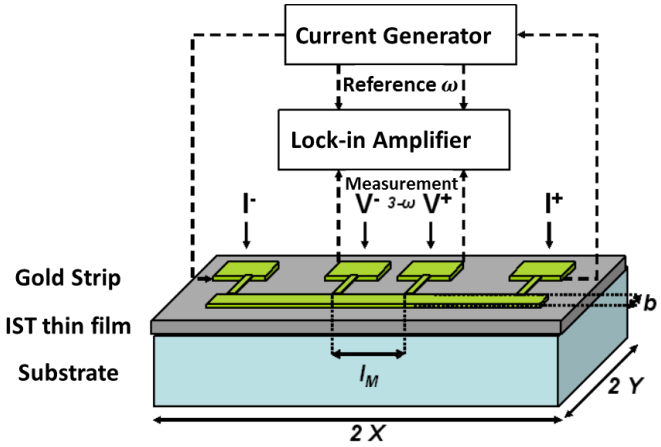

Figure 14: Layout of the 3 omega measurements

As represented on the figure, the sensitive element (the strip) is composed by two electrodes (I^- and I^+) that allow heating the film by Joule effect when an AC current generator supplied the current:

$$i = i_0 \cos(\omega t) \tag{2.1}$$

The heating coming from Joule effect is at frequency 2ω. The generated heat power (heat flux) is thus:

$$\begin{aligned} P &= r\,i^2 = r\,i_0^2 \cos^2(\omega t) \\ &= \frac{r\,i_0^2}{2}\left(1+\cos(2\omega t)\right) = P_{2\omega}\left(1+\cos(2\omega t)\right) \end{aligned} \tag{2.2}$$

In this relation, r is the electrical resistance of the strip between the two inner pads (V^+, V^-). The power P is the heat flux applied to the sample on the whole surface at the bottom of the metallic strip. Assuming the disturbance is small enough to ensure the linear heat transfer in the material, the average temperature rise of the strip is expressed as:

$$\Delta T = \Delta T_0 + \Delta T_{2\omega}\cos(2\omega t + \varphi) \tag{2.3}$$

The electrical resistance of metals varies with temperature as:

$$r = r_0\left(1+\alpha\,\Delta T\right) \tag{2.4}$$

The parameter $a = (1/r)\mathrm{d}r/\mathrm{d}T$ is the temperature coefficient of the electrical resistance. Therefore, the voltage measured between the two pads (V^+, V^-) is:

$$\begin{aligned} V &= r\,i = r_0\left(1+a\,\Delta T\right) i_0 \cos\left(\omega t\right) \\ &= r_0\left(1+a\left(\Delta T_0 + \Delta T_{2\omega}\cos\left(2\omega t+\varphi\right)\right)\right) i_0 \cos\left(\omega t\right) \\ &= r_0\, i_0 \cos\left(\omega t\right)\left(1+a\,\Delta T_0\right) + \frac{a\, r_0\, i_0}{2}\Delta T_{2\omega}\cos\left(\omega t+\varphi\right) + \frac{a\, r_0\, i_0}{2}\Delta T_{2\omega}\cos\left(3\omega t+\varphi\right) \\ &= V_0\cos\left(\omega t\right)\left(1+a\,\Delta T_0\right) + V_{1\omega}\cos\left(\omega t+\varphi\right) + V_{3\omega}\cos\left(3\omega t+\varphi\right) \end{aligned} \tag{2.5}$$

The first term of the previous equation gives no information on $\Delta T_{2\omega}$. In the second term, $\Delta T_{2\omega}$ appears but it is at the same frequency as in the first term, making the discrimination $\Delta T_{2\omega}$ impossible. Only the third harmonic permits to measure the amplitude and the phase of $\Delta T_{2\omega}$ as:

$$\Delta T_{2\omega} = \frac{2}{a\, r_0\, i_0} V_{3\omega} = \frac{2}{a}\frac{V_{3\omega}}{V_0} \tag{2.6}$$

The main difficulty to overcome in the method is the measurement of $V_{3\omega}$ that is very low compared to V_0, which implies the use of a differential stage that allow decreasing the first harmonic before entering a lock-in amplifier seeking the third harmonic of the signal (see Figure 15).

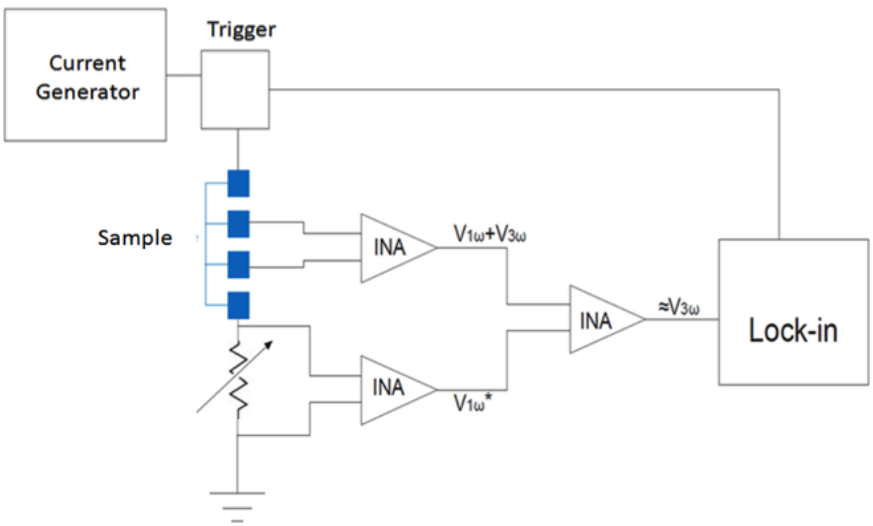

Figure 15: The differential stage and the lock-in for the 3ω setup.

The determination of α is done by a preliminary calibration step and was measured as 2.7x10^{-3} Ω.K. The resistance of the strip at room temperature was also measured as r_0 = 12 Ω.

The method is rather limited to low frequency since the sensitivity of $\Delta T_{2\omega}$ decreases exponentially with frequency (see next chapter). The main advantage of this method is the possibility of measuring the absolute temperature rise and the heat flux dissipated in the material. Even if the temperature increase remains low (below 1 K in practice) it is measurable [3]. However, the use of a metallic strip involves an additional interface and thus a thermal boundary resistance that is difficult to differentiate from the thermal boundary resistance between the deposit and the substrate.

2.3 Photothermal Radiometry technique

2.3.1 Principle

The Photothermal Radiometry method is a contactless and thus non-destructive measurement technique designed for the thermal characterization of various types of materials and thin films. It is based on monitoring the emitted infrared radiation from the surface of the sample consequently to a photothermal excitation provided by a laser.

Photothermal Radiometry is a method originally proposed by Cowan [15] and fully developed by Nordal in 1979 [16]. The principle is based on using a transient thermal excitation from a photothermal laser source. This excitation can be pulsed [17], periodic [18] or with random waveform [19] [19]. The spatial distribution of the excitation can be uniform or with more complex form (Gaussian for example). The radiation from the photothermal source is absorbed by the surface of the sample, if opaque, being at thermal equilibrium state at temperature T_0. This results in an increase of the temperature ΔT everywhere in the sample and more specifically at the surface leading to a heat flux that is emitted in the form of a thermal radiation as a function of surface temperature T. This phenomenon can be explained by Stephan-Boltzmann's law such as the total and hemispherical emittance is related to the surface temperature as:

$$M = \varepsilon \sigma_s T^4 \tag{2.7}$$

In this relation ε is the total and hemispherical emissivity of the surface and σ_s =5.67x10^{-8} W.m^{-2}.K^{-4} is the Stephan-Boltzmann constant. The heat flux is periodic as:

$$j = j_0 \cos(2\pi f t) = j_0 \cos(\omega t) \tag{2.8}$$

The temperature is expressed as the sum of the initial temperature and the temperature increase:

$$T = T_0 + \Delta T \tag{2.9}$$

Hence:

$$M = M_0 + \Delta M = \varepsilon \sigma_s (T_0 + \Delta T)^4 \tag{2.10}$$

Assuming a weak enough disturbance φ_0, then the temperature variation is also small (a few Kelvin) and the variation of emittance is linked to the temperature variation as:

$$\Delta M \approx 4 \varepsilon \sigma_s T_0^3 \Delta T \tag{2.11}$$

Finally, the variation of surface temperature ΔT varies linearly with the variation of the emittance ΔM.

The temperature change on the sample surface measured by photothermal radiometry is very low (~ 1 K) and the electrical signal related to the IR detector is in general very noisy. The measured voltages are usually very weak and embedded in noise (<1 mV for a signal to noise ratio of 1/1000). The observed data analysis is rather well adapted for the frequency domain than for the time domain. Therefore, a lock-in amplifier is implemented in order to measure the amplitude and the phase between the photothermal excitation and the measured IR variation (ΔM linked with ΔT) at the surface as shown in the Figure 16.

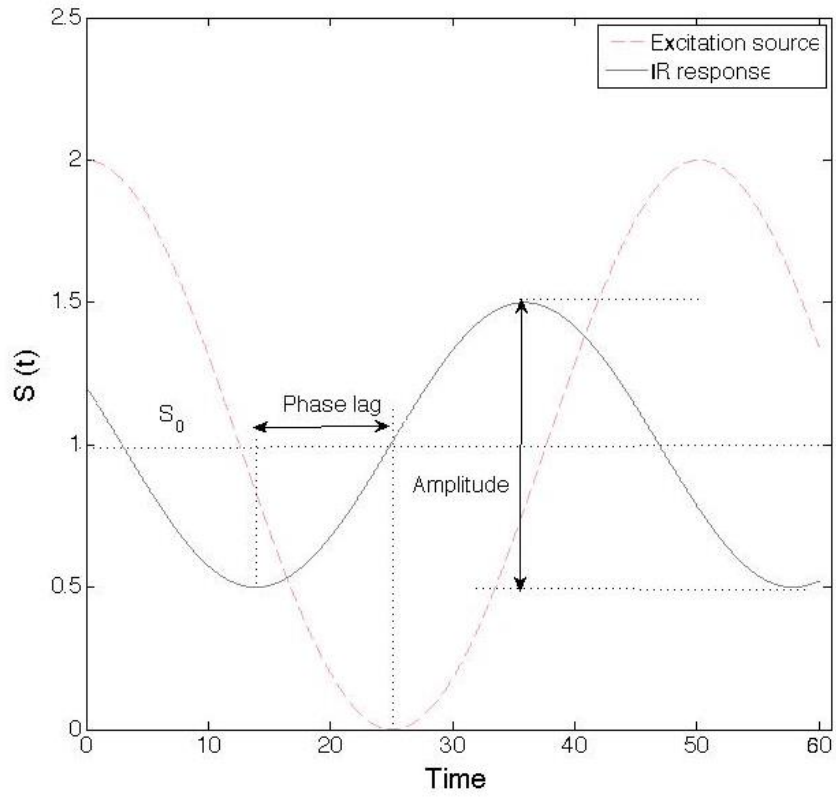

Figure 16: Amplitude and phase of the excitation signals and modulated infrared response.

In a general manner, the signal recorded by the detector is as:

$$S(t) = S_0 + \Delta S \cos(\omega t + f) \tag{2.12}$$

In this relation S_0 is the continuous part. In the frequency domain (Fourier transform), it becomes:

$$\tilde{S}(j\omega) = \underbrace{A(\omega)}_{\propto \Delta T(\omega)} e^{j\phi(\omega)} \tag{2.13}$$

In this relation $A(\omega)$ is the amplitude of the modulated variation and $\phi(\omega)$ is the phase lag at each angular frequency ω.

2.3.2 MPTR setup working at high temperature

The Thermocinetics team of I2M laboratory developed a Modulated Photothermal Radiometry experimental setup adapted for the measurements at high temperature, up to 1200°C. It is schematically represented in Figure 17.

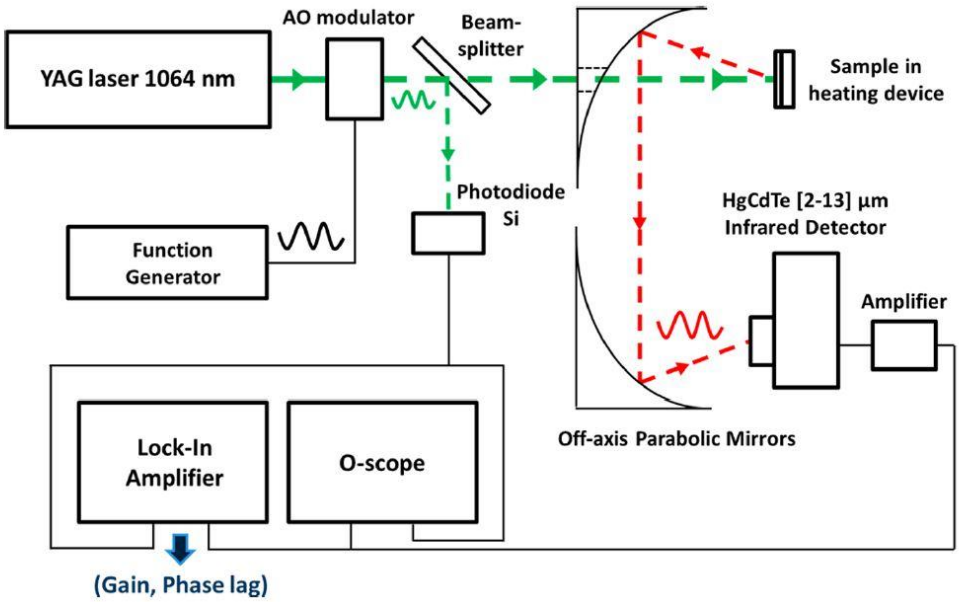

Figure 17: MPTR setup working at high temperature.

The experimental setup were developed based on the principles described above, and were inspired by the work of Mandelis et al. [22][23][24][25] on semiconductor materials and the work of Martinsons [20] on thin metallic deposits. It has been improved to work at high temperature up to 1200°C [30]-[38]. The excitation source used herein is a laser with known spatial distribution that can be easily collimated. The laser beam is periodically modulated in intensity by an acousto-optical modulator in order to obtain a periodically varying signal from 1 Hz to 1 MHz without degrading uniform profile of the laser beam. The photothermal excitation signal heats the thin layer sample that is maintained at a given temperature by a furnace under controlled atmosphere (Ar or N) or vacuum in order to prevent damage of the thin layer by evaporation or oxidation. The emitted infrared radiation from the heated surface is collected and focused by a mirror system on a mono-element infrared detector. Finally, a fast photodiode (the rising time is of the order of a nanosecond) measures the laser output from acousto-optic modulator to provide a reference for the measurement of the amplitude and the phase. The use of this photodiode prevents possible delay from the acousto-optic modulator. Signals from the photodiode and the IR detector are used as inputs of a lock in amplifier that detects the frequency and measures the amplitude and phase lag. Both quantities are of interest to identify the thermal properties of the investigated material.

More in details, the components of the setup are as follow (the experimental setup was used in the work of V. Schick during his PhD at I2M and using an Ar^+ laser at 514 nm wavelength):

- A fiber Manlight laser emitting at the 1064 nm wavelength with a 5 W CW maximum output power.
- An acousto-optic modulator (AOM, Isomet 1205C, crystal of $PbMoO_4$) driven by an Agilent 33120A function generator sweeping a frequency range from 10Hz to 100kHz producing the intensity modulation of the laser beam following a rectangular signal. Indeed, this signal is easier to follow than the sinusoidal shape. This type of equipment can achieve a theoretical efficiency of 85% from a laser beam of 0.34 mm in diameter at 1064 nm wavelength.

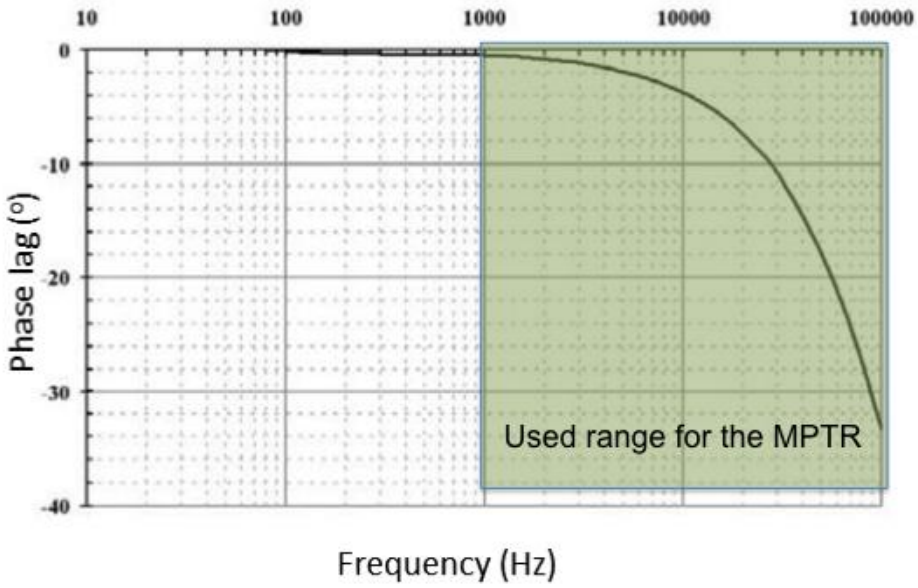

Figure 18: Measured phase-lag of modulated photothermal excitation introduced by acousto-optic modulator. The investigated frequency range is highlighted on the plot.

- A beam splitter mirror that transmits 95% of the signal.
- A fast photodiode (Thorlabs PDA 10 CF/M) with InGaAs sensitive element, leading to a rise time of the order of 1 ns and that is sensitive in the 700 – 1800 nm spectral range. It receives the 5% amplitude signal from the beam splitter. It monitors the periodic excitation signal in order to fix the reference to the lock-in amplifier. Indeed,

the AOM introduces a phase lag at high frequency that has been measured and reported in Figure 18.

- A furnace (Linkam TS 1200), being able to work up to 1200°C under controlled atmosphere (argon or nitrogen) or vacuum at 10^{-6} mbar with the help of a turbo-molecular pumping system in order to prevent the oxidation of the investigated material at high temperature. This system is adapted for measurement of the infrared radiation since the optics of the furnace is in BaF_2 (transmission spectrum of BaF_2 is given in Figure 19). The glass is transparent to the visible and infrared spectrum over the entire operating range of the laser and the infrared detector. The peak of the infrared radiation is given by the Wien's law (derived from the Planck relation): $\lambda_{max} T = 2897\ \mu m.K$. Therefore at RT (300 K) this peak is at 9.65 µm and it is at 3.74 µm when temperature of the sample is 550°C.

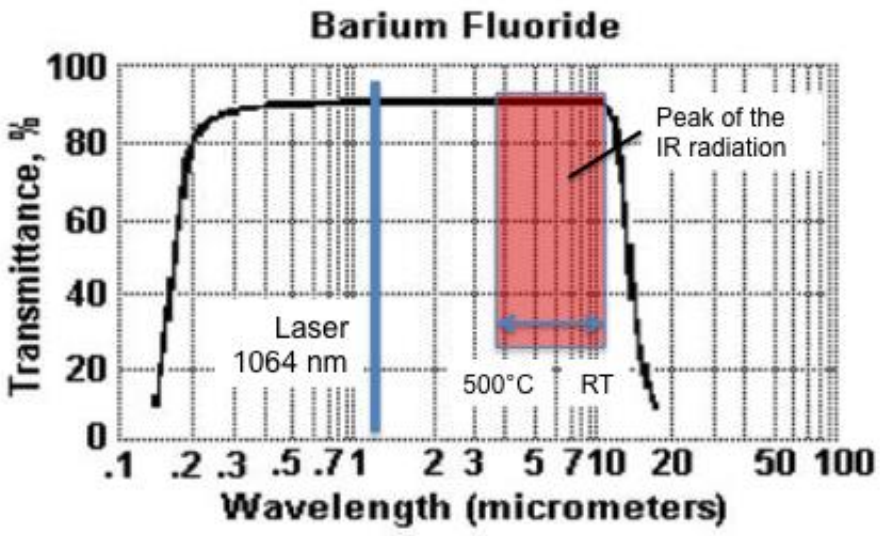

Figure 19: Transmission spectrum of the BaF_2 glass.

- Two off-axis mirrors, which collect and focus the radiation emitted by the sample on the infrared detector. These mirrors are coated with rhodium for optimum reflection of the infrared radiation (> 90% for the 3-10 µm spectral band, see Figure 20).

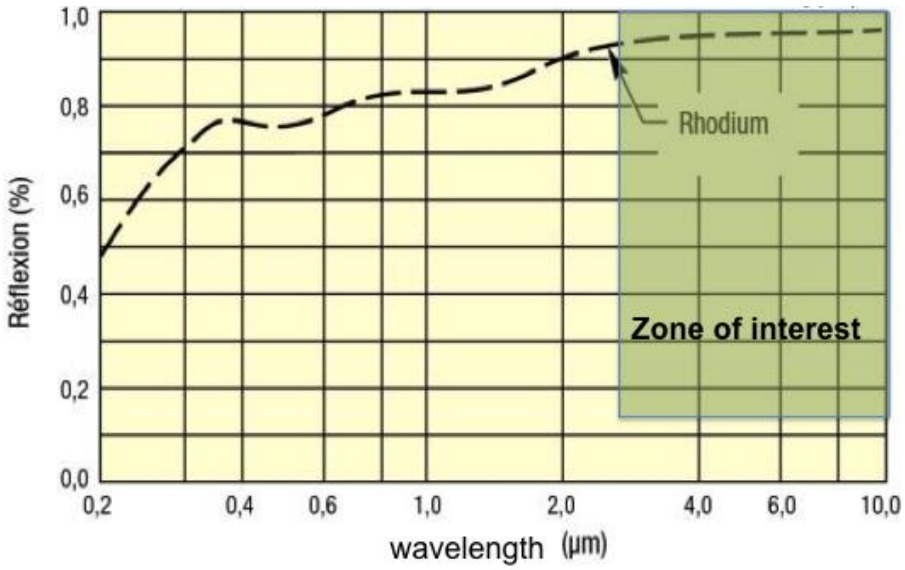

Figure 20: Reflectivity of Rhodium according to the wavelength.

- The radiation of the excitation source (1064 nm) is blocked in front of the IR detector via a 2 mm thick Germanium window whose transmission in the 1.5-13 µm is more than 45% (see Figure 21). The drawback of such filter is that it decreases the IR radiation received by the detector.

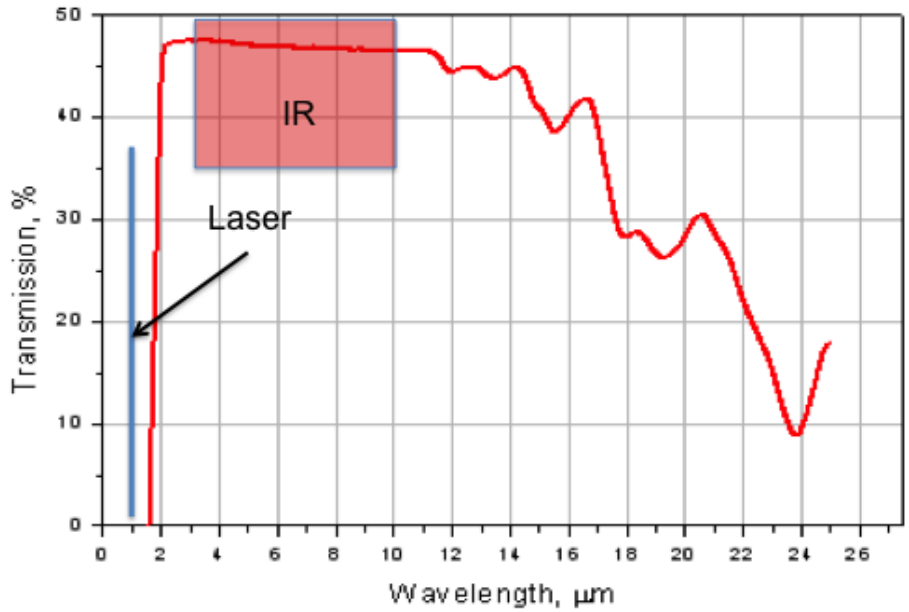

Figure 21: Transmission spectrum of Germanium (2 mm thick)

- A photoconductive detector that is only sensitive to the variations of received infrared signal, (Judson HgCdTe J15D12). Figure 22 shows that the responsivity is constant when sweeping the (1 kHz to 100 kHz) frequency range. In addition, the noise is also constant. Moreover, the detector is selected for its detectivity on the wide spectral range (2-12µm announced by the manufacturer). Indeed, as showed previously, the study carried out in this work covers a wide range of temperature and this kind of sensor is well adapted to cover the wavelengths corresponding to the infrared radiation. The infrared radiation incident to the sensitive element (HgCdTe) generates an electrical current that is amplified. The detector is cooled with liquid nitrogen. At high temperature of the sample the detectivity is higher even if the thermal disturbance is weak. The signal from the amplifier is used as the input of the Lock in amplifier.

  Let us note that the amplifier of the detector involves a phase lag that will be calibrated in the next section.

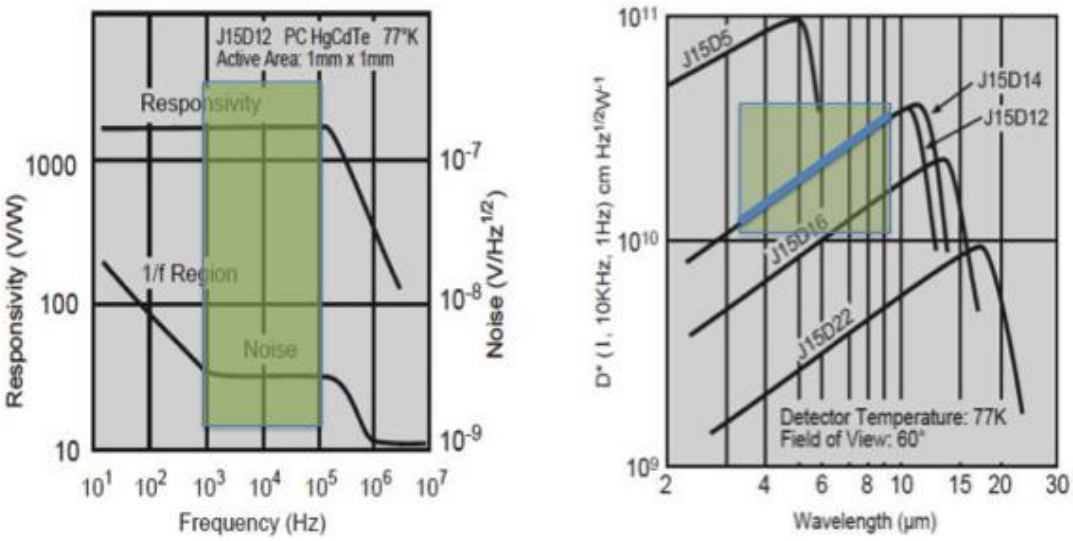

Figure 22: Technical specificity of J15D12 photo-detector (data provided by the manufacturer). Highlighted areas are related with the investigated frequency range and IR wavelengths in the present work

- The measurement of the amplitude and phase lag between the disturbance (photodiode signal) and the IR radiation (detector) is performed using a lock-in amplifier Stanford Research SR 830. This device makes it possible to detect a signal

drowned in a noise with a thousand times higher amplitude. The integration time of the measurement is set equal to 1s, which corresponds to one thousand times of the minimum period of the excitation signal (1 kHz).

- Finally a Labview interface allows the automated acquisition of amplitude and phase-lag according to the frequency and the temperature T_0 of the furnace.

2.3.3 Optical Transducer

With respect to the nanoscale thickness of the deposits in our study, the absorption of a photon flux, from the laser, cannot be longer considered as a surface phenomenon, but must be discussed according to the optical properties of the deposit (optical index, more specifically the extinction coefficient κ) with respect to this thickness. The optical penetration of the laser beam inside the material is assumed to follow the Beer Lambert law: $\exp\text{-}\left(\left(4\pi k/\lambda\right)z\right)$, where λ is the laser wavelength and z the depth. It must be also accounted that semiconductors are generally semi-transparent in the VIS and NIR wavelengths domain. Moreover, our thin films are sensitive to the environmental attacks provoked by high temperatures (evaporation, oxidation phenomena). Finally, if the deposit is of semiconductor type, additional phenomena as free charge carriers and charges recombination occur. They involve radiation that depends on the band gap E_g of the semiconductor. Calculations shows that, with E_g close to 1µm, this radiation is about the micron wavelength and therefore it can be viewed by the IR detector [16]. Furthermore, this radiation is much more higher than the thermal one generated by the disturbance (see references [22] to [27]). Adding a metallic transducer serves as the photon barrier and Schottky barrier blocking electronic transfers between the metal and the semiconductor.

For these reasons, the deposits to be analyzed are capped with a metallic layer of a few tens of nanometers thick that will play the role of a thermal and optical transducer. In other words, it will be considered at uniform temperature at each frequency and it performs the conversion of the photon flux into the heat flux. The thickness of the transducer is calculated so that it performs the optical absorption of the laser beam (the optical source is considered absorbed when 90% of the photon flux is transferred to the metallic deposit). The choice of the transducer is thus based on three criteria:

- It must be stable at high temperatures.

- It must have a low reflectivity compared to the laser source and thus a good emissivity.
- Its thickness-dimensioning to absorb 90% of the optical flow - must be relatively small enough compared to the thickness of the deposits.

The most suitable materials that can reach these criteria are obviously metals. In most cases, noble metals are used. The thin films to be analyzed are therefore covered with a 50 nm thick evaporated platinum with the optical extinction coefficient κ=5.96 at 1.064 µm. Furthermore this metal is relatively optically absorbent at the wavelengths of the excitation source (Pt reflectivity at 1064 nm is 75.6 %). This metal is rather insensitive to oxidation from environment and its melting temperature is rather high, $T_f^{Pt} = 1768°C$ at normal pressure. The absorption of the laser beam in platinum at 1064 nm is presented in Figure 23. As viewed on the figure, 97 % of the heat flux is absorbed in the Pt layer.

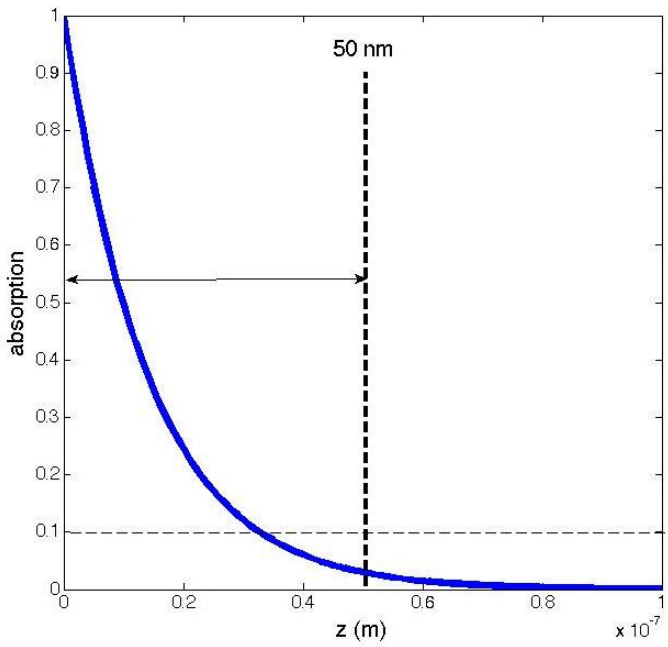

Figure 23: Optical penetration of the laser source in a platinum thin film.

2.3.4 Phase-lag calibration

The amplifier associated to IR detector adds a phase shift to the thermal signal measured during its conversion into electrical signals. The calibration of this system is done using a rapid LED type Osram SPL PL90 having a rise time of 1 ns at a wavelength of 950 nm, see

Figure 24. The infrared detector measures the LED signal, driven by the internal TTL generator of the lock-in amplifier.

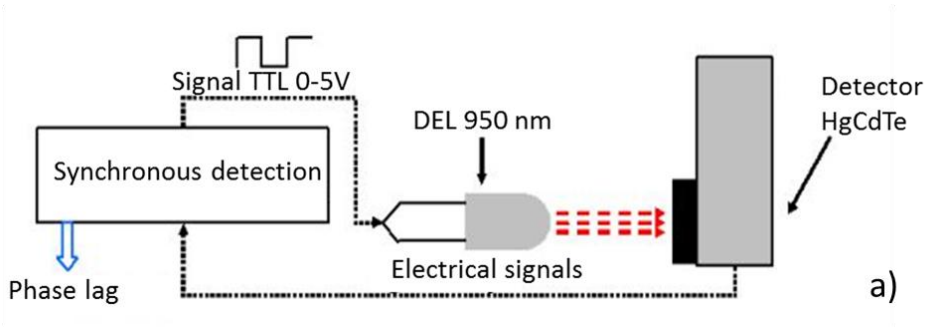

Figure 24: Experimental setup for the calibration the measurement chain

The lock-in amplifier performs the measurements with the reference to its own internal generator. The delay was thus measured, leading to the expression of the true phase-lag at the frequency *f* as:

$$f_{cor} = 2.83' \ 10^{-4} f + f_{mes} \qquad (2.14)$$

In order to validate this calibration, we performed an experiment, involving 1D heat transfer in a cylindrical tungsten sample (2 mm thick, 9 mm in diameter) of mechanically polished surface with 1µm average roughness. The measurements of amplitude and corrected phase (using relation (2.14)) are reported in Figure 25. The semi-infinite behavior of our sample from 200 Hz that is clearly shown to be characterized by:

- A phase lag equal to -45°.
- An amplitude with slope -1/2 in log-log coordinates.

In the figure, the phase presents a weak increase after 10 kHz. This increase is explained by an effect of topography of the sample surface. Indeed, the surface roughness acts as a resistive deposit on the ideal surface of the material. As it was described in the thesis of A. Cappella [29], this “apparent” rough layer involves an increase in the amplitude and more specifically in phase at high frequency that is well reproduced theoretically. Finally, we can conclude on the reliability of the calibration on the form of the relation (2.14)

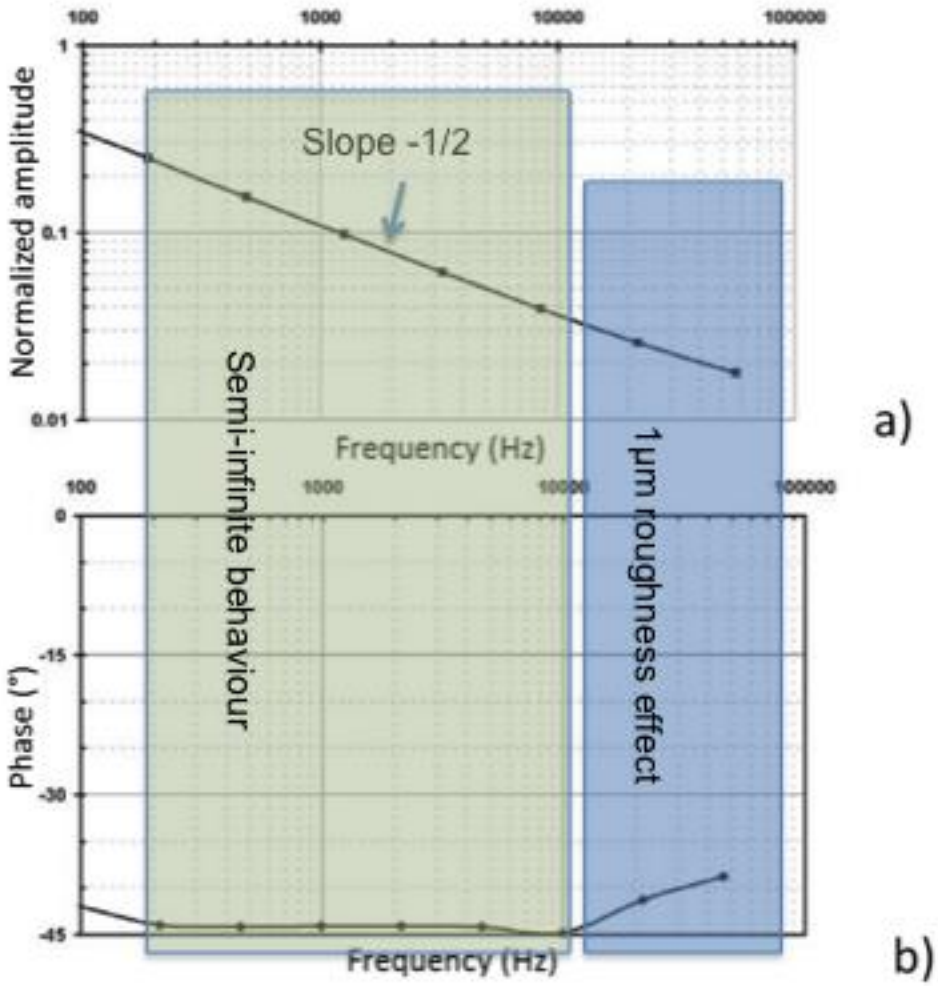

Figure 25: Measurement of a) amplitude and b) phase-lag (corrected from relation (2.14)) using the MPTR in a 1D heat transfer configuration on a tungsten sample (2mm thick, 9 mm in diameter). Two domains are clearly highlighted: the semi-infinite behaviour from 200Hz up to 10 kHz and the effect of roughness from 10 kHz.

2.4 Conclusion

In this chapter we presented the two methods that have been implemented in this work to measure the thermal resistance of IST thin films. Indeed, as it will be presented in the next chapter, the frequency is not high enough to "observe" the diffusion of heat in the deposit constituted from the superposition of thin layers, including the IST layer of interest. Although, both methods are used in the frequency domain, the 3ω and the MPTR methods work in a completely different way. The first method is a contact method that allows measuring the absolute temperature change to a known and measured variation of the heat flux dissipated by Joule effect in the strip. The second method is a contactless technique that allows reaching the phase-lag between the excitation and the surface temperature. However

in this former case, we can only deal with relative variations of both quantities, meaning that the amplitude is not used.

In the next chapter, we will develop the model of heat transfer in both experiments. From experimental data and corresponding theoretical values, we will able to implement a minimization algorithm (see Figure 13) between both quantities in order to obtain the unknown thermal property, i.e., the thermal resistance of the deposit.

2.5 References

3ω technique

[1] D. G. Cahill, H. E. Fisher, T. Klitsner, E. T. Swartz and R.O. Polh, *Thermal conductivity of thin films: measurements and understanding*, J. Vac. Sci. Technol. A **7** (3), 1259 (1989).

[2] D. G. Cahill, *Thermal conductivity measurement from 30 to 750 K: the 3ω method*, Rev. Sci. Intrum. **61**, 802 (1990).

[3] Seung-Min Lee and Sook-ll Kwun, *Heat capacity measurement of dielectric solfids using a linear surface heater: Application to ferroelectrics*, Rev. Sci. Instrum. **65** (41), (1994).

[4] D.G. Cahill, M. Katiyar and J. R. Abelson, *Thermal conductivity of a-Si:H thin films*, Phys. Rev. B **50**, 6077 (1994).

[5] S.-M. Lee and David G. Cahill, *Heat transport in thin dielectric films*, J. Appl. Phys. **81** (6), 2590 (1997).

[6] J. H. Kim, A. Feldman and D. Novotny, *Application of the three omega thermal conductivity measurement method to a film on a substrate of finite thickness*, J. Appl. Phys. **86**, 3959 (1999).

[7] L. Lu, W. Yi, and D. L. Zhang, *3ω method for specific heat and thermal conductivity measurements*, Rev. Sci. Instrum., 72 (7), 2996 (2001).

[8] A. Jacquot, B. Lenoir, A. Dausher, M. Stölzer and J. Meusel, *Numerical simulation of the 3ω method for measuring the thermal conductivity*, J. Appl. Phys. **91**, 4733 (2002).

[9] T. Borca-Tasciuc, A.R. Kumar and G. Chen, *Data reduction in 3ω method for thin-film thermal conductivity determination*, Rev. Sci. Instrum. **72**, 2139 (2001).

[10] C. E. Raudzis and F. Schatz, *Extending the 3ω method for thin-film analysis to high frequencies*, J. Appl. Phys., **93** (10), 6050 (2003).

[11] Tao Tong and Arun Majumdar, *Reexamining the 3-omega technique for thin film thermal characterization*, Rev. Sci. Instrum. **77**, 104902 (2006).

[12] S. Ahmed, R. Liske, T. Wunderer, M. Leonhardt, R. Ziervogel, C. Fansler, T. Grotjohn, J. Asmussen, T. Schuelke, *Extending the 3x-method to the MHz range for thermal conductivity measurements of diamond thin films*, Diamond & Related Materials **15**, 389 – 393 (2006)

[13] J-L. Battaglia, C. Wiemer, and M Fanciulli. *An accurate low frequecy model for the 3-omega method.* J. of Appl. Phys., **101**, 104510 (2007).

[14] R. Fallica, C. Wiemer, T. Stoycheva, E. Cianci, M. Longo, Huu T. Nguyen, J.-L. Battaglia, *Thermal properties of In-Sb-Te films and interfaces for phase change memory devices*, Microelectronics Engineering **120**, 3–8 (2013).

MPTR technique

[15] R D Cowan, *Proposed Method of Measuring Thermal Diffusivity at High Temperatures*, J. Appl. Phys. **32**, 1363–1370 (1961).

[16] E Nordal, O Kanstad, Per-Erik Nordal and Svein Otto Kanstad, *Photothermal-radiometry*, Physica Scripta **20** (5-6), 659–662 (1979).

[17] A Degiovanni, *Diffusivité et méthode flash* Revue Générale de Thermique, **185**, 420–441 (1977).

[18] S Brahim, J L Bodnar and P Grossel, *Thermal diffusivity measurement by photothermal radiometry under random excitation and parametric analysis*, Journal of Physics : Conference Series **214** (2010).

[19] J.-L. Battaglia, Andrzej Kusiak, M Bamford and J.-C. Batsale *Photothermal radiometric characterization of a thin deposit using a linear swept-frequency heat flux waveform*, Int. J. of Thermal Sciences **45** (11), 1035–1044 (2006).

[20] C Martinsons, *Analyse de revetement dur par radiometrie infrarouge photothermique : Estimation des propriétés thermiques par techniques inverses application à l'évaluation de l'adhérence*. PhD thesis, Université de Reims, 1998.

[21] C Gervaise, *Estimation des propriétés thermiques à l'échelle millimétrique par méthodes périodiques : Résolution du problème direct et du problème inverse*, Int. J. of Thermal Sciences **39** (3), 422–432 (2000).

[22] A. Mandelis, J. Batista, and D. Shaughnessy, *Infrared photocarrier radiometry of semiconductors: Physicals principles, quantitative depth profilometry and scanning imaging of deep subsurface electronic defects*, Phys. Rev. B - Condensed Matter and Materials Physics, **67** :205208, (2003).

[23] A. Mandelis, *Laser photothermal radiometry of semiconductors : principles and applications to solids states electronics*, Solids-States Electronics, **42** :1–15, (1998).

[24] A. Mandelis, *Photo-carrier radiometry of semiconductors : A novel powerful optoelectronic diffusion-wave technique for silicon process non-destructive evaluation*, NDT & E International, **39** :244–252, (2006).

[25] T. Ikari, A. Salnick, and A.Mandelis, *Theoretical and experimental aspects of three-dimensionalinfrared photothermal radiometry of semiconductors*, J. of Appl. Phys. **85** :7392–7397, (1999).

[26] C. Martinsons and M. Heuret, *Recent progress in the mesurement of the thermal properties of hard coatings*, Thin Solid Films **317** :455–457 (1998).

[27] Andreas Mandelis, Jerias Batista and Derrick Shaughnessy, *Infrared photocarrier radiometry of semiconductors : Physical principles, quantitative depth profilometry, and scanning imaging of deep subsurface electronic defects*. Phys. Rev. B **67** (20), 205208 (2003).

[28] V. Schick, Caractérisation d'une mémoire à changement de phase – Mesure de propriétés thermiques de couches minces à haute température, thèse de l'Université de Bordeaux, 2011.

[29] A. Cappella, *Caractérisation thermique à hautes température de couches minces pour mémoires à changement de phase depuis l'état solide jusqu'à l'état liquide*, thèse de l'Université de Bordeaux, 2012.

[30] Kusiak A., Battaglia J.-L., S. Gomez, J.-P. Manaud, Y. Lepetitcorps, *CuO thin films thermal conductivity and interfacial thermal resistance estimation*, Eur. Phys. J. Appl. Phys. **35**, 17 (2006).

[31] Battaglia J.-L., Kusiak A., *Thermophysical characterization of a CuO thin deposit*, Int. J. Thermophysics **175**, 10765 (2007).

[32] J. Cabrero, F. Audubert, R. Pailler, A. Kusiak, J.L. Battaglia, P. Weisbecker, *Thermal conductivity of SiC after heavy ions irradiation*, J. Nuc. Mat. **396**, 202–207 (2010).

[33] A. Kusiak, C. Pradere and J.- L. Battaglia, *Measuring of thermal conductivity of liquids using photo-thermal radiometry*, Meas. Sci. Technol. **21,** 015403 (2010).

[34] J.-L. Battaglia, A. Kusiak, V. Shick, A. Cappella, C. Wiemer, M. Longo, E. Varesi, *Thermal characterization of the SiO_2-$Ge_2Sb_2Te_5$ interface from the ambient up to 400°C*, J. Appl. Phys. **107**, 044314 (2010).

[35] J.-L. Battaglia, V. Schick, A. Kusiak, C. Rossignol, C. Wiemer, A. Lamperti, *Identification of the temperature dependent thermal boundary resistance at a metal-phase change material*, Inverse Problems in Sciences and Eng. **20**, 941 (2012).

[36] A. Kusiak, J.-L. Battaglia, J. Martan, R. Daniel, *Using of pulsed and modulated photothermal radiometry to measure the thermal conductivity of thin films*, Thermodynamica Acta, **556,** 1-5, (2013).

[37] A. Cappella, J.-L. Battaglia, V. Schick, A. Kusiak, C. Wiemer and B. Hay, *High temperature thermal conductivity of amorphous Al_2O_3 thin films grown by low temperature ALD*, Advanced Engineering Materials **15**, issue 11, 1046-1050 (2013).

[38] T. Guillemet, A. Kusiak, L. Fan, J.-M. Heintz, N. Chandra, Y. Zhou, J.-F. Silvain, Y. Lu, and J.-L. Battaglia, *Thermal characterization of diamond films through modulated photothermal radiometry*, Applied Materials and Interfaces **6**(3), 2095-102 (2014).

Chapter 3: Thermal Modeling of Heat Transfer in 3ω and MPTR experiments

3.1 Introduction

As a matter of fact, from nano-scale in quantum physics state to macro-scale, every thermal phenomenon could be expressed in the form of a partial differential equation that describes the distribution of heat (or variation in temperature) in a given region over time. Therefore, in order to point up the model for heat transfer in thin films, our research is not an exception.

At the microscale, heat is transported by mean of phonons and electrons (or holes). Those quasi-particles scatter making a temperature gradient to occur between 2 points whose distance is known as the mean free path. The scattering process is also characterized by a relaxation time that is related to the mean free path and the velocity of quasi-particles. The behavior of such particles is well described by the Boltzmann equation. The literature shows that when the temperature is close to or higher than the Debye temperature of the material, then the Fourier's law becomes usable for a very short time (a few tens of picoseconds for metals for instance). The Debye temperature is the limit temperature where all the available phonon present in the material are involved. This was clearly observed in the thesis of Vincent Shick [39] concerning the previous research on thermal properties of $Ge_2Sb_2Te_5$ at I2M laboratory based on the experimental results from a picoseconds thermoreflectometry experiment on a layer of aluminum and tungsten (see also references [40] to [43]). In case of semi-conducting alloys as the GeSbTe one, the mean free path is at the nanometer scale. Therefore, the temperature in a thin layer, calculated using the classical heat diffusion model established by Fourier's law,, reproduces the experimental response within the order of tens of picoseconds.

In this study, the experiments were performed either using the 3ω or the Modulated Photothermal Technique (MPTR), from room temperature up to 550°C, in the 100 Hz to 20000 Hz frequency range and the thickness of the deposits of interest varying from 30 nm to 105 nm. We proposed a very general model of heat diffusion process throughout both experiments, based on the equation of linear heat diffusion. This model has been widely used

for many years and mathematical tools relying on integral transforms (Laplace, Fourier, Hankel,...) are well known. To achieve this objective, we followed the three specific points below:

- Using the Laplace transform, applied on time variable, in order to transform the PDEs to ODEs;
- Using an appropriate integral transform on one geometrical coordinate (Hankel transform for the MPTR and Fourier transform for the 3ω);
- Taking into account the experimental frequency range that leads to a more simple formulation of the model in the form of a thermal impedance network.

The point is that the model is very similar for both techniques since, the frequency domain is almost comparable and they thus only differ by the spatial distribution of the heat flux: a rectangular shape for the 3ω method and a disk for the MPTR technique (see Figure 26).

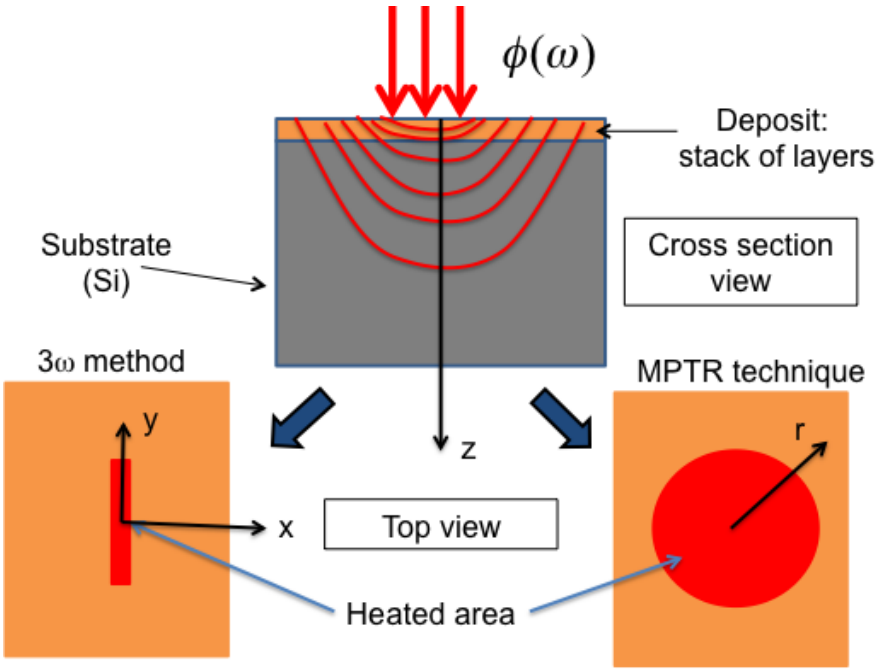

Figure 26: geometrical model for the 3ω and MPTR methods. The difference stands in the shape of the heated area.

3.2 Heat diffusion model in a composite stack of thin films

3.2.1 General formulation

In order to illustrate our purpose, let us consider the tri-layer sample represented in Figure 27, as a simplification of the general case of a multi-layered structure.

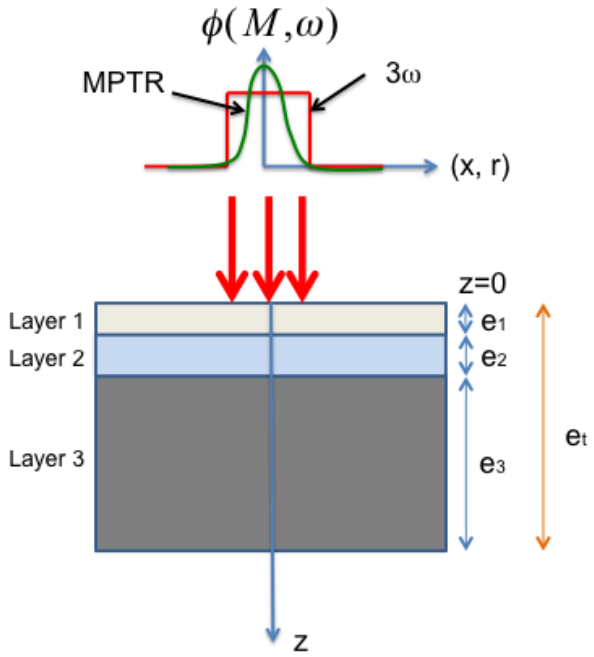

Figure 27: Configuration of a three-layer sample.

We do not consider for now the shape of the excitation (rectangular for the 3ω and cylindrical for the MPTR). For each layer *i* of the stack, the linear heat diffusion equation is:

$$r_i C_{p_i} \frac{\partial T(M,t)}{\partial t} = k_i \Delta T(M,t), M \in \text{layer } i = (1,2,3), t > 0 \qquad (3.1)$$

In this relation ρ is the density, (kg.m^{-3}), C_p is the specific heat (J.kg^{-1}.K^{-1}) and k is the thermal conductivity (W.m^{-1}.K^{-1}). Let us remind that $a = k / \rho C_p$ is the thermal diffusivity (m^2.s^{-1}). Obviously, the Laplacian $\Delta T(M,t)$ is expressed according to the adopted coordinate referential.

Between layer *i* and (*i*-1), we account for a possible thermal boundary resistance (TBR) R_i as:

$$-k_i \frac{\partial T_i(M,t)}{\partial n} = j_i(M,t) = \frac{1}{R_i}\left(T_i(M,t) - T_{i-1}(M,t)\right), M \in \text{interface } i(1,2), t > 0 \qquad (3.2)$$

In this relation n is the normal to the interface, meaning $\partial T_i(M,t)/\partial n$ is the temperature gradient at the interface. The thermal resistance per unit area R_i is in K.m^2.W^{-1}. Therefore, one defines the thermal boundary conductance (TBC) per unit area as $G_i = 1/R_i$. in W.m^{-2}.K^{-1}.

Both the 3ω and the MPTR involve a heat flux density $j_0(M,t)$ as the thermal excitation on the upper layer, always located at z=0. The boundary condition is expressed mathematically as:

$$-k_1 \frac{\partial T(M,t)}{\partial n} = j_0(M,t) + hT(M,t), M \text{ at } z=0, t>0 \quad (3.3)$$

In this relation the heat source is potentially dependent of the coordinate (the radial coordinate in the MPTR for instance). This relation accounts also for heat losses by convection and linearized radiation at the surface using the global coefficient h.

The last boundary condition is related to the bottom of the stack that is in contact with the furnace at constant temperature T_f. It is thus written as:

$$T(M,t) = T_f, M \text{ at } z=e_t, t>0 \quad (3.4)$$

Finally, the initial condition is written considering that all the sample is at the temperature of the furnace:

$$T(M,t) = T_f, \text{everywhere}, t=0 \quad (3.5)$$

In order to deal with a zero initial temperature, using the linearity of the model we are able to apply the change of variable $T'(M,t) = T(M,t) - T_f$ on relations (3.1) to (3.5), which leads to:

$$r_i C_{p_i} \frac{\partial T'(M,t)}{\partial t} = k_i \Delta T'(M,t), M \in \text{layer } i, t>0 \quad (3.6)$$

$$-k_i \frac{\partial T'_i(M,t)}{\partial n} = j_i(M,t) = \frac{1}{R_i}\left(T_i'(M,t) - T_{i-1}'(M,t)\right), M \in \text{interface } i, t>0 \quad (3.7)$$

$$-k_1 \frac{\partial T'(M,t)}{\partial n} = j_0(M,t) + hT'(M,t), M \text{ at } z=0, t>0 \quad (3.8)$$

$$T'(M,t) = 0, M \text{ at } z=e_t, t>0 \quad (3.9)$$

$$T'(M,t) = 0, \text{everywhere}, t=0 \quad (3.10)$$

3.2.2 From time to frequency

In order to work in the frequency domain, which is appropriate for both the 3ω and the MPTR, we perform a Laplace transform of the previous equations (see references [44] [45] for Laplace transform applied to the heat transfer problems and [47][48][49][50][51][52] regarding the inverse Laplace transform algorithm). Let us note that the Laplace transform is applied to the time variable t of the temperature and the heat flux density respectively as:

$$\theta(M,p) = \mathcal{L}_t\left[T'(M,t)\right] = \int_0^\infty T'(M,t)e^{-pt}\,\mathrm{d}t \tag{3.11}$$

$$\psi(M,p) = \mathcal{L}_t\left[\varphi(M,t)\right] = \int_0^\infty \varphi(M,t)e^{-pt}\,\mathrm{d}t \tag{3.12}$$

It must be noted that one of the advantages of the Laplace transform is its direct link with the Fourier transform when the initial temperature is zero. This implies that the simple transformation $p = j\omega = j2\pi f$ leads to obtain the expression of the temperature in the frequency domain. By applying this transformation on relations (3.6) to (3.10) we obtain the new system of partial differential equations as follows:

$$j\omega r_i C_{p_i} q(M,j\omega) = k_i \Delta q(M,j\omega), M \in \text{layer}\, i \tag{3.13}$$

$$-k_i \frac{\partial q_i(M,j\omega)}{\partial n} = \frac{1}{R_i}\left(q_i(M,t) - q_{i-1}(M,t)\right), M \in \text{interface}\, i \tag{3.14}$$

$$-k_1 \frac{\partial q(M,j\omega)}{\partial n} = \gamma_0(M,j\omega) + hq(M,j\omega), M \text{ at } z = 0 \tag{3.15}$$

$$q(M,j\omega) = 0, M \text{ at } z = e_t \tag{3.16}$$

3.3 From the general formulation to the 3ω and MPTR experimental configurations

3.3.1 Practical considerations about the heat diffusion length

In the frequency regime, the heat diffusion length l_h of the thermal field in 1D heat transfer is proportional to $\sqrt{a/\pi f}$, where a is the thermal diffusivity and f the frequency. Whatever the thermal diffusivity in the (10^{-6}, 10^{-7}) $m^2.s^{-1}$ range, it is found that $l_h >> e_d$ where e_d is the thickness of the deposit, i.e., the sum of the thicknesses of the deposited films on the

substrate. In practice e_d does not exceed 500 nm. As represented in Figure 28, the diffusion length is about 2 µm at 10 kHz, validating thus the previous assumption.

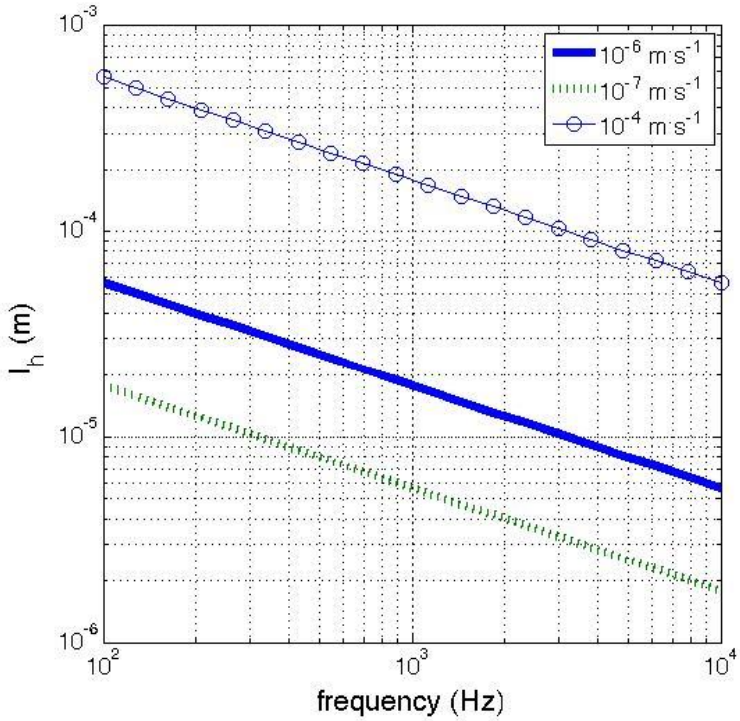

Figure 28: heat diffusion length for two values of the thermal diffusivity according to the experimental frequency range.

Therefore, the deposit, constituted by the superposition of all the thin films on the silicon substrate can be viewed as a thermal resistance R_T since diffusion cannot be observed in the experimental frequency range both during the 3ω and the MPTR methods.

Instead, the silicon substrate (10^{-4} $m^2.s^{-1}$) can be considered as a semi-infinite medium since, as reported in Figure 28, l_h remains lower than the substrate thickness (about 0.6 mm) at the lower frequency.

3.3.2 Dealing with spatial coordinates with 3ω method

In the 3ω method the heat flux is applied on the sample surface as the shape of a rectangular strip. In general, it is well admitted that the strip is infinite since its length $2l$ is very large as compared to its width $2b$. As discussed in the preceding section, the deposit is viewed as a thermal resistance R_T and the substrate is semi-infinite. In that case the Laplacian of relation (3.13) is defined as:

$$\mathrm{D}q\left(M,j\omega\right)=\mathrm{D}q\left(x,z,j\omega\right)=\frac{\partial^2 q\left(x,z,j\omega\right)}{\partial x^2}+\frac{\partial^2 q\left(x,z,j\omega\right)}{\partial z^2} \tag{3.17}$$

We define the Fourier transform (see [46]) of the temperature upon the *x* coordinate as:

$$\tilde{\theta}\left(\alpha,z,j\omega\right)=\int_0^\infty \theta\left(x,z,j\omega\right)\cos\left(\alpha x\right)\mathrm{d}x \tag{3.18}$$

It means that :

$$\frac{\partial^2}{\partial x^2}\tilde{\theta}\left(\alpha,z,j\omega\right)=-\alpha^2\tilde{\theta}\left(\alpha,z,j\omega\right) \tag{3.19}$$

Applying this integral transform to relations (3.17) and (3.13), considering only one layer (the substrate, conductivity *k* and diffusivity *a*) leads to:

$$\frac{j\omega}{a}\tilde{\theta}\left(\alpha,z,j\omega\right)=-\alpha^2\tilde{\theta}\left(\alpha,z,j\omega\right)+\frac{\partial^2\tilde{\theta}\left(\alpha,z,j\omega\right)}{\partial z^2},M\in\text{layer}\,i \tag{3.20}$$

Thus:

$$\frac{\partial^2\tilde{\theta}\left(\alpha,z,j\omega\right)}{\partial z^2}-\underbrace{\left(\alpha^2+\frac{j\omega}{a_i}\right)}_{\beta^2}\tilde{\theta}\left(\alpha,z,j\omega\right)=0,M\in\text{layer}\,i \tag{3.21}$$

The solution is:

$$\tilde{\theta}\left(\alpha,z,j\omega\right)=Ae^{\beta z}+Be^{-\beta z} \tag{3.22}$$

Using the boundary condition (3.16) leads to:

$$\tilde{\theta}\left(\alpha,z,j\omega\right)=0,\text{at}\,z=e_t\to\infty \tag{3.23}$$

This implies for relation (3.22) that A=0.

Using boundary condition (3.15) with h=0 (justification given after) leads to:

$$-k\frac{\partial\tilde{\theta}\left(\alpha,z,j\omega\right)}{\partial z}=\widetilde{\psi_0}\left(j\omega\right),\text{at}\,z=0 \tag{3.24}$$

With:

$$\widetilde{\psi_0}(j\omega)=\int_0^b \varphi_0(j\omega)\cos(\alpha x)\,\mathrm{d}x=\frac{\varphi_0(j\omega)}{\alpha}\sin(\alpha b) \tag{3.25}$$

Replacing $\tilde{\theta}(\alpha,z,j\omega)$ in (3.24) with its expression in (3.22) leads to:

$$k B\beta e^{-\beta z}=\widetilde{\psi_0}(j\omega)=\frac{\varphi_0(j\omega)}{\alpha}\sin(\alpha b),\text{at } z=0 \tag{3.26}$$

Thus:

$$B=\frac{j_0(jw)}{akb}\sin(ab) \tag{3.27}$$

Finally, we obtain:

$$\tilde{\theta}(\alpha,z,j\omega)=\frac{\varphi_0(j\omega)}{\alpha k\beta}\sin(\alpha b)e^{-\beta z} \tag{3.28}$$

The inverse Fourier transform allows us to retrieve the periodic temperature as:

$$\theta(x,z,j\omega)=\frac{2}{\pi}\int_0^\infty \tilde{\theta}(\alpha,z,j\omega)\cos(\alpha x)\,\mathrm{d}\alpha=\frac{2}{\pi}\int_0^\infty \frac{\varphi_0(j\omega)}{\alpha k\beta}\sin(\alpha b)e^{-\beta z}\cos(\alpha x)\,\mathrm{d}\alpha \tag{3.29}$$

At z=0 it is:

$$q_0(x,jw)=\frac{2}{p}\int_0^\infty \frac{j_0(jw)}{akb}\sin(ab)\cos(ax)\,\mathrm{d}a \tag{3.30}$$

Finally, we measure the average temperature of the strip, that is:

$$\overline{q_0}(jw)=\frac{1}{b}\int_0^b q_0(x,jw)\,\mathrm{d}x=\frac{2}{p}\int_0^b\int_0^\infty \frac{j_0(jw)}{bakb}\sin(ab)\cos(ax)\,\mathrm{d}a\,\mathrm{d}x \tag{3.31}$$

Thus:

$$\overline{q_0}(jw)=\frac{2j_0(jw)}{pbk}\int_0^\infty \frac{\sin^2(ab)}{a^2\sqrt{a^2+\frac{jw}{a}}}\mathrm{d}a \tag{3.32}$$

When $\sqrt{a/w}>>2b$, a more simplified form of relation (3.32) is found as:

$$\bar{q}(w)=f_0(w)\frac{1}{pk2l}\left(\frac{1}{2}\ln\left(\frac{a}{b^2}\right)-\frac{1}{2}\ln(2w)+0.923-j\frac{p}{4}\right) \tag{3.33}$$

When the thickness e_t of the sample is not so large as compared to l_h, the boundary condition (3.23)must take into account the value of e_t , and the model (3.28) becomes:

$$\tilde{\theta}(\alpha,z,j\omega)=\frac{\varphi_0(j\omega)}{\alpha k\beta\tanh(\beta e_t)}\sin(\alpha b)e^{-\beta z} \tag{3.34}$$

Since $j_0(w)=\frac{f_0}{4bl}\sin(wt)$, and adding the thermal resistance accounting for the deposit on the substrate, one finally obtains the temperature magnitude corresponding to the measured temperature as:

$$\overline{Dq}(w)=f_0\left[\frac{1}{pkb^2 2l}\int_0^{\infty}\frac{\sin^2(ab)}{a^2\tanh\left(\sqrt{a^2+\frac{jw}{a}}e_t\right)\sqrt{a^2+\frac{jw}{a}}}da+\frac{R_T}{4bl}\right] \tag{3.35}$$

The integral can be numerically calculated by using a quadrature method (routine INTEGRAL in Matlab).

3.3.3 Dealing with spatial coordinates with MPTR method

In the MPTR method, the heat flux is applied on the shape of a disk with radius r_0 with a Gaussian distribution of the heat flux. In that case the Laplacian of relation (3.13) is defined as:

$$Dq(M,jw)=Dq(r,z,jw)=\frac{\partial}{\partial r}\left(r\frac{\partial q(r,z,jw)}{\partial r}\right)+\frac{\partial^2 q(r,z,jw)}{\partial z^2} \tag{3.36}$$

We define the Hankel transform (see [44]) of the temperature upon the *r* coordinate as:

$$\tilde{\theta}(\alpha,z,j\omega)=H\{\theta(r,z,j\omega)\}=\int_0^R\theta(r,z,j\omega)rJ_0(\alpha r)dr \tag{3.37}$$

J_0 is the Bessel function of the first kind and first order. The integral is bounded by the radius (equivalent) of the sample. It means that :

$$\frac{\partial}{\partial r}\left(r\frac{\partial\tilde{\theta}(\alpha,z,j\omega)}{\partial r}\right)=-\alpha^2\tilde{\theta}(\alpha,z,j\omega) \tag{3.38}$$

Applying this integral transform to relations (3.17) and (3.13), considering only one layer (the substrate, conductivity k and diffusivity a) leads to:

$$\frac{j\omega}{a}\tilde{\theta}\left(\alpha,z,j\omega\right)=-\alpha^2\tilde{\theta}\left(\alpha,z,j\omega\right)+\frac{\partial^2\tilde{\theta}\left(\alpha,z,j\omega\right)}{\partial z^2},M\in\text{layer}\,i \tag{3.39}$$

Thus:

$$\frac{\partial^2\tilde{\theta}\left(\alpha,z,j\omega\right)}{\partial z^2}-\underbrace{\left(\alpha^2+\frac{j\omega}{a_i}\right)}_{\beta^2}\tilde{\theta}\left(\alpha,z,j\omega\right)=0,M\in\text{layer}\,i \tag{3.40}$$

The solution is:

$$\tilde{\theta}\left(\alpha,z,j\omega\right)=Ae^{\beta z}+Be^{-\beta z} \tag{3.41}$$

Using the boundary condition (3.16) leads to:

$$\tilde{\theta}\left(\alpha,z,j\omega\right)=0,\text{at}\,z=e_t\to\infty \tag{3.42}$$

This implies for relation (3.41) that A=0.

Using boundary condition (3.15) with h=0 (justification given after) leads to:

$$-k\frac{\partial\tilde{\theta}\left(\alpha,z,j\omega\right)}{\partial z}=\widetilde{\psi_0}\left(j\omega\right),\text{at}\,z=0 \tag{3.43}$$

With:

$$\widetilde{\psi_0}\left(j\omega\right)=\int_0^R\varphi_0\left(r,j\omega\right)rJ_0\left(\alpha r\right)\mathrm{d}r \tag{3.44}$$

Since the heat flux spatial distribution is a Gaussian profile as: $j_0\left(r,j\omega\right)=j_0\left(j\omega\right)e^{-2\left(\frac{r}{r_0}\right)^2}$

$$\widetilde{\psi_0}\left(j\omega\right)=\varphi_0\left(j\omega\right)\int_0^R e^{-2\left(\frac{r}{r_0}\right)^2}rJ_0\left(\alpha r\right)\mathrm{d}r=\varphi_0\left(j\omega\right)\frac{r_0^2}{4}e^{-\frac{\left(\alpha r_0\right)^2}{8}} \tag{3.45}$$

Replacing $\tilde{\theta}\left(\alpha,z,j\omega\right)$ in (3.41) with its expression in (3.43) leads to:

$$k\,B\,b\,e^{-bz} = j_0(jw)\frac{r_0^2}{4}e^{-\frac{(ar_0)^2}{8}}\ ,\text{at}\ z=0 \tag{3.46}$$

Thus:

$$B=\frac{j_0(jw)}{a\,k\,b}\frac{r_0^2}{4}e^{-\frac{(ar_0)^2}{8}} \tag{3.47}$$

Finally, we obtain:

$$\tilde{\theta}(\alpha,z,j\omega)=\frac{\varphi_0(j\omega)}{\alpha\,k\,\beta}\frac{r_0^2}{4}e^{-\frac{(\alpha r_0)^2}{8}}e^{-\beta z} \tag{3.48}$$

The inverse Hankel transform allows us to retrieve the periodic temperature as:

$$\theta(r,z,j\omega)=\int_0^R\tilde{\theta}(\alpha,z,j\omega)\alpha J_0(\alpha r)\mathrm{d}\alpha \tag{3.49}$$

At z=0 it is:

$$q_0(r,jw)=\int_0^R\frac{j_0(jw)}{a\,k\,b}\frac{r_0^2}{4}e^{-\frac{(ar_0)^2}{8}}\,a\,J_0(ar)\mathrm{d}a \tag{3.50}$$

Considering the heat flux equal to zero at $r=R$, the values of α are solutions of the relationship $J_1(aR)=0$, which is a transcendental equation with an infinite number of solutions. These solutions are such that:

$$a_nR\approx p\left(n+\frac{1}{4}\right)-\frac{3}{8p\left(n+\frac{1}{4}\right)},a_0=0 \tag{3.51}$$

This integral (3.50) can be evaluated by a series as:

$$q_0(r,jw)=q_0(r,z,p)=\frac{j_0(jw)}{k}\sum_{n=0}^{N}\frac{2J_0(a_nr)}{a_n\sqrt{a_n^2+\frac{jw}{a}R^2J_0(a_nR)^2}}\frac{r_0^2}{4}e^{-\frac{(ar_0)^2}{8}} \tag{3.52}$$

The average temperature on the heated area, viewed by the detector of equivalent radius r_d, is:

$$\overline{q_0}(j\omega)=\frac{1}{\pi r_d^2}\int_0^{r_d} q_0(r,z,p)\,r\,2\pi\,\mathrm{d}r=\frac{2j_0(j\omega)}{k r_d^2}\sum_{n=0}^{N}\frac{2\int_0^{r_d} J_0(a_n r)\,r\,\mathrm{d}r}{a_n\sqrt{a_n^2+\frac{j\omega}{a}}R^2 J_0(a_n R)^2}\frac{r_0^2}{4}e^{-\frac{(a r_0)^2}{8}} \quad (3.53)$$

Since: $\int_0^{r_d} J_0(a_n r)\,r\,\mathrm{d}r=\frac{r_d J_1(a_n r_d)}{a_n}$

$$\overline{q_0}(j\omega)=\frac{r_0^2 j_0(j\omega)}{r_d k}\sum_{n=0}^{N}\frac{J_1(a_n r_d)}{a_n^2\sqrt{a_n^2+\frac{j\omega}{a}}R^2 J_0(a_n R)^2}e^{-\left(\frac{a_n r_0}{2}\right)^2} \quad (3.54)$$

When the thickness e_t of the sample is not so large as compared to l_h, the boundary condition (3.42)must take into account the value of e_t , and the model (3.48) becomes:

$$\tilde{\theta}(\alpha,z,j\omega)=\frac{\varphi_0(j\omega)}{\alpha k\beta\tanh(\beta e_t)}\frac{r_0^2}{4}e^{-\frac{(\alpha r_0)^2}{8}}e^{-\beta z} \quad (3.55)$$

Taking into account the thermal resistance of the deposit, the final relation is:

$$\overline{q_0}(j\omega)=j_0(j\omega)\left[\frac{r_0^2}{r_d k}\sum_{n=0}^{N}\frac{J_1(a_n r_d)}{a_n^2\sqrt{a_n^2+\frac{j\omega}{a}}R^2 J_0(a_n R)^2}e^{-\left(\frac{a_n r_0}{2}\right)^2}+R_T\right] \quad (3.56)$$

in the case of the semi-infinite behavior, or :

$$\overline{q_0}(j\omega)=j_0(j\omega)\left[\frac{r_0^2}{r_d k}\sum_{n=0}^{N}\frac{J_1(a_n r_d)}{a_n^2\tanh\left(e_t\sqrt{a_n^2+\frac{j\omega}{a}}\right)\sqrt{a_n^2+\frac{j\omega}{a}}R^2 J_0(a_n R)^2}e^{-\left(\frac{a_n r_0}{2}\right)^2}+R_T\right] \quad (3.57)$$

for the finite substrate thickness.

When the heated radius area r_0 is comparable to the sample radius R, the heat transfer is 1D and the relations (3.56) and (3.57) largely simplify as:

$$\bar{q}(j\omega) = \begin{cases} j_0(j\omega)\left(\dfrac{1}{k\sqrt{\dfrac{j\omega}{a}}} + R_T\right), & z \to \infty \\ j_0(j\omega)\left(\dfrac{1}{k\tanh\left(e_t\sqrt{\dfrac{j\omega}{a}}\right)\sqrt{\dfrac{j\omega}{a}}} + R_T\right), & z = e_t \end{cases} \tag{3.58}$$

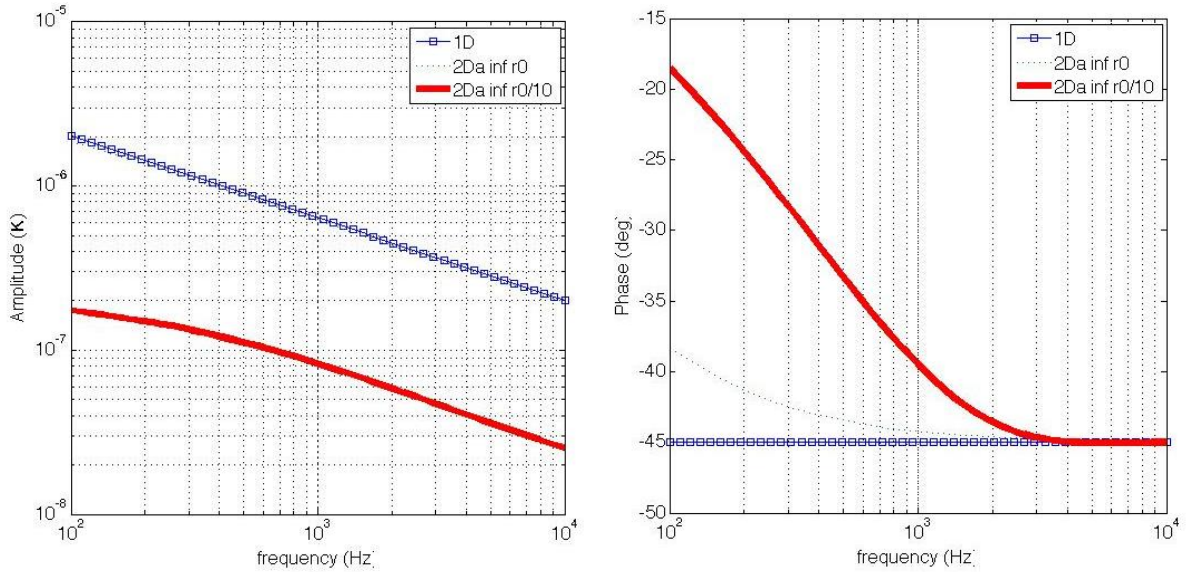

Figure 29: amplitude and phase calculated for the semi infinite substrate (with R_T=0) considering a 1D heat transfer model (relation (3.58)) and the 2D axi model (relation (3.54)). Values are r_0 = 2.5x10^{-3} m; r_d = 0.5x10^{-3} m; R = 2.5x10^{-3} m; k=238 W.m^{-1}.K^{-1}, a = 1.45x10^{-4} m^2.s^{-1} (silicon).

The amplitude and the phase are respectively calculated as:

$$\left\|\bar{q}(\omega)\right\| = \left(\mathrm{Re}\left[\bar{q}(j\omega)\right]^2 + \mathrm{Im}\left[\bar{q}(j\omega)\right]^2\right)^{1/2} \tag{3.59}$$

$$f(\omega) = \arg\left[\bar{q}(j\omega)\right] = \arctan\frac{\mathrm{Im}\left[\bar{q}(j\omega)\right]}{\mathrm{Re}\left[\bar{q}(j\omega)\right]} \tag{3.60}$$

A comparison between the amplitude and the phase calculated from both the 1D model (relation (3.58)) and the 2D axi model (relation (3.54)) is showed in Figure 29, considering the sample behaves has a semi infinite medium. It is clearly demonstrated that when r_0=R, the two models give a very comparable response. The difference observed for the phase at low

frequency comes from the fact that the radius r_d of the aimed area seen by the detector is lower than r_0 and that the heat profile is Gaussian. Therefore, the complete agreement occurs from a frequency that is about 1 kHz in the simulation. This simulation also shows that the phase is more sensitive to a change in the parameters that the amplitude.

The same simulation has been performed, taking into account the substrate thickness e_s. The amplitude and the phase calculated from both the 1D model (relation (3.58)) and the 2D axi model (relation (3.57)) are reported in Figure 30. The gap between the 1D heat transfer model and the 2D axi model is all the more pronounced than the radius r_0 is small compared to R. Again it appears that working at a frequency higher than 1 kHz will ensure a good agreement between both models regarding the phase value.

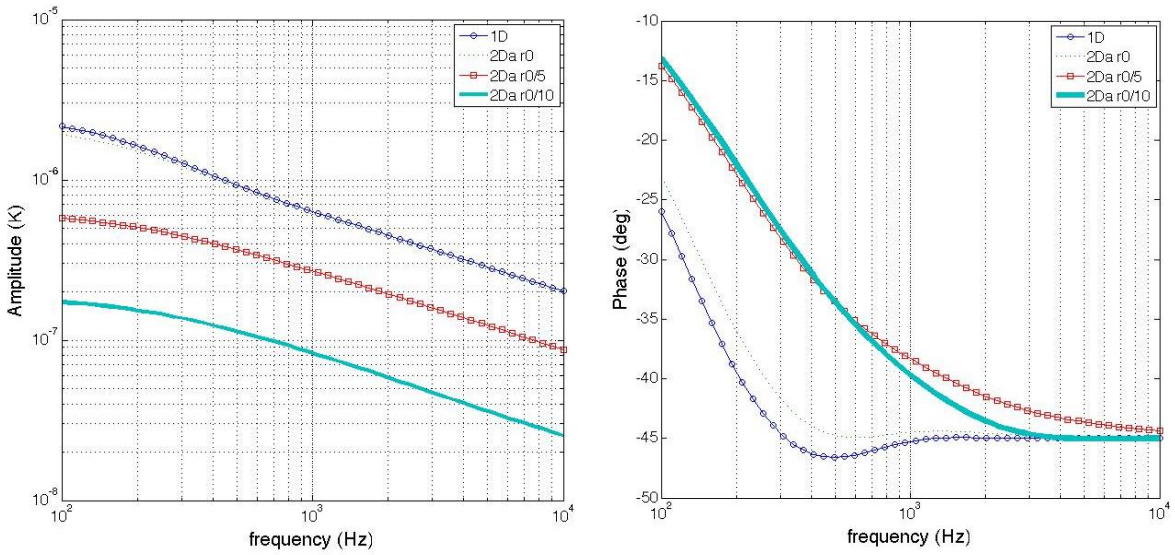

Figure 30: amplitude and phase calculated for the substrate of thickness e_t=0.6 mm (with R_T=0) considering a 1D heat transfer model (relation (3.58)) and the 2D axi model (relation (3.54)). Values are r_0 = 2.5x10^{-3} m; r_d = 0.5x10^{-3} m; R = 2.5x10^{-3} m; k=238 W.m^{-1}.K^{-1}, a = 1.45x10^{-4} m^2.s^{-1} (silicon).

Obviously those simulations are interesting in terms of experimental design since they allow seeking for the appropriate frequency range to use the 1D heat transfer model. Using such a model presents several advantages as, for the most interesting one, to avoid the uncertainty on the geometrical dimensions: R, r_0 and r_d.

3.4 Practical estimation of RT in the 3ω and MPTR methods

In the 3ω and MPTR methods, the substrate (Si) is well known. The unknown parameter is the thermal resistance R_T of the deposit that encompass for the thermal resistance of each layer and the thermal boundary resistance between each layer. We are thus interested in

analysing the sensitivity of the amplitude and phase versus RT for both the 3ω and the MPTR methods.

3.4.1 Sensitivity to R_T using the 3ω method

Starting from the model in relation (3.35), we varied the value of RT and calculated the average temperature magnitude. The results are reported in Figure 31. This simulation demonstrates that variation of RT more or equal than 10^{-8} $m^2.K.W^{-1}$ are easily detectable by the 3ω method on the investigated frequency range.

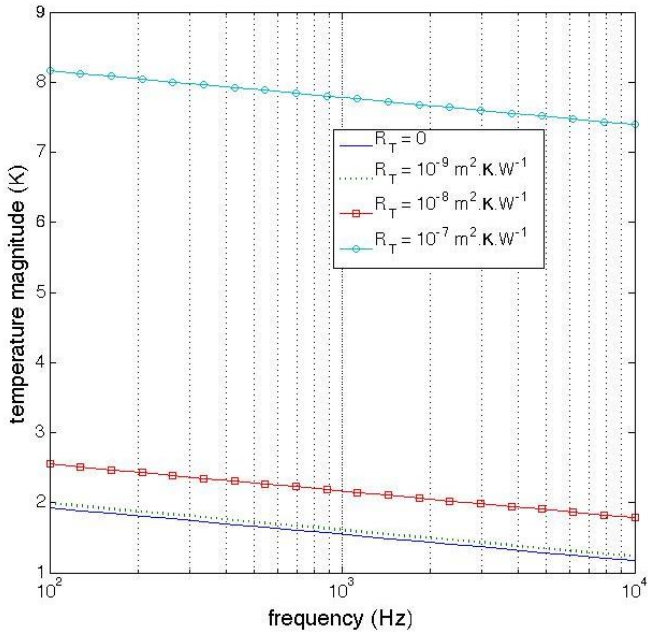

Figure 31: amplitude calculated for the substrate of thickness e_s=0.6 mm with differents values of R_T considering the heat transfer model (relation (3.35)). Parameters are b = 2 µm; l = 2 mm; P = 1 W; k=238 $W.m^{-1}.K^{-1}$, a = 1.45x10^{-4} $m^2.s^{-1}$ (silicon).

3.4.2 Sensitivity to R_T using the MPTR method

Starting from the 1D heat transfer model (relation (3.58) considering the thickness e_t of the substrate), we calculated the amplitude and the phase considering several values for R_T. The frequency range has been chosen in the [10^3-10^5] Hz range accordingly with the analysis in the previous section. The results of those simulations are reported in Figure 32. They clearly demonstrate that R_T can be identified from the phase measurement when $R_T \geq 10^{-8}\,m^2.K.W^{-1}$. This is well adapted to the configuration of thin dielectric and semi-conducting layers that are the subject of the present thesis.

In addition, as said in the previous chapter, the MPTR does not allow to easily measure the absorbed heat flux as well as the absolute temperature on the area aimed by the detector. Therefore, using the phase becomes a requirement. Fortunately, it appears that this is also the best quantity for the identification of R_T.

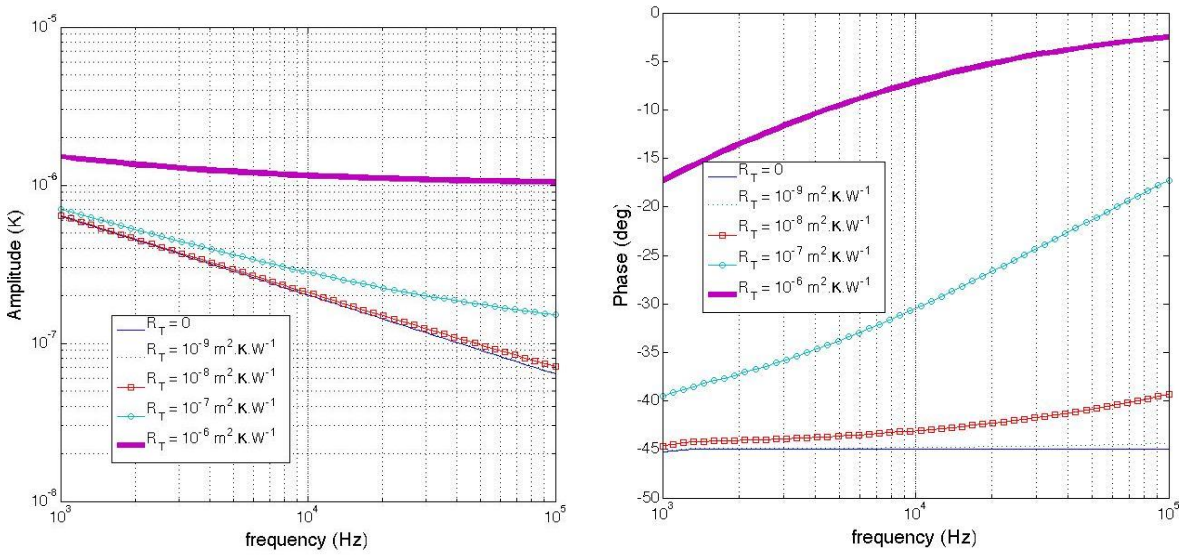

Figure 32: amplitude and phase calculated for the substrate of thickness e_s=0.6 mm with differents values of R_T=0 considering a 1D heat transfer model (relation (3.58)). Parameters are r_0 = 2.5x10^{-3} m; r_d = 0.5x10^{-3} m; R = 2.5x10^{-3} m; k=238 W.m^{-1}.K^{-1}, a = 1.45x10^{-4} m^2.s^{-1} (silicon).

3.5 Identification of RT

In practice, we implement a minimization method to identify R_T starting from measurement of the absolute temperature in the 3ω method or measurement of the phase in the MPTR method.

The method consists in minimizing the quadratic gap between the theoretical phase $f(w)$ and the measured one $f_m(w)$ all over the experimental frequency range as:

$$J = \sum_{i=1}^{N} \left(f(w_i) - f_m(w_i) \right)^2 \tag{3.61}$$

In this relation, N denotes the number of investigated frequency. Since the sensitivity function $S_{R_T}(f(w))$ depends on R_T, one must use a non-linear least square algorithm [53]. We used the classical Levenberg-Marquardt algorithm that is very efficient and fast when dealing with only one unknown parameter (information regarding the algorithm are in [54][55][56]).

One interest of using such algorithm is that it leads to evaluate the standard deviation of the estimated parameter as:

$$\sigma_{R_T} = \sqrt{\left(\mathbf{S}^t \mathbf{S}\right)^{-1} \sigma_e^2} \tag{3.62}$$

with the sensitivity vector: $\mathbf{S} = \left[\begin{array}{ccc} S_{R_T}\left(\phi(\omega_1)\right) & \cdots & S_{R_T}\left(\phi(\omega_N)\right) \end{array} \right]$

In practice the sensitivity are calculated using a standard finite difference scheme as:

$$S_{R_T}\left(\overline{\Delta q}(w)\right) = \frac{\partial \overline{\Delta q}(w)}{\partial R_T} = \frac{\overline{\Delta q}(1.1R_T, w) - \overline{\Delta q}(R_T, w)}{0.1R_T} \tag{3.63}$$

for the 3ω method, and:

$$S_{R_T}\left(f(w)\right) = \frac{\partial f(w)}{\partial R_T} = \frac{f(1.1R_T, w) - f(R_T, w)}{0.1R_T} \tag{3.64}$$

for the MPTR technique.

The standard deviation of the measurement noise can be approximated by the value of the residuals at the end of the minimization process as: $\sigma_e^2 = J^2 / N$

3.6 Evaluation of *k* and TBR

The experimental principle is as follows: for each value of the frequency ω, we identify the thermal resistance of the deposit that is expressed according to the thermal conductivity of each layer *i* composing the deposit and the thermal boundary resistances TBRs between the layers. Therefore, we can express this thermal resistance as:

$$R_T = \sum_{i=1}^{N} \frac{e_i}{k_i} + \underbrace{\sum_{i=1}^{N-1} \mathrm{TBR}_i}_{R^i} \tag{3.65}$$

In this relation e_i and k_i denote the thickness and thermal conductivtviy of layer *i* and TBR_i is the resistance at the interface between layer *i* and *i*+1 and *N* denotes the number of layers constituting the deposit.

Thus, in order to discriminate the thermal conductivity of the layer of interest, we have to consider several thicknesses of this layer (at least 3 or 4). The value of RT is then identified

for each sample constituted with the varying thickness of the investigated layer. The relation (3.65) is re-written as:

$$R_T = \sum_{i=1}^{N-1} \frac{e_i}{k_i} + \underbrace{\frac{e_{IST}}{k_{IST}}}_{\text{layer of interest}} + R^i \tag{3.66}$$

In this relation, we make appear the thermal resistance of interest, i.e., that of the IST. Representing the measured value of R_T according to e_{IST}, we thus are able to determine k_{IST} and R^i as:

$$\frac{1}{k_{IST}} = \frac{dR_T}{de_{IST}} \tag{3.67}$$

and:

$$R^i = R_T - \sum_{i=1}^{N-1} \frac{e_i}{k_i} + \frac{e_{IST}}{k_{IST}} \tag{3.68}$$

It means that the slope is the inverse of the thermal conductivity k_{IST} and the total TBR is the value of R_T extrapolating the regression line at e_{IST}=0. The protocol is schematically represented in Figure 33.

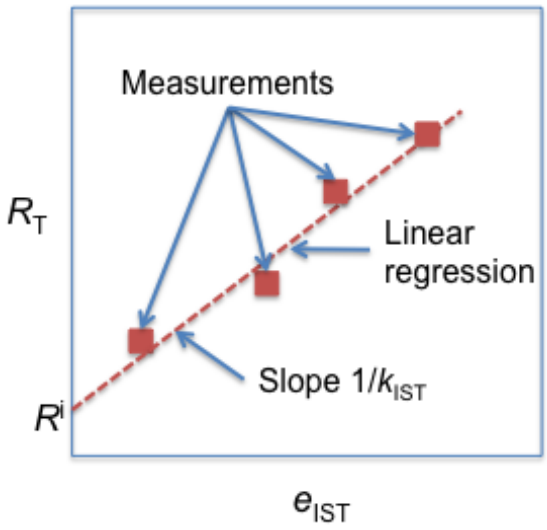

Figure 33: protocol for the identification of the thermal conductivity of the layer of interest (here the IST) and the total TBR from measurement of RT using the 3ω and the MPTR techniques.

This protocol, assumes that all the other layers constituting the stack are well known. In addition, this method can only lead to the total TBR, meaning that the thermal resistance at the interfaces of the layer of interest with upper and lower neighbor layers can be achieved by assuming the other TBR are known.

Obviously the protocol presented here is valid either for the 3ω or the MPTR methods.

3.7 Conclusion

In this chapter we presented the heat transfer models for both the 3ω and MPTR methods. As expected they are very similar since only the shape of the disturbance (the heat flux) is different. We used the Laplace transform as a classical mathematical tool to pass from time to frequency domain. The use of the Fourier transform would have given the same result but it has less general impact since it is restricted to periodic excitation, whereas the Laplace transform can deal with any transient waveform of the heat flux.

Using the rectangular geometrical shape for the strip, in the 3ω method, and the disk in the MPTR method, we applied appropriate integral transform on spatial coordinate that allowed us to modify the Laplacian of the temperature in the heat diffusion equation. All those transforms lead to obtain an analytical expression for the average temperature on the aimed area.

We demonstrated that measurements are well sensitive to a change in R_T on a specific frequency range that will be used during the experiments.

Implementing a non-linear minimization algorithm, we are finally able to identify the thermal resistance of the deposit as well as the standard deviation for the obtained value.

A protocol is implemented that consists in measuring the thermal resistance of the deposit by varying the thickness of the layer of interest (the IST layer in this study). This makes the method rather long but it leads to very accurate value of the thermal conductivity of the layer and to the total boundary resistance at the interfaces constituting the deposit.

3.8 References

Model of heat transfer at very short times

[39] V. Schick, *Caractérisation d'une mémoire à changement de phase – Mesure de propriétés thermiques de couches minces à haute température*, thèse de l'Université de Bordeaux, 2011.

[40] J.-L. Battaglia, V. Schick, C. Rossignol, O. Fudym, P. H. A. Nobrega, H. R. B. Orlande *Global estimation of thermal parameters from a picoseconds thermoreflectometry experiment*, Int. J. Thermal Sciences **57**, 17-24 (2012).

[41] P. H. A. Nobrega, H. R. B. Orlande, J.-L. Battaglia, *Bayesian estimation of thermophysical parameters of thin metal films heated by fast laser pulses*, Int. Comm. In Heat and Mass Transfer **38**, 9, 1172-1177 (2011).

[42] V. Schick, J.-L. Battaglia, A. Kusiak, C. Rossignol, C. Wiemer, *Temperature dependant thermal and mechanical properties of a metal-phase change layer interface using the time resolved pump probe technique*, J. of Phys.: Conference Series, **278**, 012024 (2011).

[43] J.-L. Battaglia, A. Kusiak, C. Rossignol, N. Chigarev, *Thermal diffusivity and effusivity of thin layers using the time-domain thermoreflectance*, Phys. Rev. B **76**, 184110 (2007).

Integral transforms

[44] D. Maillet, S. André, J.-C. Batsale, A. Degiovanni, C. Moyne, *Thermal Quadrupoles: an efficient method for solving the heat equation trough integral Transforms*, J. Wiley and sons, 2000.

[45] J. Pailhes, C. Pradere, J.-L. Battaglia, J. Toutain, A. Kusiak, A.W. Aregba, J.C. Batsale, *Improvement of the thermal quadrupole method for multilayered media with heat sources*, J. Thermal Sciences **53**, 49–55 (2012).

[46] Sulima P. Y., Battaglia J.-L., Zimmer T., Batsale J.-C., *Self heating modelling of SiGe heterojunction bipolar transistor*, Int. Comm. Heat Mass Transfer **34**, 553 (2007).

[47] B. Davies and B. Martin, *Numerical Inversion of the Laplace Transform, a Critical Evaluation and Review Methods*, J. Comput. Phys., **33**, 1, 1979.

[48] D. G. Duffy, *On the numerical inversion of Laplace Transform: comparison of three new methods on characteristic problems from applications*, ACM Trans. Math. Soft. **19**, 33, 1993.

[49] F. R. de Hoog, J. H. Knight, A. N. Stokes, *An improved method for numerical inversion of Laplace transforms*, S.I.A.M. J. Sci. and Stat. Comp. **3**, 357, 1982.

[50] D. P. Gaver Jr., *Observing stochastic processes and approximate transform inversion*, Operations Research **14**, 44, 1966.

[51] H. Stehfest, *Algorithm 368: numerical inversion of Laplace transforms*, Com. of the ACM **13**, 47, 1970.

[52] P. Den Iseger, *Numerical transform inversion using Gaussian quadrature*, Probability in the Engineering and Informational Sciences **20**, 1, 2006.

Non-linear minimization techniques

[53] J. V. Beck and K. J. Arnold, Parameter estimation in engineering and science, John Wiley & sons, 1976.

[54] K. Levenberg, « A Method for the Solution of Certain Problems in Least Squares », dans *Quart. Appl. Math.* **2**, 164-168 (1944).

[55] D. Marquardt, « An Algorithm for Least-Squares Estimation of Nonlinear Parameters », dans *SIAM J. Appl. Math.* **11**, 431-441 (1963).

[56] P. E. Gill et W. Murray, « Algorithms for the solution of the nonlinear least-squares problem », *SIAM J. Numer. Anal.* **15** (5), 977-992 (1978).

Chapter 4: Experiments, results and discussions

4.1 Introduction

In this chapter, the 3ω contact method and the Modulated Photothermal Radiometry (MPTR) contactless method, both presented in the previous chapter, allowed us to carry out an estimation of the IST thermal conductivity as well as the thermal boundary resistance at the interfaces with neighbourhood layers at the bottom and the top. A model for both the thermal conductivity and the thermal boundary resistance will be used that will help us to understand better the possible reasons for a significant difference with experimental data.

First, thermal conductivity and TBR have been measured using the 3ω method at the MDM laboratory. The samples were measured at room temperature and then annealed at 480°C. Electrical resistivity measurements of the IST have also been performed. As presented in the first chapter, the phase change (active) material (PCM) is surrounded by a dielectric in order to ensure the electrical insulation but also to avoid thermal cross talk between neighbours' memory cells. Therefore, the interface between IST and dielectric layers as silicon dioxide, silicon nitride and alumina was also analysed. For these thin films the effect of layer interfaces on the apparent thermal conductivity cannot be neglected. Although the IST film thickness remains higher than the phonon mean free path, the interface between layers, which acts as a barrier to heat diffusion, affects the measurement in such a way that the measured (apparent) thermal conductivity exhibits a dependence on the layer thickness. This means obviously that the thermal resistance at the interface is of the same order of magnitude than the thermal resistance of the layer itself. In this work, this effect has been taken into account in terms of an additional thermal interfacial resistance R_i. The IST intrinsic thermal conductivity possible dependence on PCM thickness and surrounding layers nature can be explained as an influence of the grain size or the anisotropy of the film. However, the thermal conductivity existence needs the IST thickness to be at least 10 times higher than the phonon mean free path. This assumption has been adopted in this work.

The 3ω method being not well designed to deal with in-situ temperature variation of the sample, we applied the MPTR with a [RT-550°C] temperature range variation of the sample

at the I2M laboratory. As it will be seen, results do not differ significantly from those obtained using the 3ω on annealed samples.

Measuring the thermal conductivity and TBR of thin layers at high temperature has sense if followed by a structural and chemical analysis of the investigated samples. The complementary structural analysis by Raman, XRD, XRR, TXRF and chemical analysis Tof-SIMS were performed in order to examine the non-destructive characteristics of the experimental thermal technique and help analyzing the results. Finally EDS and WDS measurements helped us to understand the chemical composition of the matter at very low scale. All these techniques are briefly described in the appendix of the manuscript.

4.2 Useful thermophysical properties for further studies

All the materials involved in this study have been already the subject of a characterization in terms of their density, specific heat, Debye temperature, thermal conductivity and group velocity for the transverse and longitudinal acoustic branches. The known properties have been reported in Table 3 along with the associated references.

The heat capacity and thermal conductivity vary within the investigated temperature range [RT-600°C] especially for the PCM. The Ge-Sb-Te has been largely studied and we use those results as a comparison with the measurements on the In-Sb-Te ternary alloy that is the subject of this work.

		$r(T)\left[\text{kg.m}^{-3}\right]$	$c_p(T)\left[\text{J.K}^{-1}\text{.kg}^{-1}\right]$	$Q_D\ [\text{K}]$	$k(T)\left[\text{W.K}^{-1}\text{.m}^{-1}\right]$	$v_l\ \left[\text{m.s}^{-1}\right]$	$v_t\ \left[\text{m.s}^{-1}\right]$
Pt [1][2] [8]		21450@300K 23820@800K	130@300K 144@800K	240	69@300K	4174	1750
In [1] [2]		7310@300K	238@300K		81.6@300K	2460	710
Sb [1] [2]		6696@300K	207@300K		18.42@300K	3140	1800
Te [1] [2]		6245@300K	201@300K		1.7@300K	3360	2260
$In_3Sb_1Te_2$ [16][17]		6310@300K	210@300K	190	-	3100	1900
$Ge_2Sb_2Te_5$ [39][40]	α	5870	218	136	0.2	2250	1350
	fcc	6270	205	197	0.45@300K 0.8@570K	3190	1914
	hcp	6390	201	198	0.8@570K 1.8@670K	3300	1980
α-Si_3N_4 [12][13][14][15]		3200	400	1130	0.8	620	1030
α-Al_2O_3 [4] [5][6][7]		2950@300K 3050@800K	755@300K 1165@800K	390	1.5@300K 3.1@800K	10890	6040
α-SiO_2 [9][10][11]		2200@300K 2650@800K	787@300K 1230@800K	552	1.38	6633	4038
Si [1] [2]		2300 (705+0.428 *T*)		645	983 $T^{-0.4737}$	8945	5341

Table 3: Thermophysical properties for Pt, In-Sb-Te, Ge-Sb-Te, Si_3N_4, Al_2O_3, SiO_2 and Si.

The dielectric materials are deposited in their amorphous structure. Some of their thermal properties vary significantly in the swept temperature range as reported in the Table above.

The mechanical properties are not reported (although the group velocities are connected with the elastic constants tensor).

4.3 IST film deposition

For both the 3ω and MPTR the IST was deposited in the same way. The depositions were performed at MDM laboratory using the MOCVD facility. For the deposition process, these following precursors were employed for the IST deposition: *trimethylindium-solution* $In(CH_3)_3$ for In, *trisdimethylaminoantimony* $[N(CH_3)_2]_3Sb$ for Sb and *diisopropyltelluride* $(C_3H_7)_2Te$ for Te. The bubbler temperature for all the precursors was kept constant at 20°C during the depositions. The precursor vapors were transported to the reactor with the help of N_2 carrier/process gas with a total flow of 4 L/min.

In the process of thin film formation, the temperature, pressure and precursors flow were optimized so as to achieve high film flatness, compact grains morphology, and good step coverage. This can be obtained by sensibly reducing the deposition temperature, in order to limit the formation of crystalline grains (when the deposition temperature is below that of crystallization). As a matter of fact, the chemical deposition of thin film mostly depends on the temperature condition.

Herein, samples were grown on Si/SiO_2 (thermal, 50 nm thick) substrate in the 220°C–350°C temperature range and working pressure condition varied from 35 to 100 Pa that made thin film thickness down to 30 nm. The deposition temperature should be less than the expected crystallization temperature at 280°C (for [312] composition of the IST) in order to obtain amorphous conformal layers. In the Figure 34 a-b, samples were grown at 220°C and 250°C, these ones exhibited grainy morphology, because of unsatisfactory precursor dissociation, thus a low deposition rate. Higher conformity and continuity of the deposited IST film were reached when increasing up to 260°C (Figure 34 c). On the other hand, samples grown at 350°C (Figure 34 d) showed nanostructured morphology and non-continuous layers were grown. In this case the strong tendency to form crystal grains was evident. Therefore, for the first step of testing, the possibility to obtain a conformal and smooth morphology with improved surface roughness for films grown at 260°C when the

substrate surface is treated with the *trisdimethylaminoantimony* $[N(CH_3)_2]_3Sb$ precursor was shown.

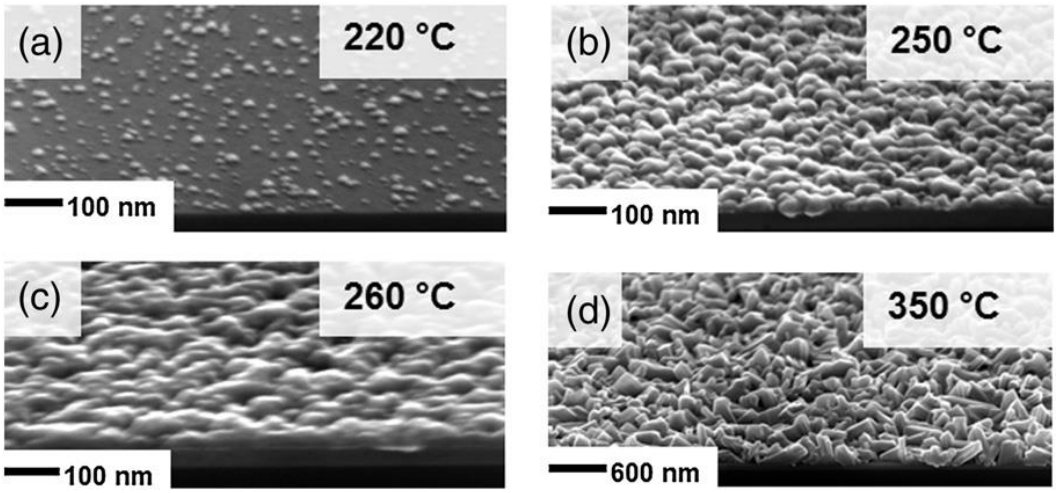

Figure 34: The SEM image shows the effect of the deposition temperature on the surface morphology of IST on SiO2 substrate.

As described in the previous chapter, the 3ω and MPTR methods allow measuring the thermal resistance of the stack composed from the deposited layers, including the IST layer. In order to achieve the thermal conductivity of the IST film, we need to deal with different thicknesses of the IST layer. Therefore, the deposition time was varied for each sample in order to obtain different thicknesses of the IST thin film.

We obtained two compositions of In-Sb-Te: $In_3Sb_{2.7}Te_{0.8}$ (A) and $In_3Sb_{2.5}Te_{1.2}$(B), corresponding to a Te content of 12 at.% and 17 at.%, respectively by acting on the Sb/Te ratio, which is 0.633 in the case of sample #434 and 1.722 in the case of sample #440.

Therefore, four thicknesses were deposited for the two stoichiometries: $In_3Sb_{2.7}Te_{0.8}$ (30, 50, 65, 90 nm) and $In_3Sb_{2.5}Te_{1.2}$ (30, 50, 70, 105 nm). The deposition time, film thickness and exact composition measured by TXRF are shown in Table 4.

The samples were analysed by TXRF and the chemical composition of each sample was calculated. The thickness of the samples was measured by cross-section samples observation via SEM.

Sample name	Deposition time, min	Thickness, nm	TXRF Chemical composition		
			In	Sb	Te
MOIST434	165	90	3	2.75	0.77
MOIST435	125	65	3	2.82	0.75
MOIST436	75	30	3	2.64	0.82
MOIST437	100	50	3	2.85	0.72
MOIST438	130	50	3	2.33	1.34
MOIST439	250	105	3	2.42	1.19
MOIST440	180	70	3	2.44	1.17
MOIST441	90	30	3	2.41	1.18

Table 4: The detailed of the IST film deposited on Si/SiO_2 subtrate by MOCVD.

4.4 Thermal characterization using the 3ω technique

4.4.1 Sample preparation

We prepared stacks of different combinations of top-dielectric/IST/bottom-dielectric layers. As previously said, the silicon dioxide layers employed as bottom dielectric were obtained by thermal oxidation from the wafer manufacturer. The top SiO_2 layers were thermally evaporated in a vacuum chamber. All alumina (Al_2O_3) layers were produced by atomic layer deposition (ALD) in a flow-type reactor, employing Trimethyl-aluminium and H_2O as precursors, and by means of a process optimised for the growth of thick (30 and 50 nm) films at 100 °C (the reader can also have a look on the work of A. Cappella concerning the Al_2O_3 deposited by ALD [7]). Bottom Si_3N_4 dielectric films (60–200 nm thick) were deposited by plasma-enhanced chemical vapour deposition, at 380°C, on thermally oxidized SiO_2 (10 nm). Finally, the effect of heat treatment (480°C for 10 min) was investigated on samples of both compositions sandwiched between SiO_2. The thermal annealing was performed in a tube

furnace in nitrogen flow at 0.2 bar. Obviously, as the IST thickness was varied, that of the dielectric layers remains constant.

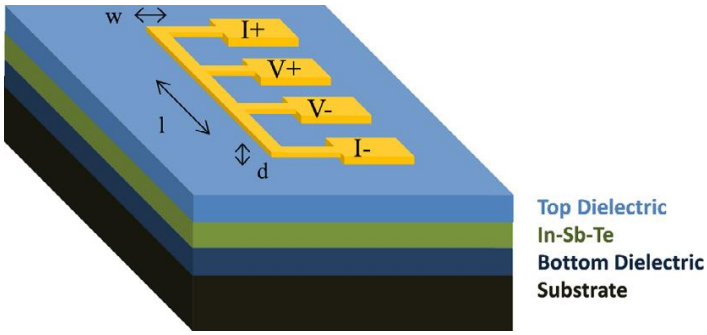

Figure 35: Layout of the samples for 3ω experiment.

In order to perform the 3ω experiment, a metal strip (Au, 1 mm long, 20 µm wide, 230 nm thick) was deposited by evaporation and defined by a photolithographic process, along with four metal pads to provide connection to the sample holder of the instrument. The sample layout is shown in Figure 35.

The symbols used for the investigated samples in terms of detailed thermal treatment conditions and the combinations of top and bottom dielectric of all samples are summarized in Table 5. The IST film thickness was varied, whereas the dielectric thickness was kept constant for all samples, except for those prepared with Si_3N_4 bottom dielectric, where the thickness of the former was always 45 nm and the latter was varied.

Top dielectric	SiO_2 80nm	SiO_2 80nm	SiO_2 80nm	SiO_2 80nm	SiO_2 80 nm	Al_2O_3 30 nm
In-Sb-Te	A ■ as deposited $In_3Sb_{2.7}Te_{0.8}$	A □ annealed $In_3Sb_{2.7}Te_{0.8}$	B ● as deposited $In_3Sb_{2.5}Te_{1.1}$	B ○ annealed $In_3Sb_{2.5}Te_{1.1}$	B ▲ as deposited $In_3Sb_{2.5}Te_{1.1}$	B ▼ as deposited $In_3Sb_{2.5}Te_{1.1}$
Bottom dielectric	SiO_2 50nm	SiO_2 50nm	SiO_2 50nm	SiO_2 50nm	Si_3N_4 30-200 nm	Al_2O_3 50 nm
substrate	bulk Si	bulk Si	bulk Si	bulk Si	bulk Si	bulk Si

Table 5: symbols used for the investigated samples: batch, composition and thickness as well as thermal annealing conditions (filled symbol = RT, empty symbols = ann. At 480°C), type and thickness of the top & bottom capping dielectric layers.

4.4.2 Structural analysis of the samples

These samples were analysed both as deposited and after thermal annealing at 480 °C during 10 min under Ar flow. XRD analysis on both as-deposited and annealed samples is reported in Figure 36. As-grown IST showed a cubic $InSb_{0.8}Te_{0.2}$ phase + an amorphous Te component. The crystallographic structure of as deposited IST layers did not depend on the nature of the dielectric bottom layers. The lattice parameter was found to decrease with increasing Te content, as expected. After thermal treatment at 480 °C (higher than the crystallization temperature of $In_3Sb_1Te_2$), the batch A IST films became fully crystallized predominantly within the $InSb_{0.8}Te_{0.2}$ structure, with minor tetragonal InSb and cubic In-Te binary components. On the other hand, in batch B the $In_3Sb_1Te_2$ phase was also found to develop. In all thermally annealed IST compositions, the $InSb_{0.8}Te_{0.2}$ component of the XRD patterns was found to scale with the IST thickness.

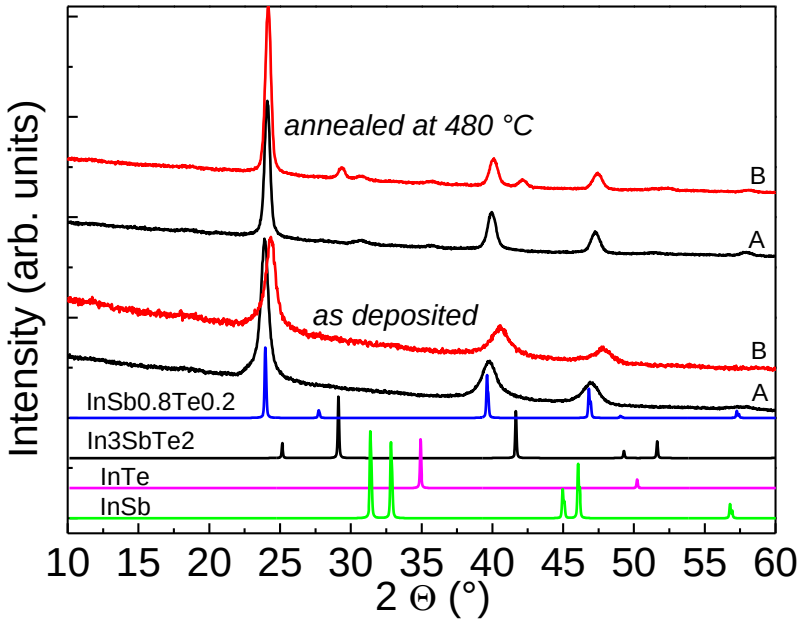

Figure 36: XRD analysis for as-grown and post-annealed (at 480°C) IST film.

The morphological properties of the dielectric/IST/dielectric stacks were also measured by XRR. Figure 37 shows experimental data and simulation of selected XRR patterns. The upper surfaces of all top dielectrics had a surface roughness of 2.0–2.2 nm, with the lowest values being obtained for Al_2O_3 deposited by ALD. The top IST/deposited dielectric interfacial roughness ranged within 2.0–2.3 nm for all samples, while the bottom dielectric/IST interface depended on the deposited dielectric: 0.7–0.9 nm for Si_3N_4, 0.4–0.5 nm for SiO_2 and 0.6 nm

for Al_2O_3. The SiO_2/Si_3N_4 interface had an interfacial roughness of 0.5 nm. Both IST batch A and B had the same upper and lower interfacial roughness with SiO_2. After annealing at 480°C, the upper IST/SiO_2 interfacial roughness and the upper SiO_2 surface roughness increased to 2.5–2.7 nm and up to 3.8 nm, respectively, while the lower SiO_2/IST interface maintained its low (0.4–0.5 nm) roughness value. This analysis has an absolute uncertainty of 0.1 nm per each interface.

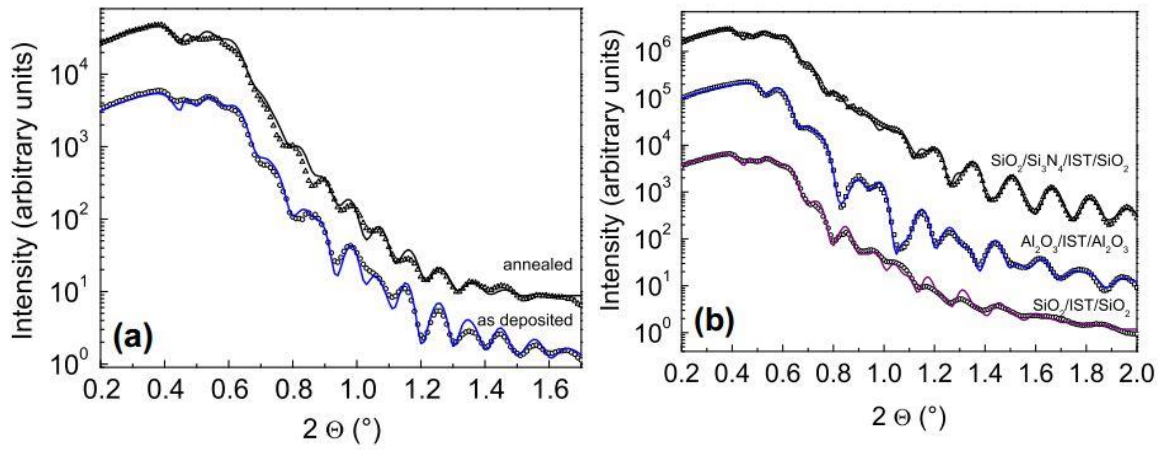

Figure 37: XRR data (symbols) and simulations (lines) of (a): as deposited and 480°C annealed 70 nm thick IST sandwiched between SiO_2; (b): as deposited IST, 48 nm thick, in contact with different bottom and top dielectric layers.

4.4.3 3ω Measurements

According to the investigated frequency range [100-3000] Hz, the heat penetration depth at the higher frequency ($\sqrt{a/pf}$, a being the thermal diffusivity) is much larger than the thickness of the stack constituted from all the thin films. Therefore, each layer behaves as a thermal resistance whereas the Si substrate can be considered as a semi-infinite medium. This leads to the representation of the heat transfer in the sample as described in Figure 38.

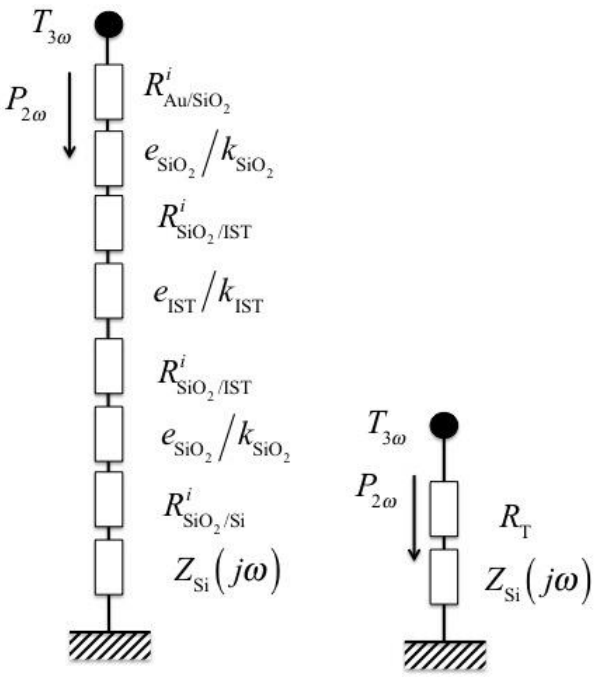

Figure 38: heat transfer in the sample during the 3ω experiment.

Therefore, the measured temperature is expressed according to the generated heat flux as:

$$T_{3w}(w) = Z(w) P_{2w} \tag{4.1}$$

As demonstrated in the chapter 3 (relation (1.35)), one has:

$$Z(w) = \frac{1}{p k b^2 2l} \int_0^{\infty} \frac{\sin^2(a\,b)}{a^2 \tanh\left(\sqrt{a^2 + \frac{jw}{a}}\, e_{Si}\right) \sqrt{a^2 + \frac{jw}{a}}} da + \frac{R_T}{4bl} \tag{4.2}$$

Where b is the heater strip half-width, l the measurement half-length between the two inner voltage pads and e_{Si} the Si substrate thickness.

Choosing SiO_2 for the dielectric layer, the thermal resistance of the stack is:

$$R_T = R^i_{Au/SiO_2} + \frac{e_{SiO_2}}{k_{SiO_2}} + R^i_{SiO_2/IST} + \underbrace{\frac{e_{IST}}{k_{IST}}}_{R_{IST}} + R^i_{IST/SiO_2} + \frac{e_{SiO_2}}{k_{SiO_2}} + R^i_{SiO_2/Si} \tag{4.3}$$

Another form of this relation is:

$$R_T = R^i + 2\frac{e_{SiO_2}}{k_{SiO_2}} + R_{IST} \tag{4.4}$$

The total boundary resistance being:

$$R^i = R^i_{Au/SiO_2} + R^i_{SiO_2/IST} + R^i_{IST/SiO_2} + R^i_{SiO_2/Si} \quad (4.5)$$

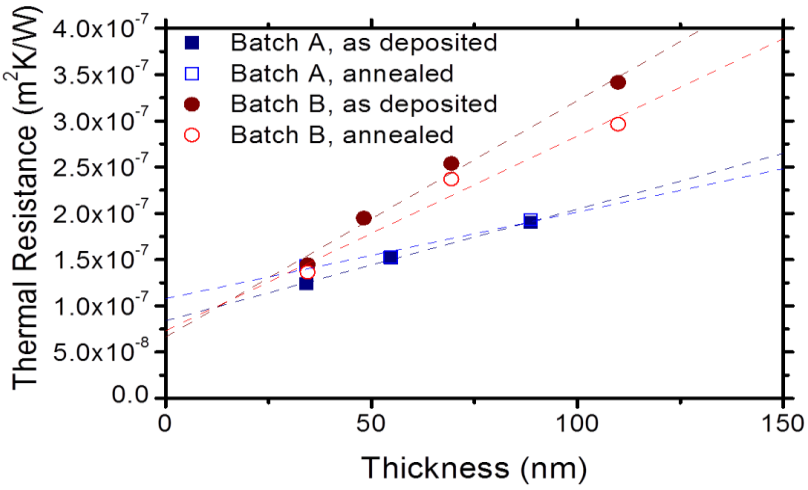

Figure 39: Thermal resistance $\left(R_T - 2e_{dielect}/k_{dielect}\right)$ versus IST thickness. SiO_2-capped composition A (squares) and B (circles) both before (full symbol) and after (hollow symbol) thermal annealing. [Symbols are consistent with those defined in Table 3]

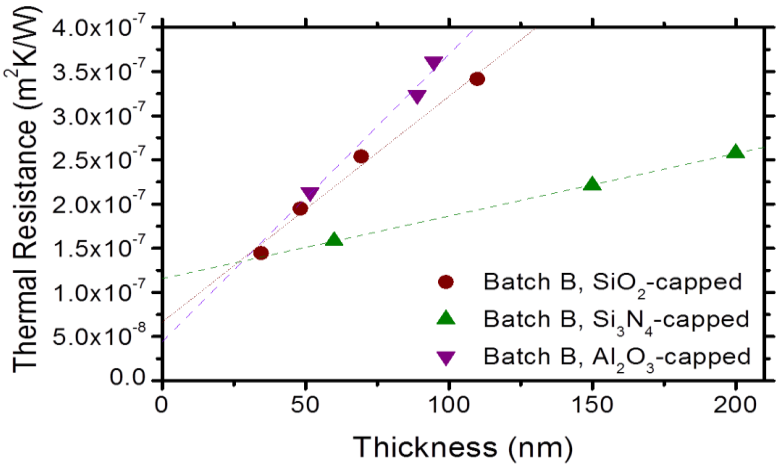

Figure 40: thermal resistance $\left(R_T - 2e_{dielect}/k_{dielect}\right)$ versus IST thickness. Composition B, as deposited, capped between: SiO_2 (circles), Si_3N_4 (upward triangles) and Al_2O_3 (downward triangles). [Symbols are consistent with those defined in Table 3]

The stack thermal resistance $\left(R_T - 2e_{SiO_2}/k_{SiO_2}\right)$ as a function of the IST thickness is represented in Figure 39 for the (A) and (B) samples capped with SiO_2 and in Figure 40 for the (B) samples capped with SiO_2, Si_3N_4 and Al_2O_3. A linear trend is extracted for each set of

data. Therefore, the intrinsic thermal conductivity is given as the reciprocal of the slope of the linear fit to the data, while the Y-axis intercept represents the total thermal boundary resistance R_i.

4.4.4 Discussion on the thermal conductivity

The intrinsic thermal conductivity k_{IST} of the IST films is deduced from the previous thermal measurement using relation (4.4). As reported in Figure 41, k_{IST} is noticeably higher in the Te-poor composition (0.83 $W.m^{-1}.K^{-1}$) than in the Te-rich one (0.39 $W.m^{-1}.K^{-1}$). The thermally annealed samples, which exhibited a higher crystallinity, also had a higher thermal conductivity, as expected. However, upon thermal annealing, the thermal conductivity increased more markedly in batch A (from 0.83 to 1.1 $W.m^{-1}.K^{-1}$) than it did in batch B (from 0.39 to 0.48 $W.m^{-1}.K^{-1}$).

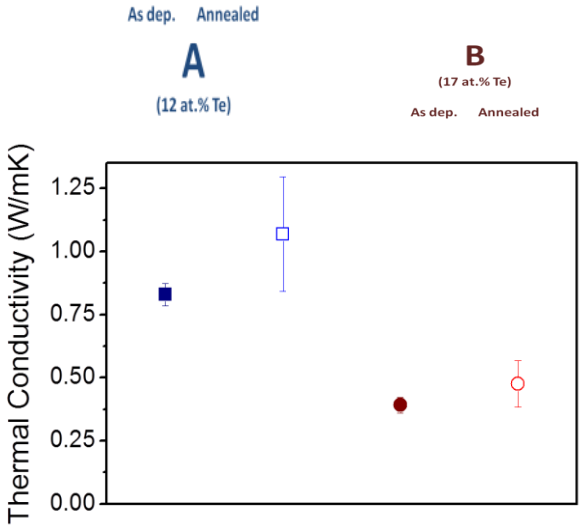

Figure 41: Thermal conductivity of the IST compositions investigated in this work and effect of the thermal treatment on the material. Te-richer compounds of IST (batch B, 17 at.%) was less thermally conductive than its Te-poorer counterpart (batch A, 12 at.%), regardless of the thermal treatment (both batches capped between silicon dioxide) . [Symbols are consistent with those defined in Table 3].

IST film capped between Al_2O_3 dielectric layers has roughly the same conductivity (≈ 0.3 $W.m^{-1}.K^{-1}$, not shown) as those in-between SiO_2, hence proving that the thermal conductivity value was intrinsic and did not depend on the neighbouring layers. More rigorously, this result demonstrates that the growth of the IST film is not influenced by the nature of the dielectric used as substrate. All these results have been published in [17].

4.4.5 Discussion on the thermal boundary resistance

Finally, the TBR is extracted from values of the measured thermal resistance extrapolating the linear regression to thickness equal to 0. As reported in Figure 42, our data indicated that the TBR at the SiO_2/IST/ SiO_2 boundaries ($2\,R^{i}_{SiO_2/IST}$) was 8.4x10^{-8} m^2.K.W^{-1} for batch A and 6.6x10^{-8} m^2.K.W^{-1}for batch B (assuming the TBR between the gold strip and the dielectric layer is negligible, Debye temperature of Au is 170 K). Both values increased to 10.8x10^{-8} and 7.3x10^{-8} m^2.K.W^{-1}, respectively, when these same samples underwent the 480 °C, 10 min., thermal annealing. Besides, the effect of a different dielectric on the boundary resistance was found to be weakly significant. Replacing SiO_2 with Si_3N_4 brought the TBR to 11.6x10^{-8} m^2.K.W^{-1}; whereby it was almost halved when using Al_2O_3 (4.4x10^{-8} m^2.K.W^{-1}). However, those results are in perfect agreement with the value for the Debye temperature for each dielectric material. Indeed, it is well known that the higher the mismatch between the Debye temperatures of superimposed layers, the higher the TBR. As reported in Table 1, it was thus expected to have the higher TBR between IST ($\Theta_D = 1130\,K$) and Si3N4 ($\Theta_D = 190\,K$) than with SiO_2 ($\Theta_D = 552\,K$) and Al2O3 ($\Theta_D = 390\,K$). This is well retrieved on the experimental results reported in figure 9.

In addition, we also observed that the TBR follows well the measured roughness. For each stack, we calculated the total roughness as the sum of the roughness of each of the three interfaces (top dielectric/IST/bottom dielectric). This value for the three dielectric layers has been reported on the second y-axis of figure 9 and it is clear that increasing, even slightly, the roughness leads to increase the TBR in a comparable way.

To summarize, two causes have been clearly identified that accounted for the TBR:

- The diffuse mismatch of phonon at the interface between two different adjacent layers, even more pronounced as the Debye temperature differs between both materials.
- The morphological roughness of the surface between the layers, which has a detrimental effect on the heat transfer.

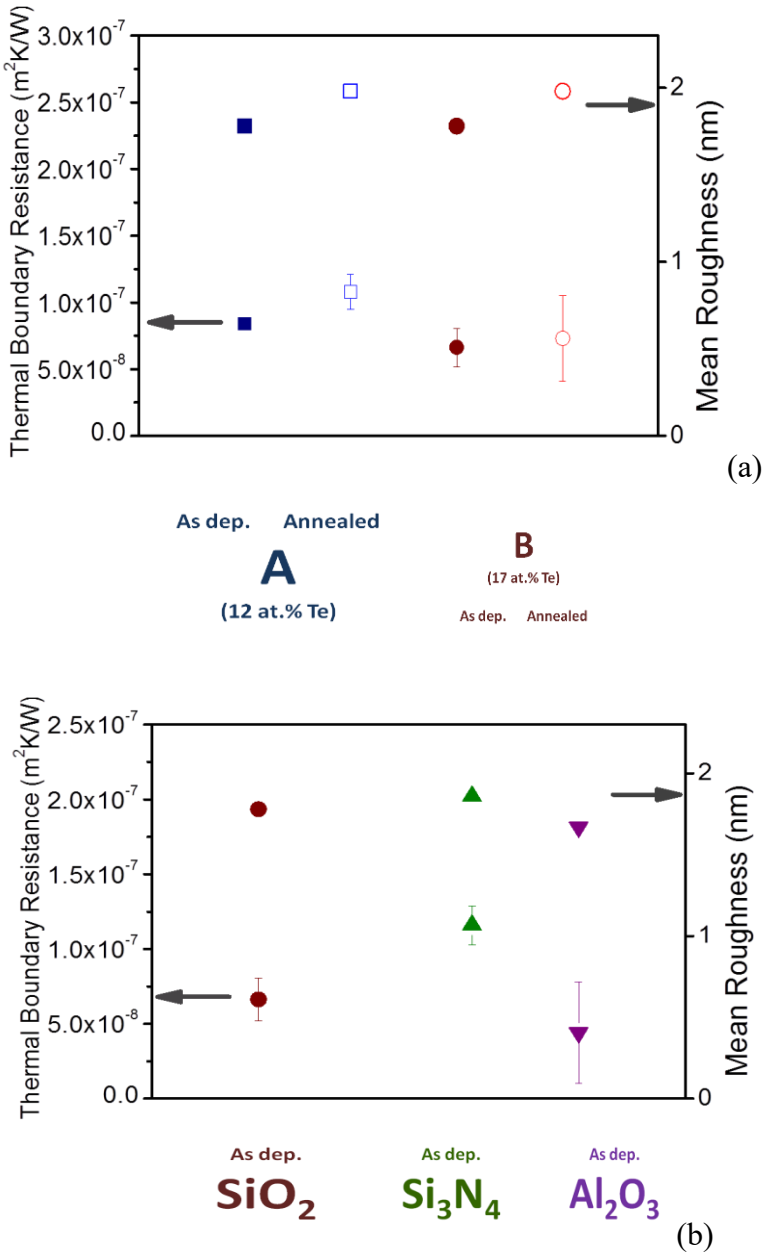

Figure 42: Relationship between thermal boundary resistance (left axis) and mean roughness (right axis) of full stacks of dielectric/IST/dielectric. (a) Results of SiO_2-capped batches A (blue squares) and B (red circles), as deposited (full symbols) and after thermal treatment (hollow symbols). (b) Results of the same batch B, sandwiched between SiO_2 (circles), Si_3N_4 (upward triangle) and Al_2O_3 (downward triangle).

Both A and B as deposited SiO_2-capped IST samples had nearly the same TBR, which was comparable to what found at the interface between crystalline-$Ge_2Sb_2Te_5$ and SiO_2 [40]. This result is not surprising since the thermal properties of both alloys are very close (especially their Debye temperature). Upon thermal annealing, the In-Sb-Te films became more thoroughly crystalline and their mean roughness increased, a phenomenon previously

reported on Ge-Sb-Te films. As a consequence, a greater TBR was measured in thermally annealed samples, regardless of composition. Such increase in TBR is less noticeable in batch B than in batch A.

All the results obtained using the 3ω method are summarized in Table 4.

Batch	Te at. %	Thermal treatment	Capping layers	k_{IST} [W/mK]	TBR [x10^{-8} m^2K/W]	Mean Roughness [nm]
A	12	-	SiO_2	0.83 ± 0.04	8.40 ± 0.41	1.8
A	12	480°C	SiO_2	1.07 ± 0.23	10.8 ± 1.30	2.0
B	17	-	SiO_2	0.39 ± 0.03	6.63 ± 1.44	1.8
B	17	480°C	SiO_2	0.48 ± 0.09	7.30 ± 3.20	2.0
B	17	-	Si_3N_4	*	11.6 ± 1.30	1.9
B	17	-	Al_2O_3	0.48 ± 0.09	4.40 ± 3.40	1.7

Table 6: summarize of all the results obtained using the 3ω method.

4.5 Thermal Characterization using Modulated Photothermal Radiometry (MPTR).

4.5.1 Introduction

In this second part, we study the effects of phase transformation on the thermal conductivity of InSbTe thin film by using the modulated photothermal radiometry (MPTR, described in chapter 2) from room temperature to 550° C and going back to RT. All the experiments have been carried out at I2M laboratory using the MPTR facility. Experiments have been repeated at least three times for each sample.

As when using the 3ω experiment, the heat penetration depth during the MPTR characterization is higher than the thin film thickness under investigation whatever the frequency in the investigated range. Therefore, the thermal characterization required having

different In-Sb-Te film thicknesses e_{IST}. We thus used the same two batches presented previously: A [$In_3Sb_{2.7}Te_{0.8}$ (30, 50, 65, 90 nm)] and B [$In_3Sb_{2.5}Te_{1.2}$ (30, 50, 70, 105 nm)]; each being constituted with four IST film thicknesses for the two stoichiometries. Let us note that we will focus only on the SiO_2 dielectric material in contact with the IST, meaning we will not consider the other dielectric materials (Al_2O_3 and Si_3N_4). Let us remind that a Pt capping layer is required also for the MPTR at high temperature. This metallic layer has been deposited by sputtering and thickness is about 50nm.

The final stack configuration is represented as in Figure 43 where TBR denotes the thermal boundary resistance at the interface between each layer.

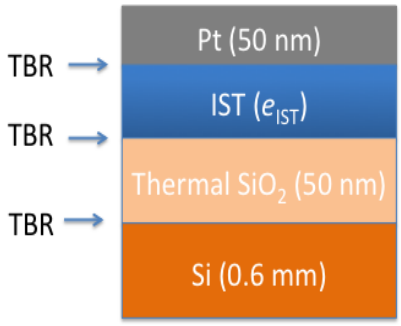

Figure 43: Layout of the sample for the MPTR characterization.

4.5.2 Structural and chemical analysis

X-ray diffraction (XRD) analysis (see Figure 44) has been performed at MDM. As for the sample used for the 3ω technique, it demonstrated that as-deposited In-Sb-Te layers are formed by a mixture of polycrystalline face centred cubic $InSb_{0.85}Te_{0.15}$ phase and a Te-rich amorphous component.

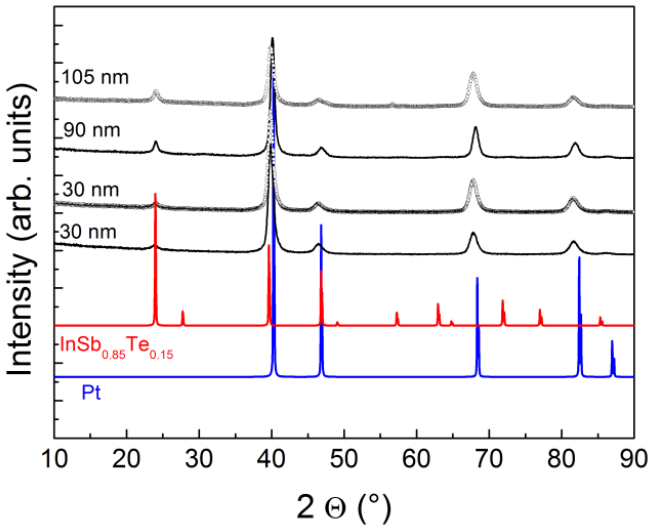

Figure 44: XRD measurements on as-deposited In-Sb-Te sample (MOIST439).

Time of Flight Secondary Ion Mass Spectroscopy (Tof-SIMS) measurements (carried out at MDM) are reported in Figure 45. They reveal a very sharp interface between Pt and IST, demonstrating no species inter-diffusion between as-deposited In-Sb-Te and Pt.

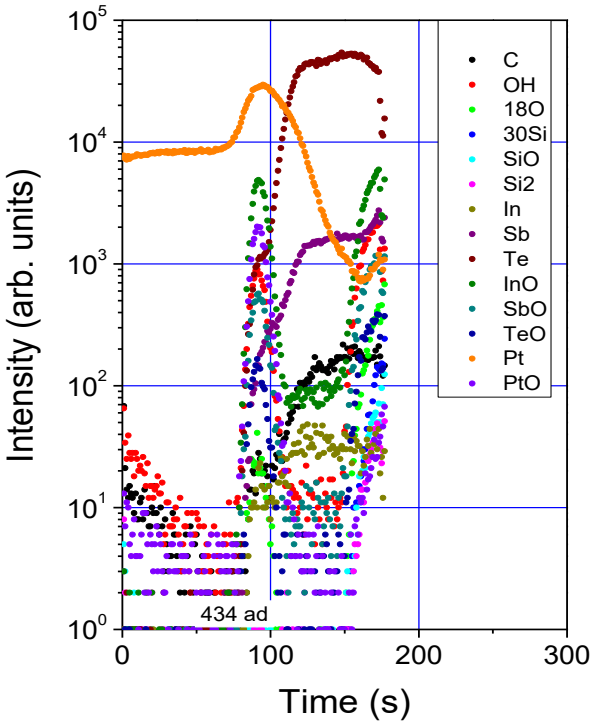

Figure 45: Tof-SIMS measurements on as-deposited In-Sb-Te (MOIST 439).

We heated the sample up to 550°C under Argon flow in the furnace used within the MPTR experiment. We then explore the sample surface using a MEB each 20°C sampling temperature. We observed that the Pt capping layer started to deteriorate from 300°C and was even more pronounced at 480°C as reported on the image in Figure 46. This result was surprising since we never observed such a degradation before 450°C (as we experienced for the characterization of the GST alloy). Let us note also that the temperature where the degradation starts is very close to the phase change temperature (about 280°C). However, the degradation appears as if some very small areas of the deposit have been removed randomly on the surface. It must be also accounted for a possible low adhesion between the Pt and the IST although there is no information in the literature about it. As observed on the figure at different optical magnification, the IST with high Te content deteriorates more than that with the low Te content. Using EDS, we verified that the IST layer was always on the substrate even that the Pt removed from the surface.

IST 435 (low Te)	IST 438 (High Te)
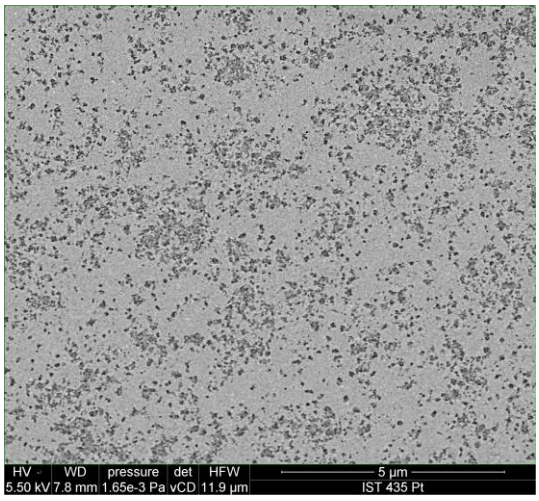	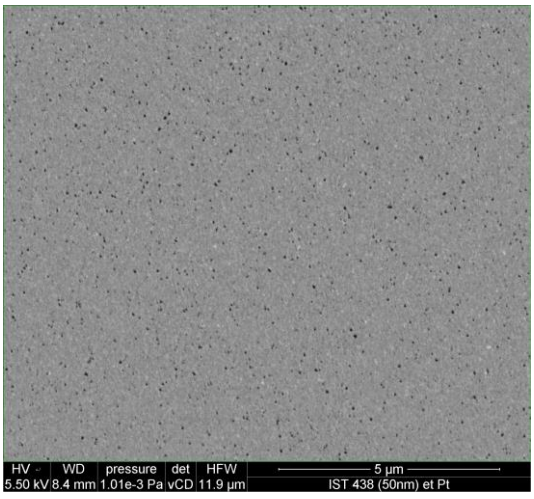

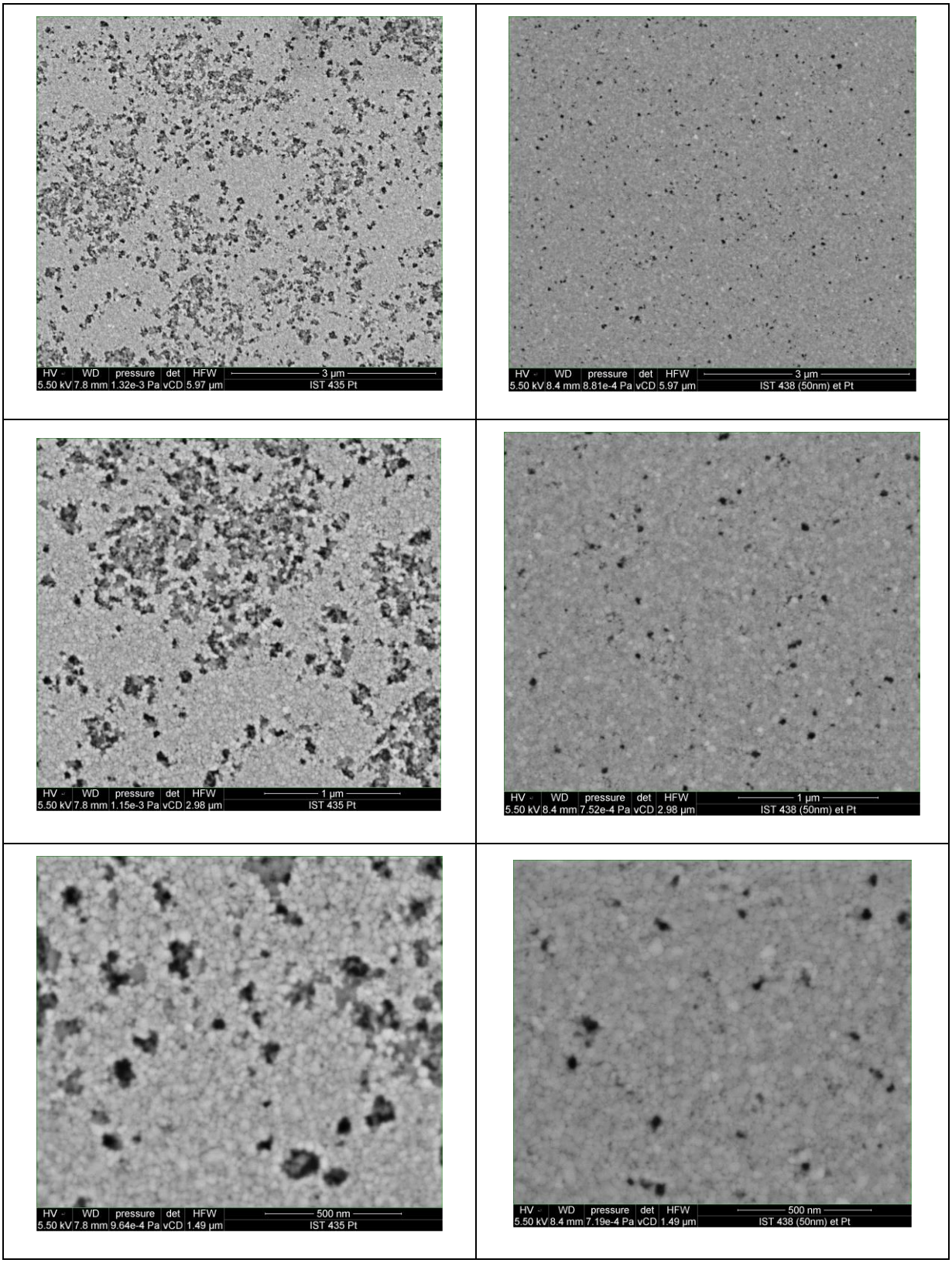

Figure 46: The Pt layer is thermally affected at 480°C annealing temperature. However, we observed that this degradation seems to be relevant starting from 300°C. Images obtained by MEB, at different scales, showed that the IST with low Te content is more affected than the one with high Te content.

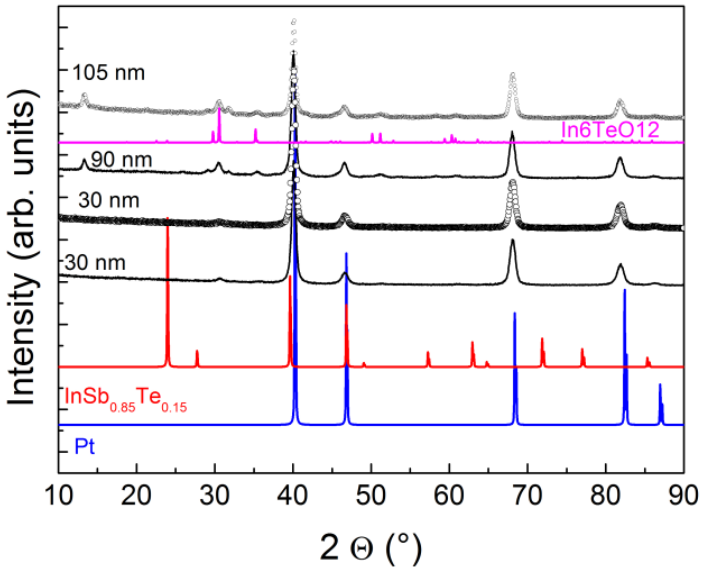

Figure 47: XRD patterns of In-Sb-Te (MOIST439) annealed at 550°C.

We performed XRD measurements on the annealed IST 439 (high Te) sample at 550°C that are reported in Figure 47. It appears that the only composition that allows retrieving the measurements is In_6TeO_{12} that thus demonstrates the In-Sb-Te film is fully oxidized.

On the other hand, Time of Flight Secondary Ion Mass Spectroscopy (Tof-SIMS) performed after annealing up to 550 °C on the same sample (see Figure 48) clearly reveals a very significant species inter-diffusion between In-Sb-Te and Pt, as well as the presence of oxygen migration. In conclusion, XRD and ToF-SIMS experiments showed that the In-Sb-Te sample with high Te content, annealed at 550°C, is fully oxidized due to massive Pt-In-Sb-Te species inter-diffusion allowing oxygen migration through the Pt film. Species inter-diffusion was also observed at the interface between $Ge_2Sb_2Te_5$ and Pt (as reported in [40]). But, this phenomenon was not critical with regards to the thermal conductivity measurement of the GST, contrary to what is observed on the IST. However, the higher temperature reached for the GST was 350°C, whereas it is 550°C for the IST, that makes a significant difference in terms of thermal budget viewed by the sample. It must be also noted that SEM observation revealed that a better Pt surface was obtained when the annealing is performed on the furnace of the MDM. It means that the sample placed in the furnace at I2M, under the MPTR facility,

was more contaminated despite of the Ar continuous flow. This suggests that the Ar flow was not uniform enough inside the furnace.

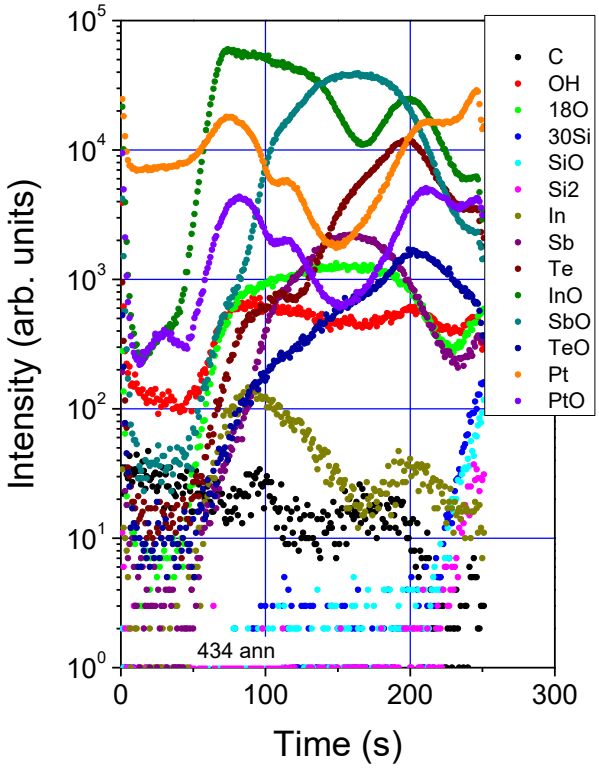

Figure 48: Tof-SIMS measurements on annealed In-Sb-Te (MOIST439) at 550°C.

Temperature dependent Raman analysis was performed on the IST samples. The measurements were carried out at I2M (MACAM platform) from room temperature up to 480°C. The temperature rate was 20°C/min with a plateau of 2 minutes in order to stabilize the temperature before data acquisition (each spectrum acquisition took about 5 minutes). This was thus fully consistent with the on-going thermal regime that typifies a MPTR experiment. It shall be noted that the annealing temperature could be slightly less than the one monitored by the furnace controller since a copper layer was put between the sample and the furnace heating element. Therefore a calibration was performed to minimize the unwanted effect approach

The first heating experiments were run under argon flow, first using a x5 objective and then with a higher magnification objective (x20). In both cases the samples was fitted into a micro

furnace comprising a window of BaF_2. Before presenting the results, let us remind the peak values for the concerned materials or possibly formed materials in Table 7.

Bond vibration	Excitation wavelength								References
Sb-Sb		115			152-157				[18][19]
		113			153				[20]
	780 nm	113			149		186	300	R050654 [21]
	785 nm				150	163			R070318 [21]
Te (am)					150 (large)				[22][19][23]
Te (c)			123	141		174			[24][25]
	780 nm			138				212	R060136 [21]
	785 nm					165		264	R070376 [21]
		102.2	119.7	139.5					[26]
InSb						178-180	189-191		[18][27]
						180	190		[20]
InTe			123	136					[24][28]
α-In_2Te_3	514.5 nm	103	125	142	157		194	225	[29][30]
	514.5 nm	105	123	143	158	182	194		[29][31]
	514.5 nm	103	125	147			194		[29][30]
	1064 nm	110	130		164		197	227	[29]
Sb_2Te_3 (am)					150 (large)				[19]
Sb_2Te_3 (c)	514.5 nm		122	141		163.6		265.5	[32]
		113				166			[33]
		112				165			[34]
In_2O_3	785 nm	110	131					312 ...	[35]
	1064 nm						200	220...	[36]
	532 nm		131					308...	[37]
Sb_2O_3	632.8 nm			143			191	218...	[38]

Table 7 : Raman peak values for amorphous and crystalline Te, Sb-Sb bound, InSb, InTe, In_2Te_3, Sb_2Te_3, In_2O_3 and Sb_2O_3 compounds. (am= amorphous ; c=cristallized)

The Raman spectra of the two as-deposited IST compositions (A and B *cf.* Table 2) obtained with a x50 magnification are represented in Figure 49. The non-characteristic peak at 0 cm^{-1}

is a Rayleigh residual that was not filtered by our edge filter. In addition the peak at 514 cm^{-1} is characteristic of the Si wafer. Let us now move to the peaks of interest. The major (bimodal) peak centred at around 184cm^{-1} corresponds to the two InSb bonds vibration at 178 and 189 cm^{-1}[18]. The peak at around 123 cm^{-1} expresses the In-Te vibration. Last, we have a quite large peak centred at about 150 cm^{-1} due to the amorphous Te (150 cm^{-1}).

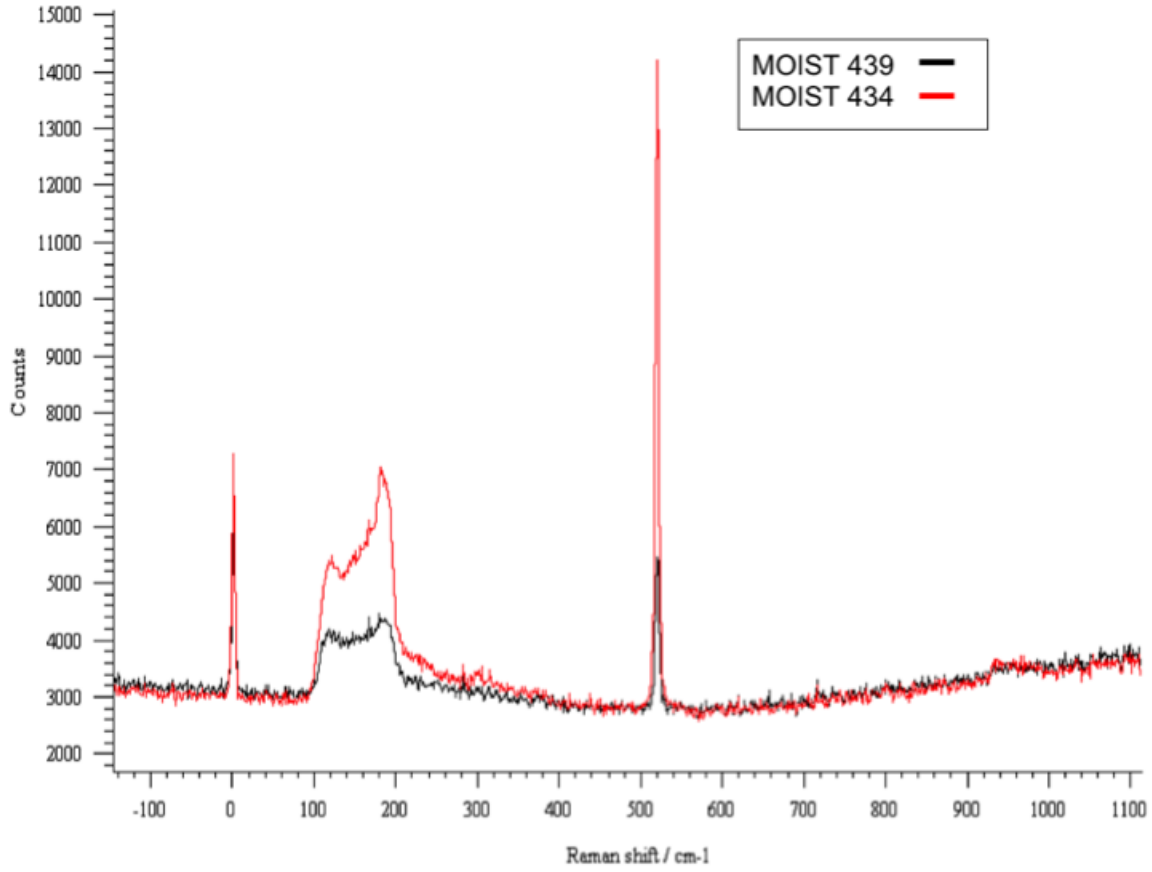

Figure 49: Raman measurements of IST at room temperature (sample 439 and 434 in Table 4)

Data obtained with the x5 objective are reported in Figure 50. No variations are found in spectra registered from room temperature up to 340°C. However, when the temperature reaches 360°C, a new peak appears at 141 cm^{-1} that corresponds to Te crystallization mainly. When increasing temperature up to 440°C, this peak develops and shifts towards 136 cm^{-1}. The development of that part of the spectrum centred at about 123 cm^{-1} supports a better organisation between In and Te compounds. In parallel, starting at 420°C, the appearance of a shoulder at around 115 cm^{-1} expresses the vibration of the Sb-Te bond. We may tentatively interpret the latter point as follows: the Sb-Te bonds may reflect the formation of crystallized Sb_2Te_3.

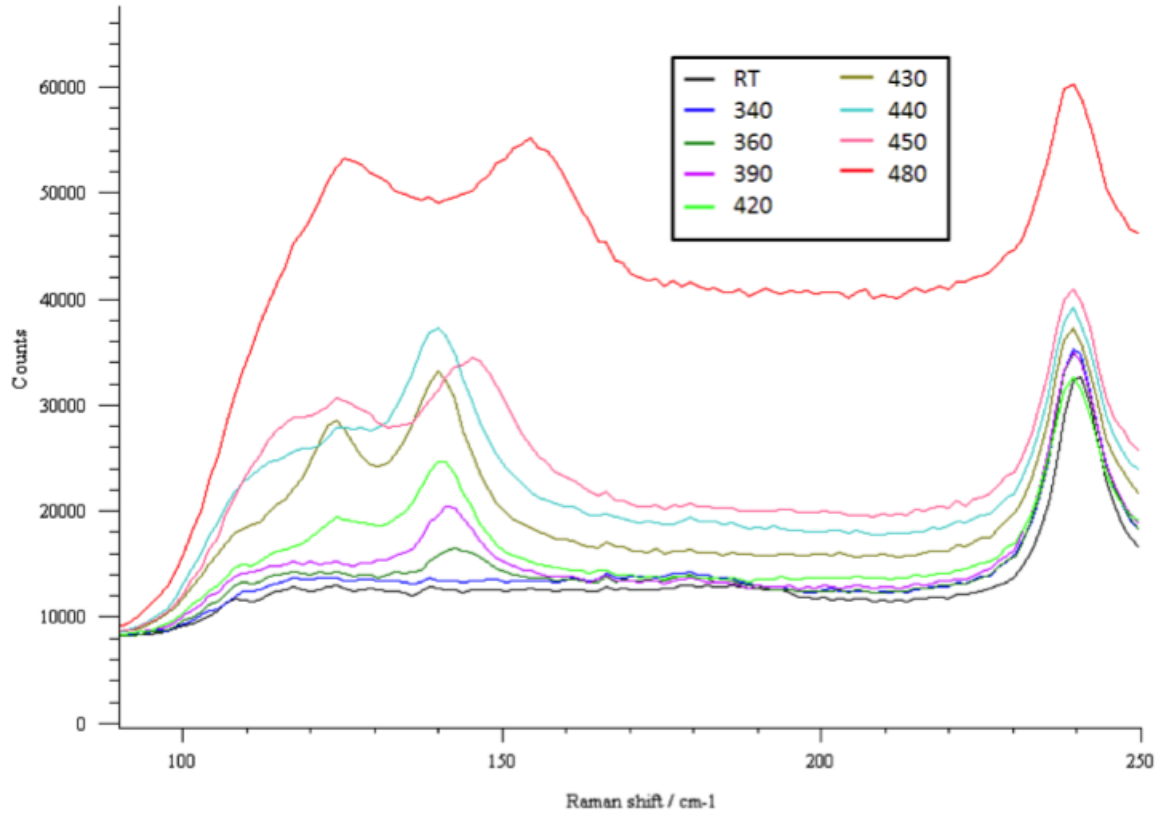

Figure 50: First in-situ Raman measurement for $In_3Sb_{2.5}Te_{1.2}$ (sample 439 in Table 4)

Over the temperature range 450°C - 480°C, new peak appears at about 145 cm^{-1} and shift towards 155 cm^{-1}. These peaks can be tentatively related to the increase implication of Sb in new bonds of e.g. Sb-Sb or Sb-Te. Conversely this peak can simultaneously express the formation of In_2Te_3.–In this experiment we were not able to see clearly the evolution of the original InSb peak at around 185 cm^{-1}. This may be due to the use of a low magnification objective (x5) and/or to fluorescence.

The same experiments have been repeated using a x20 long working distance objective, designed to be used with a quartz window for the furnace. Results are reported in Figure 51 that confirm those obtained with the smaller magnification. However, as shown in the figure, we reached a higher spectral resolution. In addition, during this experiment we removed the copper layer between the sample and the furnace and we replaced it with a thinner sapphire layer (100 µm thick). This allowed us a better confidence about the fact that the temperature reached by the sample was that of the controller.

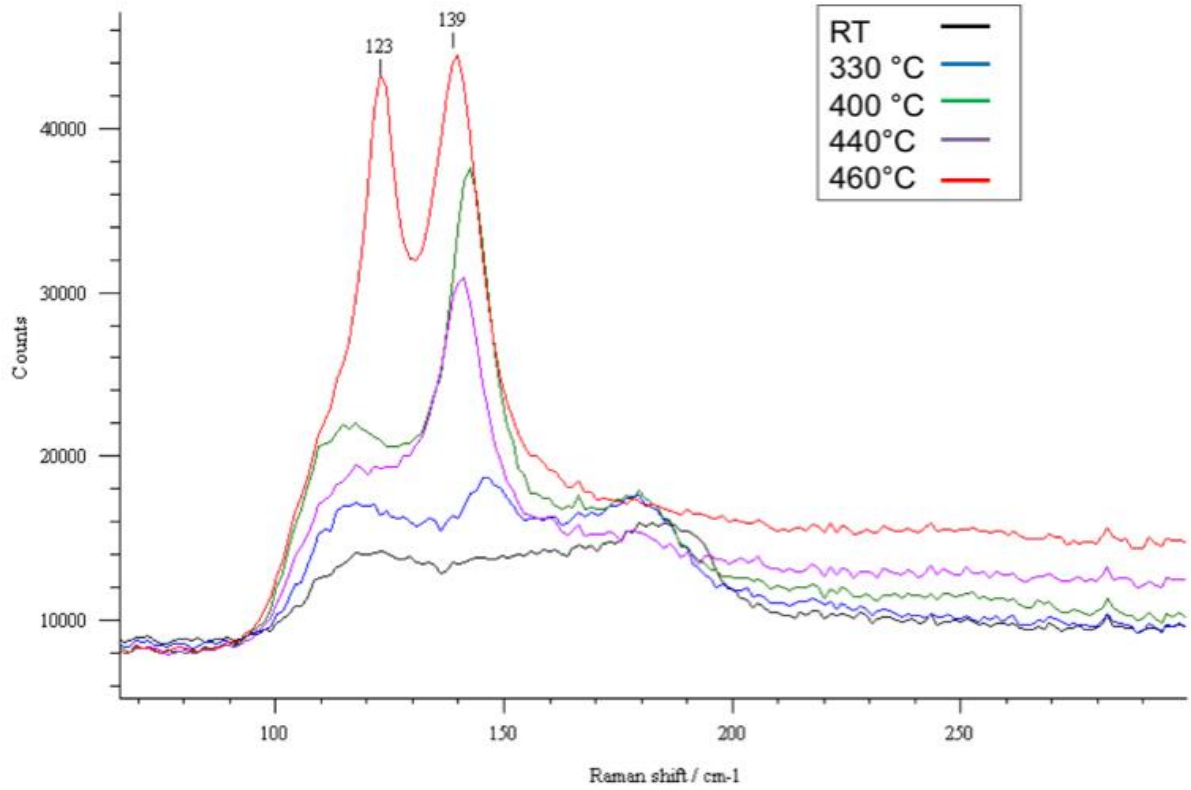

Figure 51: Second in-situ Raman measurement for $In_3Sb_{2.5}Te_{1.2}$ (sample 439 in Table 4)

The Raman spectra presented in Figure 51 suggest the following main comments:

- At **330°C**: Organisation of the Te-Te bonds - Appearance of a peak at 146 cm^{-1}. As it will be viewed after, this structural change is remarkably correlated to the sharp increase of the thermal conductivity (Figure 72);
- Until **440°C:** Increase and shift of the peaks at 146 cm^{-1}. Increase of the peak at 123 cm^{-1} – Te crystallization and In-Te arrangement;
- At **460°C:** Strong evolution of the spectrum whose main features are: a strong peak centered at 139 cm^{-1} (extending up to 150 cm^{-1}) and a shoulder at 115 cm^{-1} expressing Sb-Te and Sb-Sb vibrations. Increase of the peak at 123 cm^{-1} reflecting more In-Te vibrations. All these spectrum characteristics support strongly that at 460°C In_3SbTe_2 is the dominant phase while $InSb_{0.8}Te_{0.2}$ becomes metastable and is much less present. This Raman-based interpretation is fully consistent with the XRD results discussed previously.

  The spectra suggest that if Sb_2Te_3 is present, it is in moderate quantity.

In Figure 52 we reported the data at RT, 460°C in-situ and those obtained when going back to RT. Results are commented according to the electrical resistivity reported in the Figure 53. The sample in its initial state (a), composed of a polycrystalline FCC $InSb_{0.8}Te_{0.2}$ phase with unbounded amorphous Te, shows the highest electrical resistivity. The lowest electrical resistivity (c) corresponds to the predominant crystallised structure at high temperature: In_3SbTe_2.

Let us now comment here the spectrum obtained when going back to room temperature. To within the two main peaks at 114 and 152 cm^{-1}, we clearly observe the spectrum characteristic of the metastable phase ($InSb_{0.8}Te_{0.2}$), which therefore appear again after cooling, confirming work by Fallica et al. (2013)[16]. The peaks at 114 and 152 cm^{-1} are clearly related to Sb-Sb bonds. This spectrum also shows the expression of In-Te bonds (InTe and In_2Te_3).

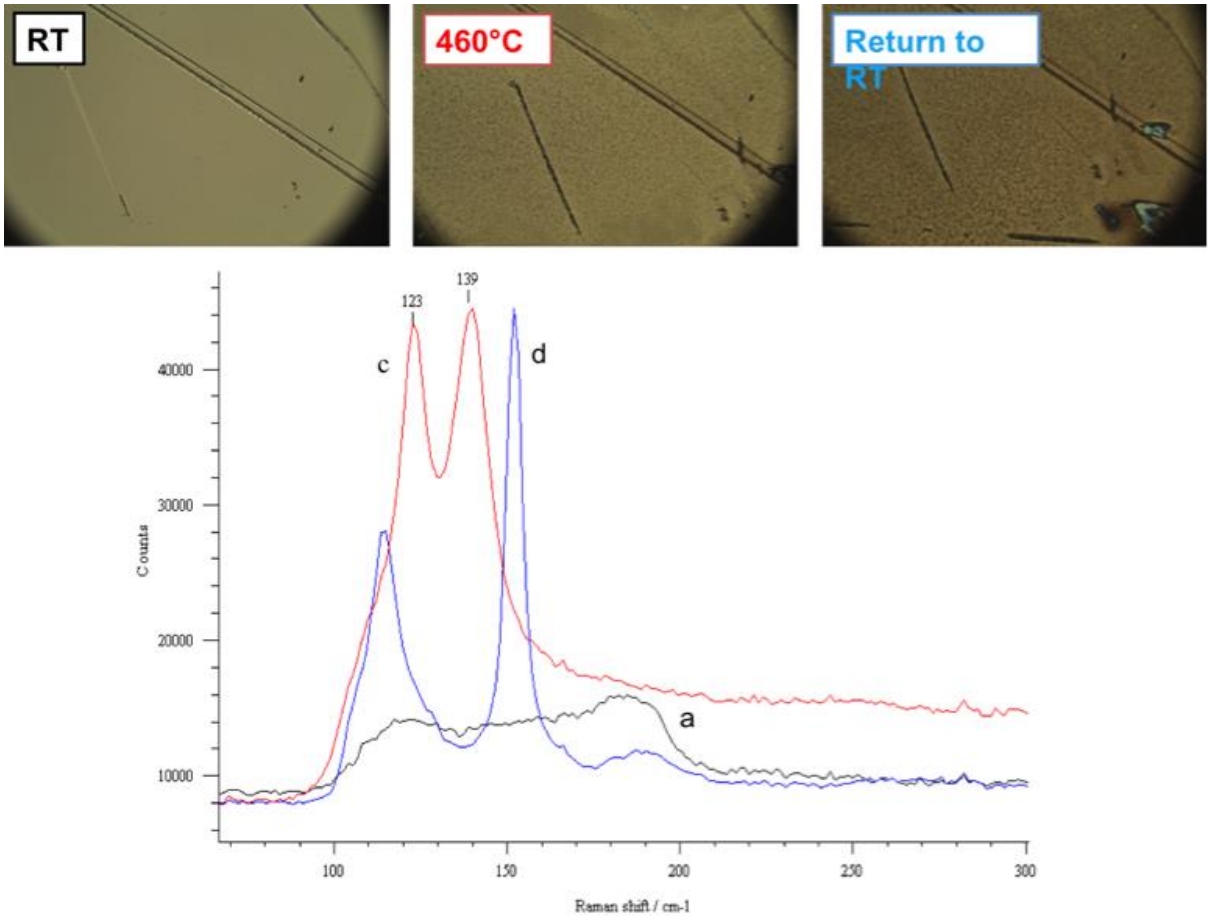

Figure 52: Raman spectra of $In_3Sb_{2.5}Te_{1.2}$. Spectra are labelled as (a), (c), (d) consistently with the notation adopted for the electrical resistivity (figure below).

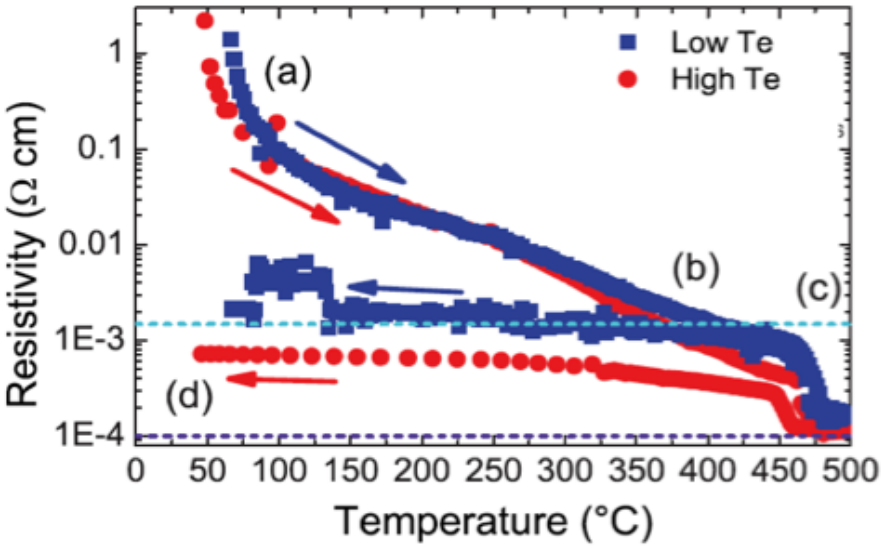

Figure 53 : From Fallica et *al.*, 2013. In red $In_3Sb_{2.5}Te_{1.2}$ (Cf figure 17). In blue $In_3Sb_{2.7}Te_{0.8}$. Electrical resistivity measured in-situ during heating experiment carried at 20°C/min. Dashed cyan line: resistivity of $InSb_{0.8}Te_{0.2}$ at room temperature. Dashed dark blue line: resistivity of In_3SbTe_2 at room temperature.

As further supported by Figure 53, the phase instability is well retrieved in the Raman data. More precisely, the spectra of the samples annealed below 400°C show the characteristic features of the original as-deposited materials. The spectra of samples annealed above 400°C express the presence of $InSb_{0.8}Te_{0.2}$ and a crystallized phase: In_3SbTe_2 (that typified a material at high temperature).

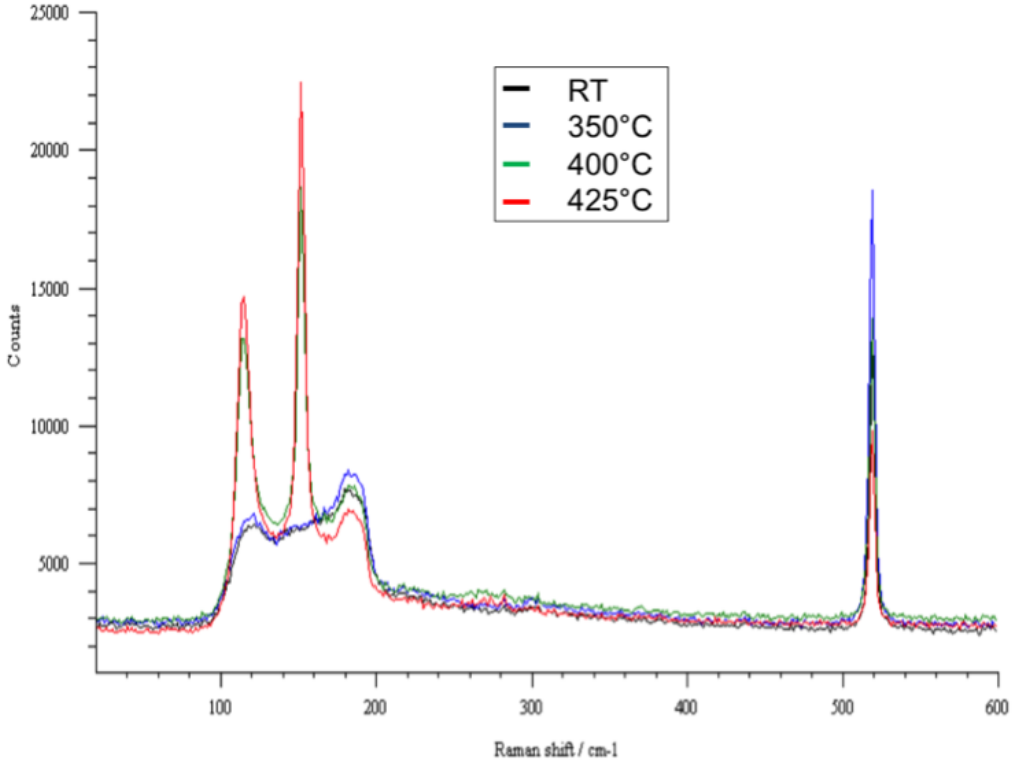

Figure 54: Raman spectra of IST with high Te content (sample 439 in Table 4)

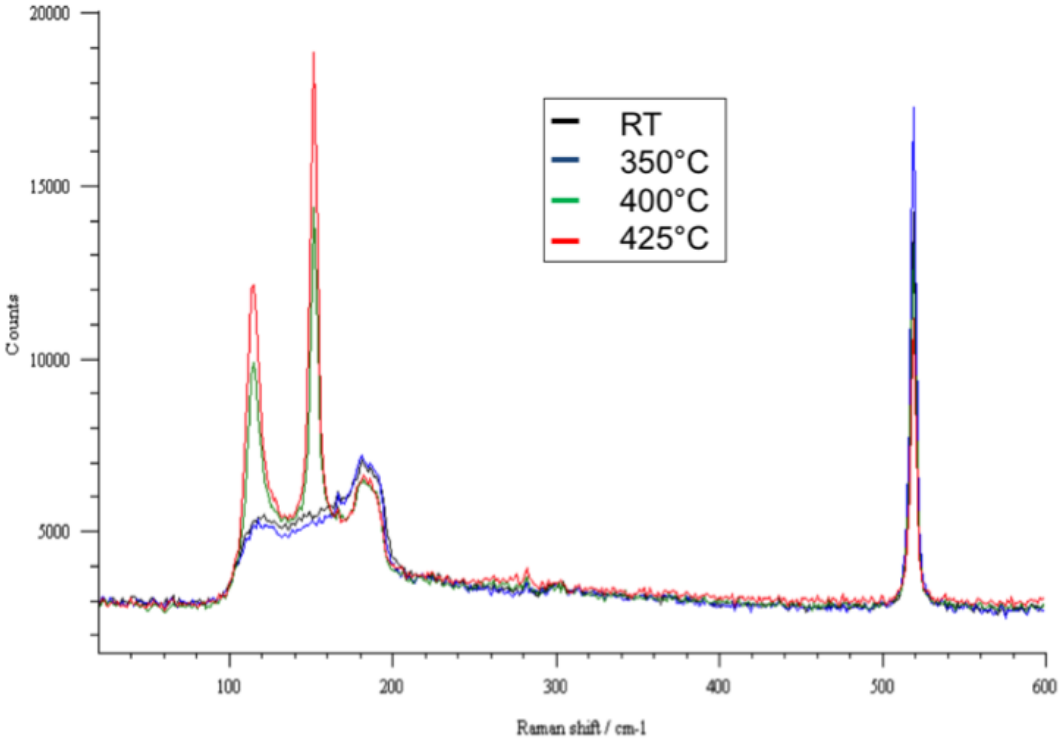

Figure 55: Raman spectra of IST with low Te content (sample 434 in Table 4)

Under the InVia Raman microscope, two types of zones could be observed when heating the sample in-situ up to 460°C: 1) Local zones showing evidence of a surface alteration and 2) local zones without any obvious alteration of the surface. These two zones were studied separately by Raman spectroscopy at 460°C and back to room temperature (Figure 56). The spectra at 460°C and back to room temperature measured on the altered area (zone 1) are those described above (Figure 52). The spectra measured on the less abundant well preserved areas were similar when back to room temperature but showed differences at 460°C (Figure 56). In particular, the characteristic features of In-Te vibrations were far less developed.

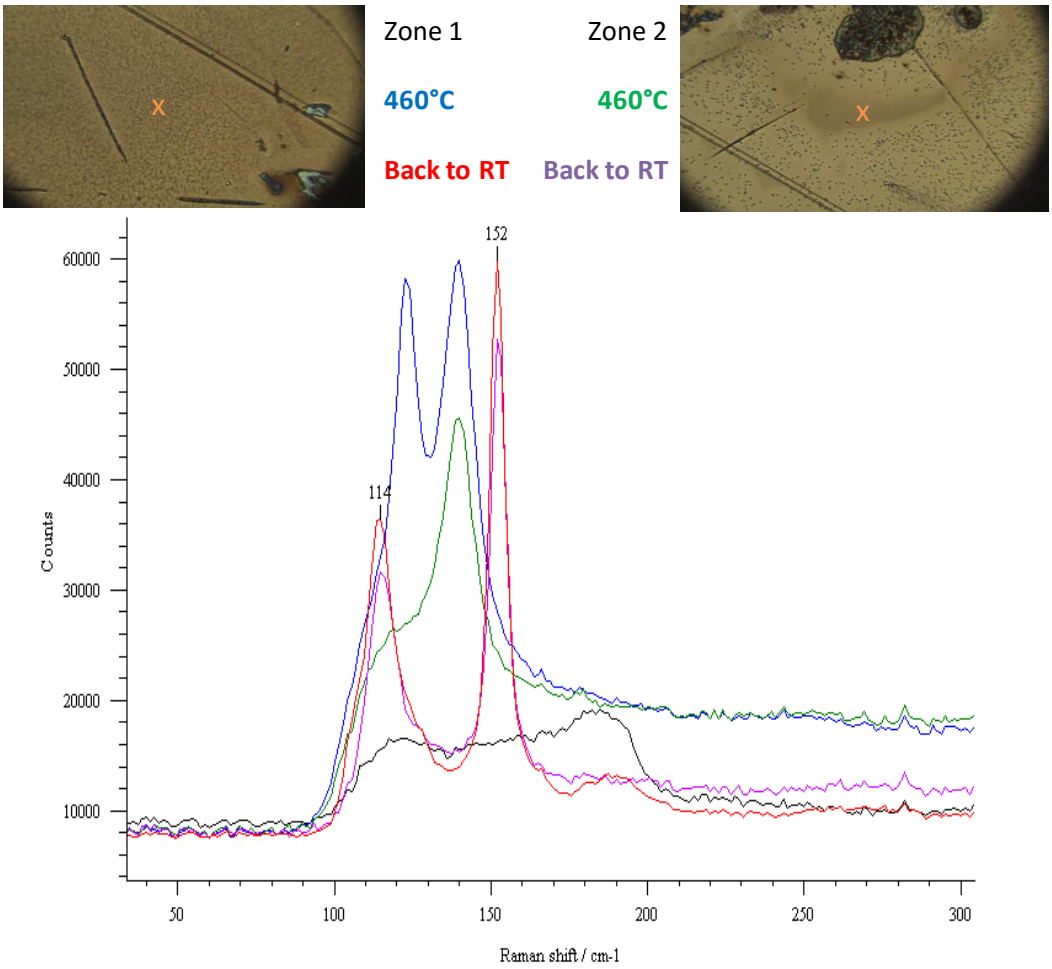

Figure 56: Study of two areas of $In_3Sb_{2.5}Te_{1.2}$ (sample 439 in Table 4) by Raman spectroscopy at room temperature, 460°C and back to room temperature

In order to investigate the origin of this difference, the two types of zones were next studied by Scanning Electron Microscopy (SEM) and X-Ray microanalysis (Energy Dispersive Spectrometer – EDS and Wavelength-dispersive X-ray spectroscopy - WDS).

Under the SEM, the so-called “altered” area where typified by micron-sized crystals cf e.g., Figure 57, whereas well preserved zones included crystals and/or nuclei of a considerably smaller size.

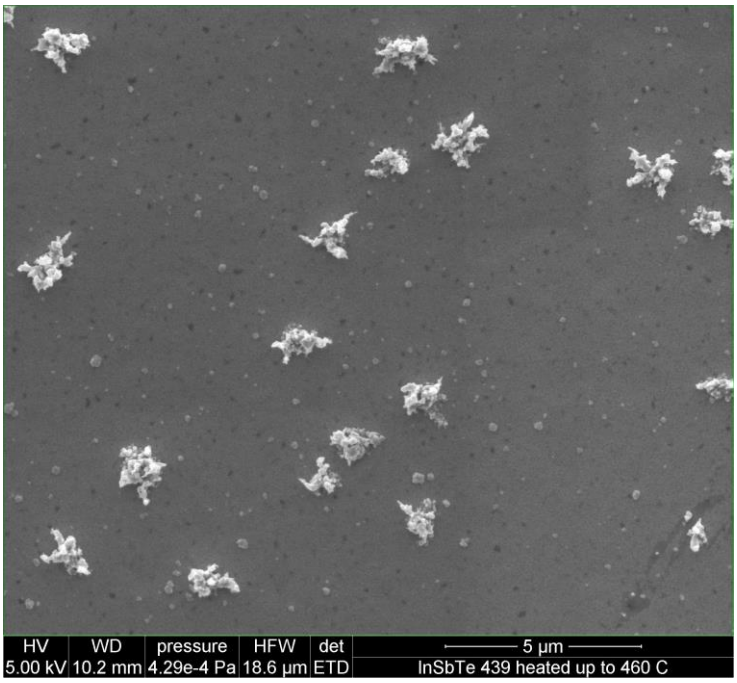

Figure 57: $In_3Sb_{2.5}Te_{1.2}$ (sample 439) heated to 460°C and return to the room temperature (RT) - Heterogeneous surface

	EDS				WDS			
	In (W%)	Sb (W%)	Te (W%)	composition	In (W%)	Sb (W%)	Te (W%)	composition
Back-z1	38,76	42,42	18,82	$InSb_{1,1}Te_{0,5}$	38,77	42,71	18,52	**$InSb_{1,1}Te_{0,5}$**
GG1-z1	45,07	10,37	44,56	$In_3Sb_{0,7}Te_3$	47,49	15,38	37,13	**$In_3SbTe_{2,3}$**
GG2-z1	58,01	12,24	29,75	$In_3Sb_{0,6}Te_{1,5}$	56,68	17,12	26,20	**$In_3Sb_{0,9}Te_{1,4}$**
Back-z2	37,22	44,20	18,58	$InSb_{1,2}Te_{0,5}$	37,92	43,49	18,58	**$InSb_{1,2}Te_{0,5}$**

Table 8: EDS and WDS results. The percentage of In, Sb and Te are measured (from data reported in Figure 58) on the crystal (GG) and the background surface (back). Two measurements have been done for reliability purpose.

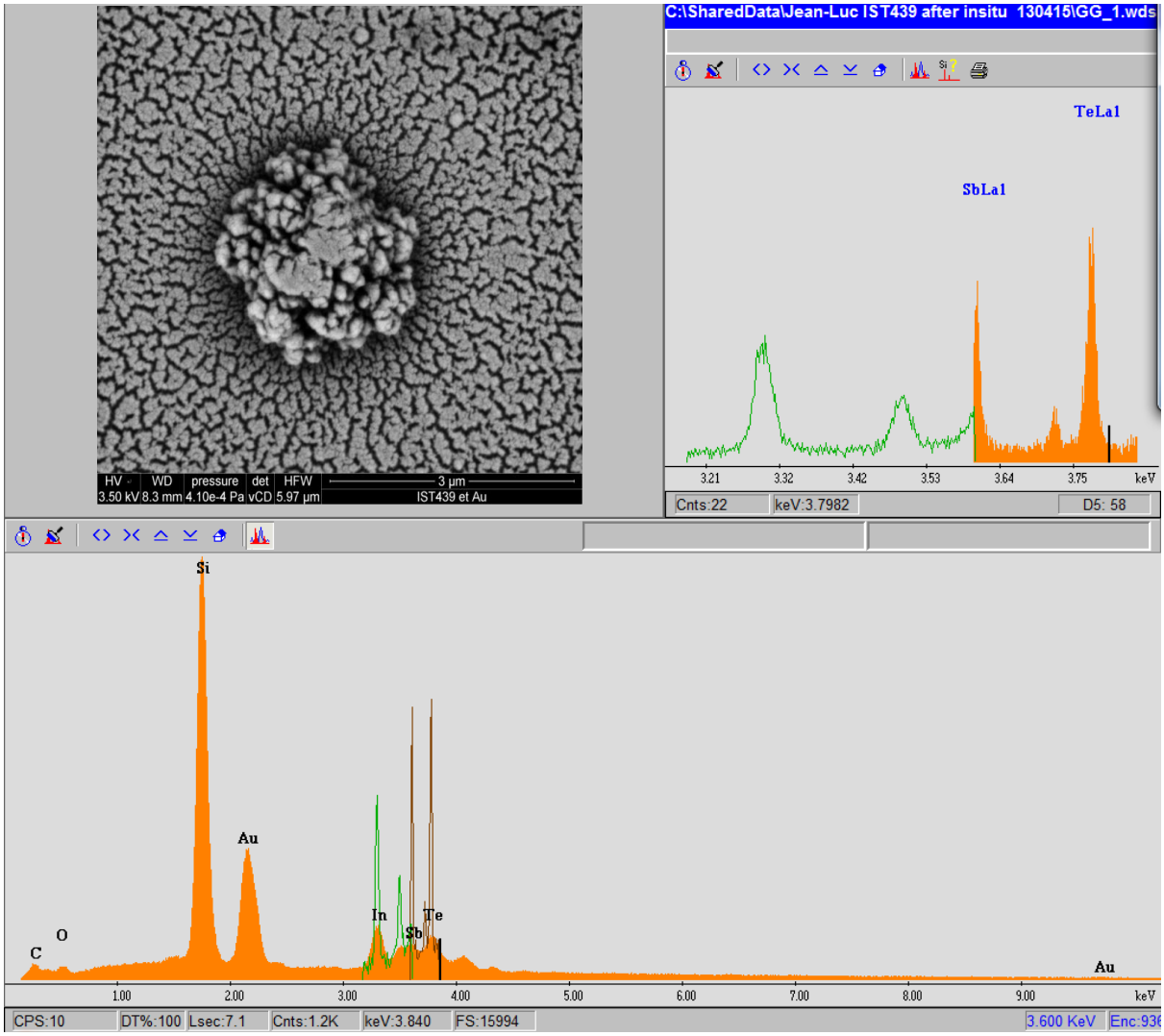

Figure 58: EDS spectrum focused on one crystal of the $In_3Sb_{2.5}Te_{1.2}$ (sample 439) heated to 460°C and return to the room temperature (RT)

The EDS and WDS spectra taken on crystals (GG) and on the smooth surface (background) differed essentially in the relative abundance of Sb that was much smaller in the crystal. The WDS and EDS measurements are reported in Figure 58. The extracted values for In, Sb and Te percentages are reported in Table 8. Those results confirm that crystals are $In_3Sb_1Te_2$ and that the background composition is consistent with the $In_1Sb_{0.8}Te_{0.2}$ that have been observed already using the XRD (Figure 36).

4.5.3 MPTR Measurements

According to the investigated frequency range [1000-30000] Hz, the heat penetration depth at the higher frequency ($\sqrt{a/\pi f}$, a being the thermal diffusivity) is much larger than the

thickness of the stack constituted from all the thin films. Therefore, each layer behaves as a thermal resistance whereas the Si substrate can be considered as a semi-infinite medium. Therefore, we fall in the same configuration than that we met with the 3ω configuration. The only difference stands on the shape of the thermally excited area: a disk with a uniform heat flux density (consistent with the use of a fiber laser diode) for the MPTR instead of a strip in the case of the 3ω. Neglecting heat diffusion within the Pt capping layer, this leads to the representation of the heat transfer in the sample as described in Figure 59.

Therefore, the measured surface temperature is expressed according to the heat flux density as:

$$T_s(w) = Z(w) j\ (w) \tag{4.6}$$

With:

$$Z(w) = R_T + Z_{Si}(w) \tag{4.7}$$

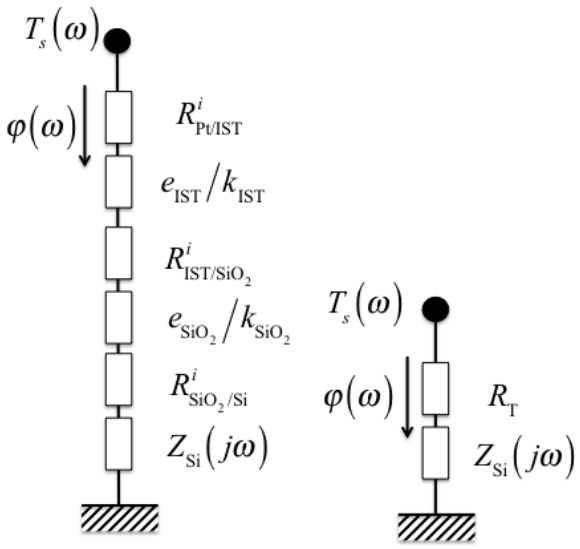

Figure 59: model of heat transfer in the sample within the MPTR experimental configuration.

As demonstrated in chapter 3 (relation (1.57)), the thermal impedance for the Si substrate is:

$$Z_{\mathrm{Si}}(j\omega)=\frac{r_0^2}{r_d\,k_{\mathrm{Si}}}\sum_{n=0}^{N}\frac{J_1(a_n r_d)}{a_n^{\,2}\tanh\left(e_{\mathrm{Si}}\sqrt{a_n^{\,2}+\frac{j\omega}{a_{\mathrm{Si}}}}\right)\sqrt{a_n^{\,2}+\frac{j\omega}{a_{\mathrm{Si}}}}\,R^2\,J_0(a_n R)^2}\,e^{-\left(\frac{a_n r_0}{2}\right)^2} \tag{4.8}$$

Where R is the sample radius, r_0 is the laser spot radius at the surface and r_D is the IR detector radius, e_{Si}, a_{Si} and k_{Si} are the thickness, thermal diffusivity and conductivity of the Si substrate respectively and:

$$a_n R \approx \pi\left(n+\frac{1}{4}\right)-\frac{3}{8\pi\left(n+\frac{1}{4}\right)},\ a_0=0 \tag{4.9}$$

However, the laser spot radius at the surface being equivalent to the sample radius R, the previous relation simplifies considering 1D heat diffusion as (see chapter 4, relation (1.58)):

$$Z_{\mathrm{Si}}(j\omega)=\frac{1}{k_{\mathrm{Si}}\tanh\left(e_{\mathrm{Si}}\sqrt{\frac{j\omega}{a}}\right)\sqrt{\frac{j\omega}{a_{\mathrm{Si}}}}} \tag{4.10}$$

The IST and SiO_2 layers behave as pure thermal resistances as: $R_{\mathrm{IST}}=e_{\mathrm{IST}}/k_{\mathrm{IST}}$ and $R_{\mathrm{SiO_2}}=e_{\mathrm{SiO_2}}/k_{\mathrm{SiO_2}}$ respectively. The thermal conductivity of amorphous SiO_2 is $k_{\mathrm{SiO_2}}=1.45\,\mathrm{W.m^{-1}.K^{-1}}$ and we consider that it does not significantly vary in the 100°C to 550°C temperature range. On the other hand, the Pt layer thermal resistance ($e_{\mathrm{Pt}}/k_{\mathrm{Pt}}$) can be neglected with respect to the two previous ones as Pt is assumed to be thermally thin. The total thermal resistance is therefore:

$$R_T=R^i_{\mathrm{Pt/IST}}+\underbrace{\frac{e_{\mathrm{IST}}}{k_{\mathrm{IST}}}}_{R_{\mathrm{IST}}}+R^i_{\mathrm{IST/SiO_2}}+\frac{e_{\mathrm{SiO_2}}}{k_{\mathrm{SiO_2}}}+R^i_{\mathrm{SiO_2/Si}} \tag{4.11}$$

Another form of this relation is:

$$R_T=R^i+\frac{e_{\mathrm{SiO_2}}}{k_{\mathrm{SiO_2}}}+R_{\mathrm{IST}} \tag{4.12}$$

The total boundary resistance being:

$$R^i = R^i_{\mathrm{Pt/IST}} + R^i_{\mathrm{IST/SiO_2}} + R^i_{\mathrm{SiO_2/Si}} \tag{4.13}$$

The temperature of the sample is controlled in a furnace (LINKAM 1200) working under inert atmosphere (Ar or N_2). The sample was heated at a rate of 25 °C/min and annealed for 2 min at the required temperature before starting the measurement (duration of the experiment is about 4 hours for one sample). Measurements were performed from room temperature up to 550°C. The thermal resistance for the two stoichiometries at each investigated temperature was identified from the phase lag defined as:

$$\mathrm{Phase}\left[Z(\omega)\right] = \mathrm{Arg}\left[Z(\omega)\right] = \mathrm{Arctan}\frac{\mathrm{Im}\left[Z(\omega)\right]}{\mathrm{Re}\left[Z(\omega)\right]} \tag{4.14}$$

R_T is the unknown parameter that needs to be identified. The Levenberg-Marquardt algorithm was used that minimized the quadratic gap J between the theoretical phase lag and the measured one as:

$$J = \left\| \mathrm{Phase}\left[Z(\omega)\right] - \mathrm{Phase}_{\mathrm{exp}} \right\|_2 \tag{4.15}$$

The standard deviation on R_T can be estimated from non linear least square formalism as:

$$\sigma^2(R_T) = \left(X^T X\right)^{-1} \sigma^2_{phase},\ \sigma^2_{phase} \approx \frac{J_f}{N_w} \tag{4.16}$$

In this relation J_f denotes the value of the quadratic gap at the end of the iteration process and N_w is the number of frequency points.

We defined also the following parameter of interest:

$$R'_T = R^i + R_{\mathrm{IST}} \tag{4.17}$$

We repeated the experiments three times and we did not obtain a very good reproduction of the data each time. As demonstrated after, we think it comes from the fact that the samples are deteriorated at high temperature. In addition we observed that this deterioration is more pronounced if we waited a long time between the IST deposition and the thermal characterization. Therefore, instead of using an average of all the data obtained during the experiments, we only retain those that seem to be the most relevant with regards to the surface aspect during the annealing. The experimental phase and the simulated one using the

identified value of R_T' are represented in Figure 60 to Figure 67 for all the samples. These comparisons are very relevant in terms of the identification quality. The first observation is that we are able to measure the thermal resistance of the thin layer even in the case of very low thickness and with a small variation of the thickness between the investigated samples. Indeed, the previous work we have done on GST thin films dealt with thickness varying from 120 to 840 nm, that seems to be very large in comparison with the IST layers we have worked with in this study. For almost all the samples, the fits between experimental and simulated phase are very good.

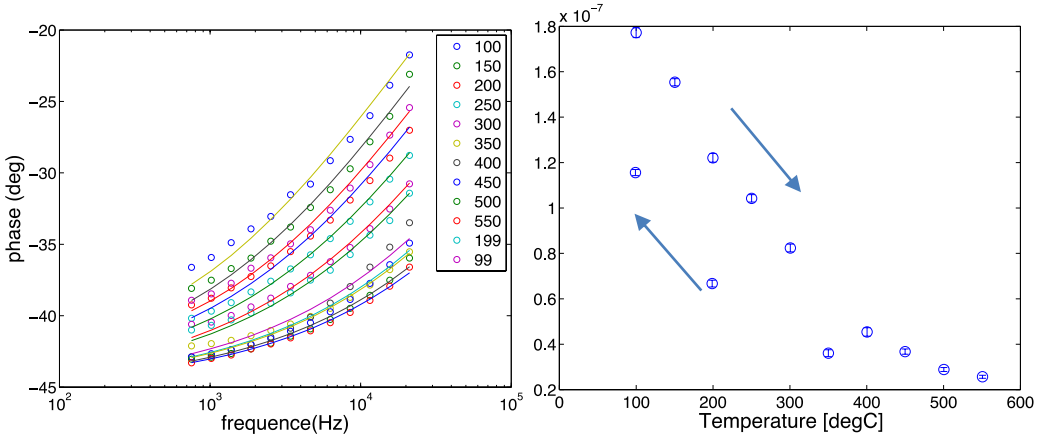

Figure 60: sample MOIST436 (30nm) left: phase calculated (line) with optimal value of R_t and measured (hollow disk); right: identified R_T' in K.m^2/W.

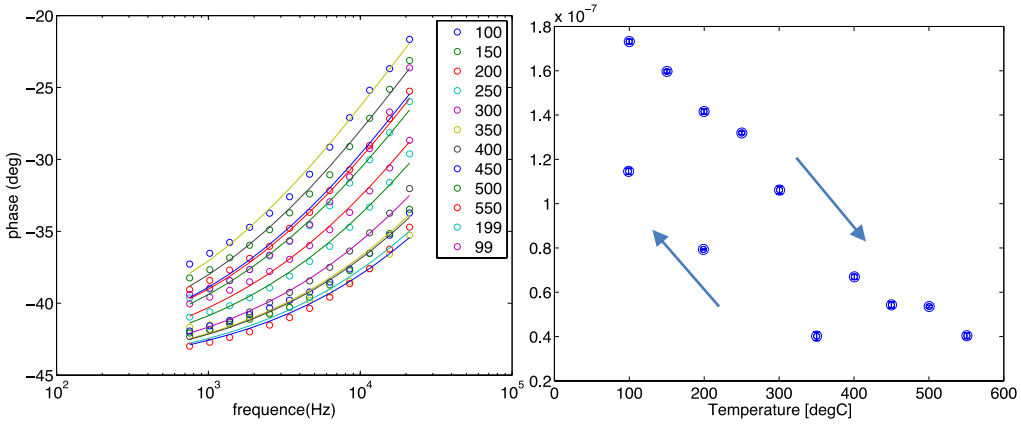

Figure 61: sample MOIST437 (50nm) left: phase calculated (line) with optimal value of R_t and measured (hollow disk); right: identified R_T' in K.m^2/W.

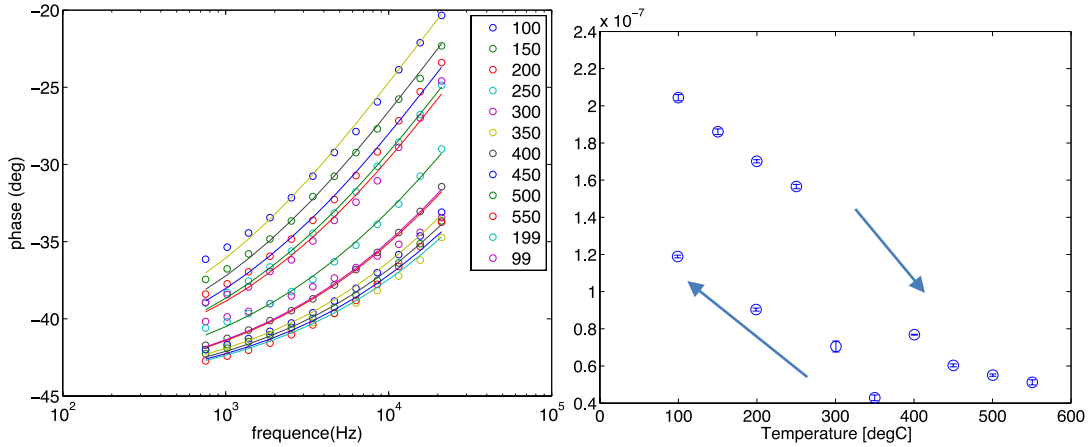

Figure 62: sample MOIST435 (65nm) left: phase calculated (line) with optimal value of R_t and measured (hollow disk); right: identified R_T' in K.m^2/W.

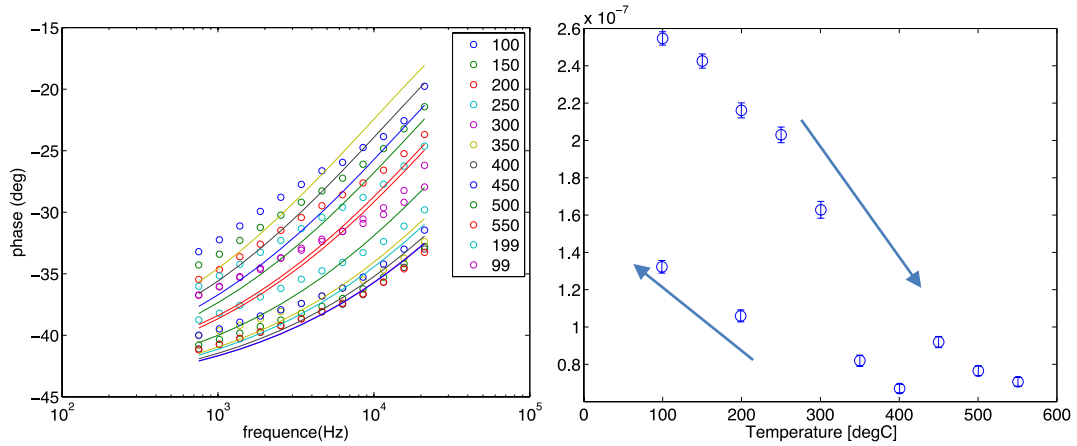

Figure 63: sample MOIST434 (90nm) left: phase calculated (line) with optimal value of R_t and measured (hollow disk); right: identified R_T' in K.m^2/W.

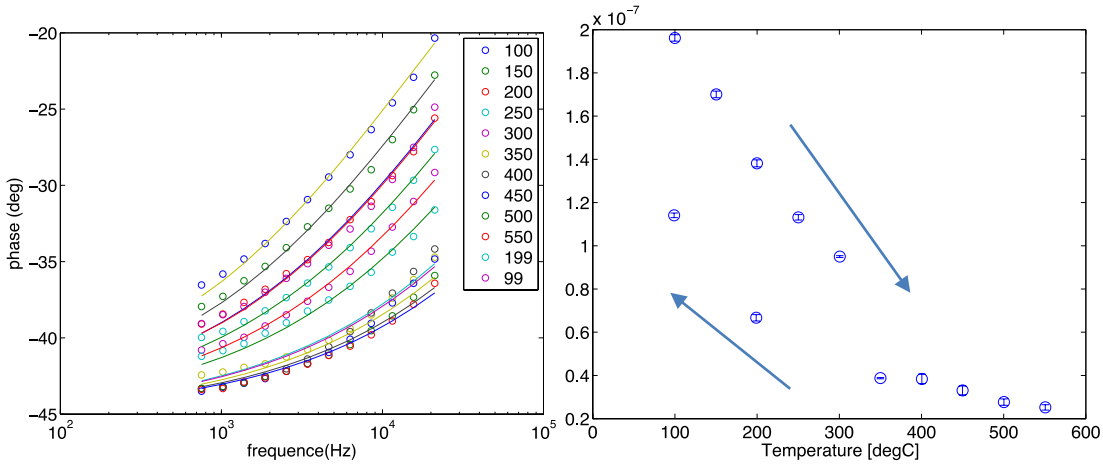

Figure 64: sample MOIST441 (30nm) left: phase calculated (line) with optimal value of R_t and measured (hollow disk); right: identified R_T' in K.m^2/W.

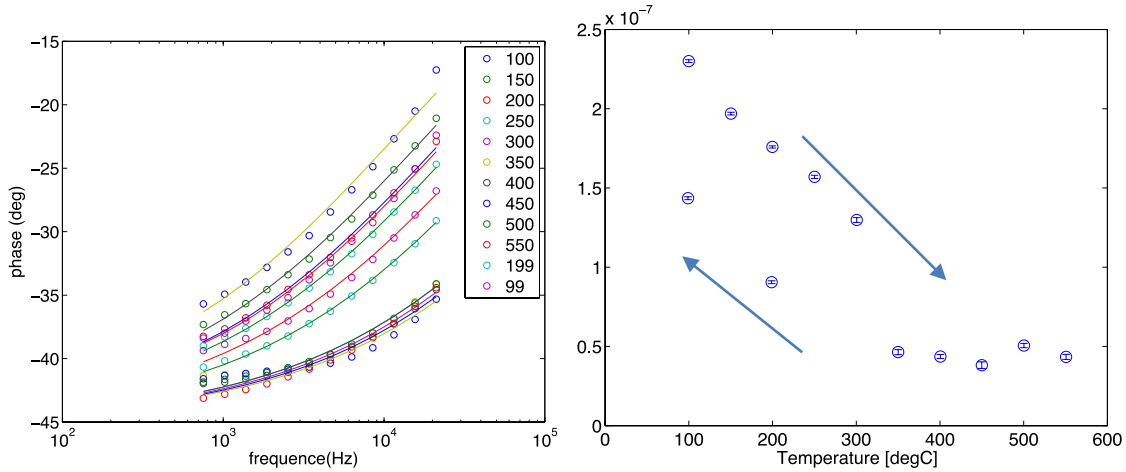

Figure 65: sample MOIST438 (50nm) left: phase calculated (line) with optimal value of R_t and measured (hollow disk); right: identified R_T' in K.m^2/W.

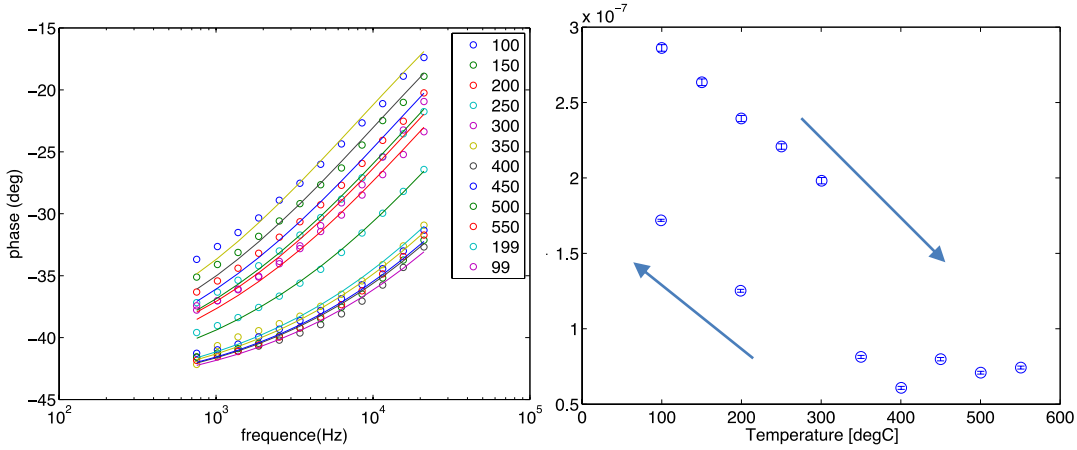

Figure 66: sample MOIST440 (70nm) left: phase calculated (line) with optimal value of R_t and measured (hollow disk); right: identified R_T' in K.m^2/W.

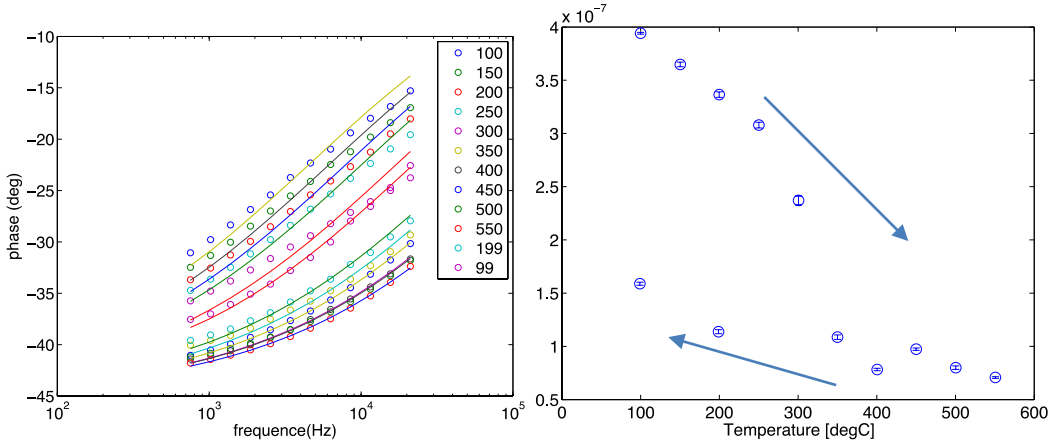

Figure 67: sample MOIST439 (105nm) left: phase calculated (line) with optimal value of R_t and measured (hollow disk); right: identified R_T' in K.m^2/W.

Only the 90 nm thick sample (MOIST434) leads to some significant bias at low temperature and high frequency. This quality is also evidenced by the error bars on R_T' that are very low.

All the identified values for R_T' for both compositions of the IST according to the IST thickness have been reported in Figure 68 and Figure 69. We observed a significant change in the variation of R_T' starting from 300°C. Let us remind that we observed that the Raman peaks started to modify also from this temperature that is related to Te-Te bonds and In-Te bonds arrangement. It is clear that this structural change involves also a significant variation of the IST thermal conductivity. This result was not expected since such a variation of the electrical resistivity was not measured. From room temperature up to 550°C, the thermal resistance decreases continuously. Going back to room temperature from 550°C, the thermal resistance starts to increase again. This result is consistent with previous observations on the electrical resistivity as well as those obtained by Raman. Indeed, we underlined that the IST structure shows a low electrical and thermal resistivity metastable state which disappears when going back to room temperature. This metastable state was monitored by in-situ XRD as the disappearance of the as deposited $InSb_{0.85}Te_{0.15}$ phase [16].

The linear regression performed for each temperature gives the In-Sb-Te thermal conductivity k_{IST} as well as to the total thermal boundary resistance R^i.

4.5.4 Discussion on thermal conductivity

Thermal conductivity values for the two In-Sb-Te compositions are reported in Figure 72. The values obtained for the as-deposited IST using the 3ω method are also reported in the figure. As expected, the two compositions present very close values for the thermal conductivity in the [RT-550°C] temperature range. In addition, they are also close to the values found for the $Ge_2Sb_2Te_5$ alloy and reported on the plot. During thermal annealing, the thermal conductivity monotonically increased owing to the on-going crystallization of the materials. As revealed by the plot, a more pronounced change occurred about 300°C for both Te contents. This observation is very consistent with the crystallization that is expected to occur at about 280°C. With respect to the error bars, the data fluctuated rather significantly between 400°C and 450°C. Going back to room temperature (RT) after 550°C led to stable values for the thermal conductivity for the high Te IST sample, whereas it seems to be higher for the low Te IST sample. This result comes to make measurement on the low Te IST questionable when going back to RT. In fact, it is not very surprising since we observed previously, in Figure 46, that the low Te sample was more affected by the thermal budget.

The evolution of the thermal conductivity for the high Te IST when going back to RT shows that the crystalline phase developing at high temperature is not in a stable configuration. This observation is consistent with electrical resistivity and Raman measurements that have been presented previously. Indeed, for the high-Te IST the electrical resistivity increased when going back from 550°C to RT (see Figure 52) and thermal conductivity decreased in the same temperature range (see Figure 72. In addition, the Raman measurements demonstrated that the crystalline phase was not stable going back to RT.

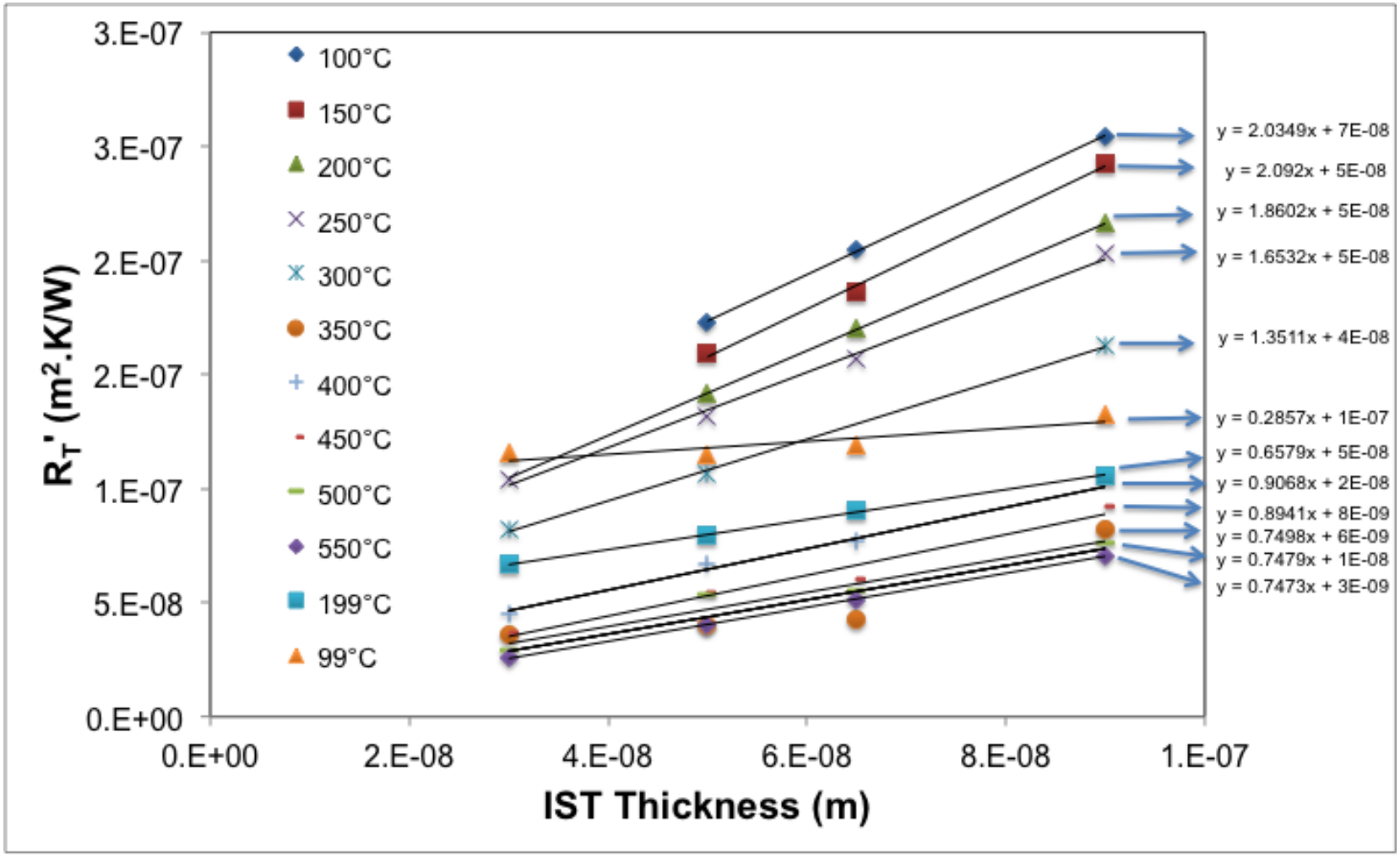

Figure 68: identified thermal resistance of low-Te sample.

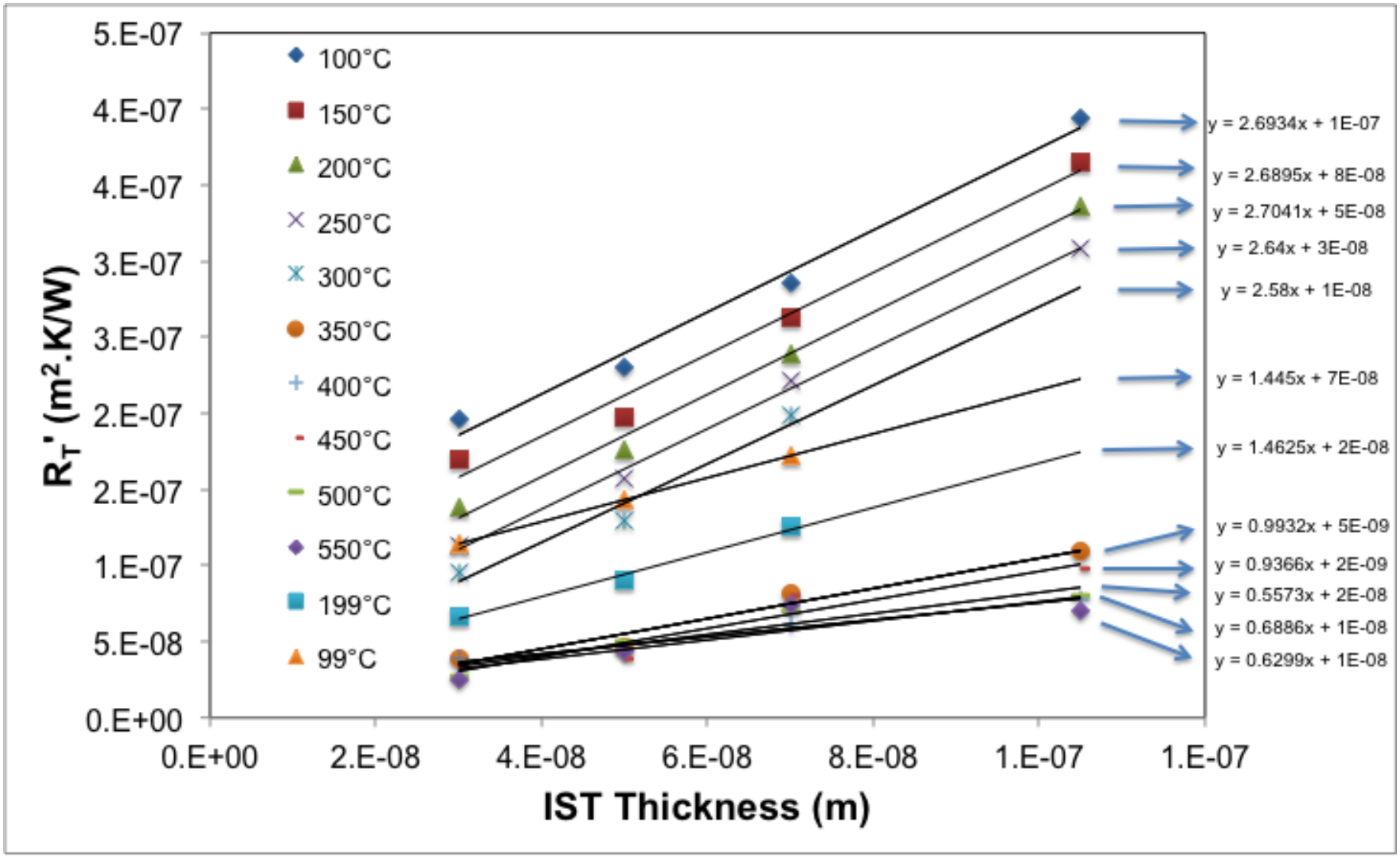

Figure 69 : Thermal resistance of high-Te sample.

The comparison between 3ω and MPTR measurements, at RT and annealed at 480°C, shows that the agreement is rather satisfactory for the IST with high Te content. A significant gap occurs for the IST with low Te content that cannot be explained to now since it does not come for an experimental mistake being that experiments have been repeated at least 3 times using both techniques.

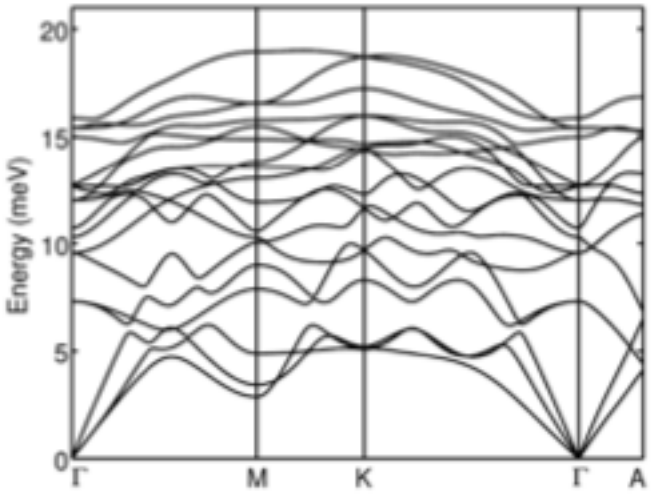

Figure 70: IST(312) dispersion curves $\omega(k)$ calculated using the DFT (calculations preformed by Marco Bernasconi at the UMB).

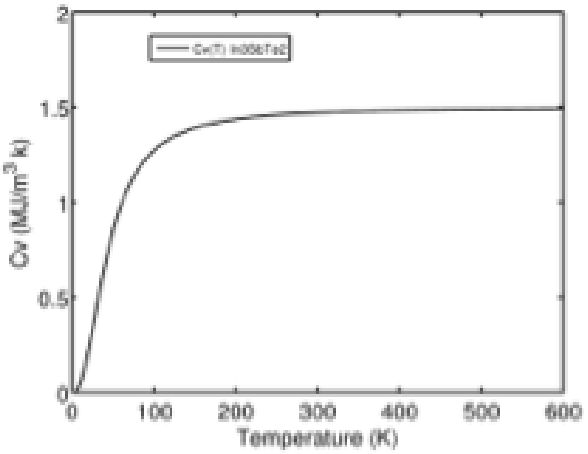

Figure 71: theoretical IST(312) specific heat (calculations preformed by Marco Bernasconi at the UMB).

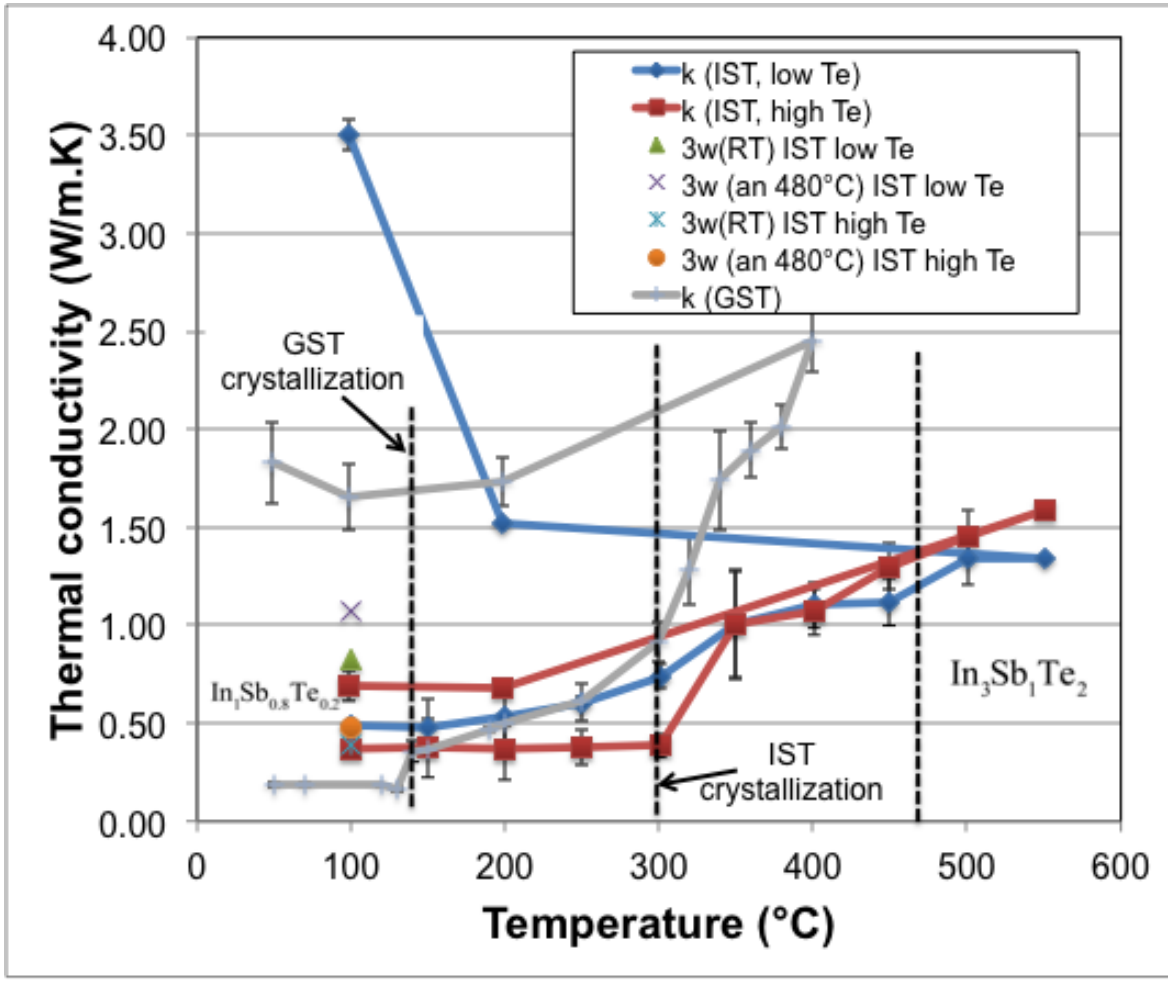

Figure 72: In-Sb-Te thermal conductivity k_{IST} for the two Te contents, comparison with GST(225). The data obtained on as-deposited IST using the 3ω method for both compositions are also reported.

The dispersion curves $\omega(k)$ for the IST(413) have been calculated by Marco Bernasconi at University Milano Biccoca (UMB) using the density functional theory (DFT) method. The results have been reported in Figure 70. Using these data it is thus possible to calculate the specific heat per unit volume for the IST as:

$$C_v = \sum_s \frac{\hbar^2}{2\pi^2 k_B T^2 v_{g,s}} \int_0^{\omega_{s,\max}} \frac{e^{\hbar\omega_s/k_B T}}{\left(e^{\hbar\omega_s/k_B T} - 1\right)^2} \omega_s^2 k\left(\omega_s\right)^2 \mathrm{d}\omega_s \tag{4.18}$$

In this relations $v_{g,s}$ is the group velocity for polarization s (one longitudinal and two transverse); $\hbar = h/2\pi$ is the modified Planck constant, k_B is the Boltzmann constant, ω is the frequency. We obtained the value reported in Figure 71. Assuming the Debye model and using $x = \hbar\omega/k_B T$ and $\Theta_{D,s} = \left(6\pi^2 n\right)^{1/3} v_{g,s}\hbar/k_B$, relation (4.18) comes to:

$$C_v = \sum_s \frac{3k_B T^3}{\Theta_{D,s}^3} \int_0^{x_{s,\max}} \frac{x^4 e^x}{\left(e^x - 1\right)^2} \mathrm{d}x \tag{4.19}$$

The value becomes constant starting to 200 K (Debye temperature being close to 190 K) and equal to 1.5 MJ/(m^3.K) that is rather close to the measured one (1.325 MJ/m^3.K in Table 3). Using this value and that of the measured thermal conductivity we can extract the mean free path (mfp) l value as:

$$l = \frac{3k}{C_v c} = 0.6\,\mathrm{nm} \tag{4.20}$$

where $c = \left(v_L + 2v_T\right)/3$ is the sound velocity in IST(312). The mfp is thus very low which means that thermal conductivity can be defined for films with a thickness that is at least more or equal to 10 l. This is somehow a validation our measurements conducted on MOIST 436 and 441 samples where thickness was 30 nm.

The observed flattening of $k(T)$ above the crystallization temperature (T_c=280°C) might be indicative of the approach of a plateau which is a characteristic feature of glass-like thermal conductivities [43][45]. This phenomenon of plateauing is classically representative of phonon localization due to strong phonon scattering from heterogeneities [45].

A lower limit for the thermal conductivity k can be obtained by Cahill's model of $k_{\min}$ [43], which serves as a reasonable starting point to explain our findings. Within the original Debye model of heat transport in crystals the phonon mean free path is set to the smallest reasonable value of half the phonon wavelength, defining:

$$k_{\min} = \left(\frac{\pi}{6}\right)^{1/3} k_B n^{3/2} \sum_s v_{g,s} \left(\frac{T}{\Theta_{D,s}}\right)^2 \int_0^{\frac{\Theta_{D,s}}{T}} \frac{x^3 e^x}{\left(e^x - 1\right)^2} \mathrm{d}x \tag{4.21}$$

with n the atomic number density (3.21×10^{28} m^{-3}) [46] and the sum is taken over two transverse and one longitudinal phonon branch, each with individual sound velocities $v_{g,s}$ and cut-off temperatures $\Theta_{D,s} = \left(6\pi^2 n\right)^{1/3} v_{g,s} \hbar / k_B$. The transversal and longitudinal sound velocities v_L and v_T are reported in Table 3. The minimum thermal conductivity is found to be 0.378 W.m^{-1}.K^{-1} at 300 K and it is also shown in Figure 73 as a dashed line. The consistent agreement between the model and the data at room temperature is clear evidence for pronounced phonon scattering. However, the plateau from RT up to T_c demonstrates that scattering mechanisms are independent of temperature.

In order to better fit the experimental data after the crystallization point we have thus to include the effects of grain boundary, point defect, Umklapp and resonant phonon scattering in a modified Debye model [37, 38] through the phonon relaxation rate $1/\tau$ as:

$$t\left(T,\omega\right)^{-1} = \frac{c}{L} + A\omega^4 + B\omega^2 T e^{-\Theta_D/3T} + \sum_s \frac{C_s \omega^2}{\left(\omega_s^2 - \omega^2\right)^2} \tag{4.22}$$

Here $c = \left(v_L + 2v_T\right)/3$ denotes the sound velocity, L the grain size while A, B and C_s refer to the coefficients of point defect, Umklapp and resonant phonon scattering, respectively. The lattice thermal conductivity is then expressed as follows:

$$k_l\left(T\right) = \frac{k_B}{2\pi^2 c}\left(\frac{k_B T}{\hbar}\right)^3 \int_0^{\frac{\Theta_{D,s}}{T}} \frac{x^4 e^x}{\tau\left(T,\omega\right)^{-1}\left(e^x - 1\right)^2} \mathrm{d}x \tag{4.23}$$

This approach was implemented in [43] for the GST alloy. However, the parameters were fitted considering the thermal conductivity measurement on [77-300] K for annealed sample at temperature higher than T_c. In our configuration we assumed constant parameters over a temperature range where the variation of the thermal conductivity is linear. In such a case the

grain boundary and resonant phonon scattering are not expected to participate in the phonon relaxation rate that can be simplified by only retaining the Umklapp and point defect contribution as:

$$t\left(T,w\right)^{-1} = Aw^4 + Bw^2 T e^{-Q_D/3T} \tag{4.24}$$

With $x = \hbar\omega / k_B T$, one has $\tau\left(T,x\right)^{-1} = A\left(k_B T/\hbar\right)^4 x^4 + B\left(k_B T/\hbar\right)^2 x^2 T e^{-\Theta_D/3T}$. The identified parameters A and B that lead to fit the theoretical $k_l(T)$ with experimental data on the RT-550°C temperature range are found by minimizing the quadratic gap between the measured conductivity and that calculated from relation (4.23). The parameter B is found almost constant to 1 x 10^{-22} (sK^{-1}). The parameter A is listed in Table 9 for both Te content in IST alloy. This result clearly shows that annealing leads to a significant reduction of point defect scattering (parameter A) while the Umklapp processes remain essentially constant. This demonstrates that the observed increase of thermal conductivity upon annealing is due to a decrease in point defect scattering. After [43], the typical sources for point defect scattering are local fluctuations in mass density or bonding.

To account for amount of vacancies according to the IST stoichiometry, one may rewrite the structure formula as $(InTe)_{1-x}$ $(\square Sb_2Te_3)_x$, where $\square$ represents the vacancy. From this it is evident that the fraction of stoichiometric vacancies changes with x as $x/(1+2x)$ [47]. These stoichiometric vacancies are not pinned to fixed lattice sites but randomly distributed.

	Temperature range (°C)						
	[RT-150]	[150-280]	[280-350]	[350-400]	[400-450]	[450-500]	[500-550]
A x 10^{-42} (s^{-3})	15	15	4	2	0.95	0.9	0.87
	9	6	2	0.94	0.9	0.88	0.88

Table 9: identified parameter *A* in the relaxation time of phonon in the lattice thermal conductivity model based on the Debye assumption. First row for low Te and second row for High Te content.

The representation of the crystal arrangement in IST for the high Te content is represented in Figure 73. It is connected with the Raman observations made previously. As showed in the

figure, the differences between each state are clearly due to the localization of vacancies in the structure.

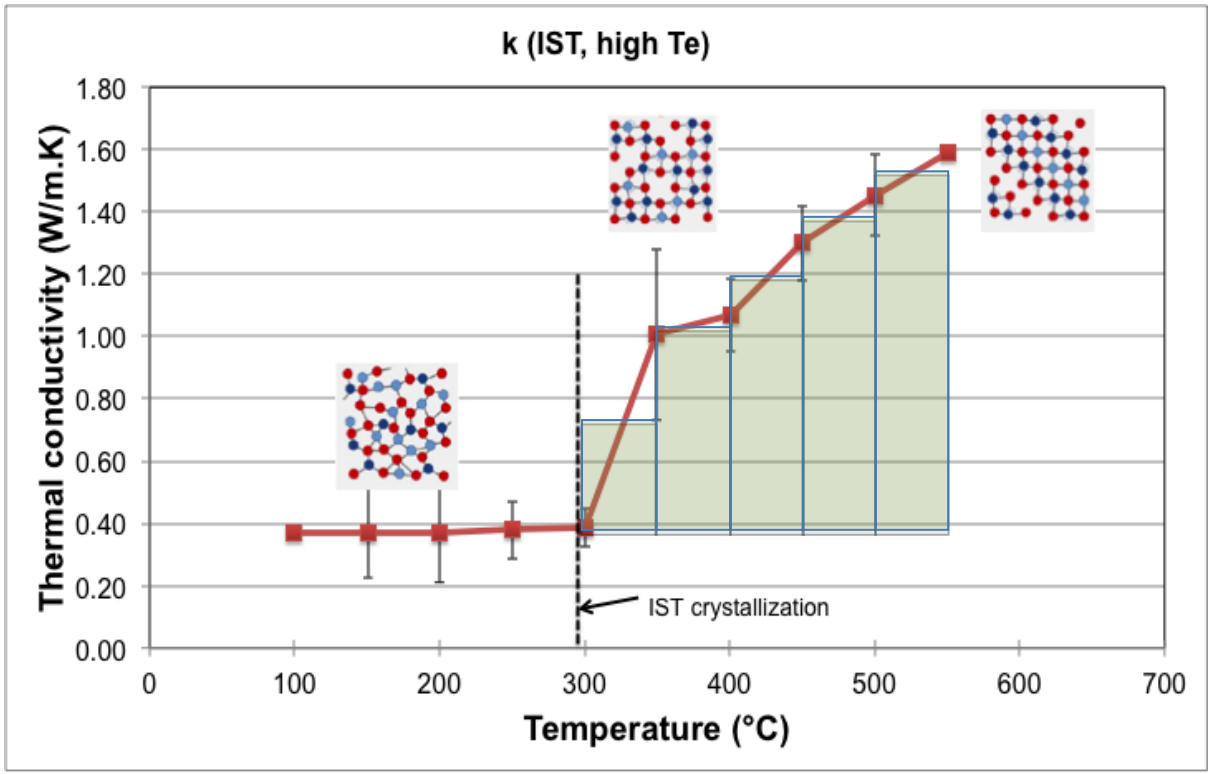

Figure 73: high Te thermal conductivity vs Temperature explained through the crystalline organization.

In Figure 75 we plotted the ratio $k/\sigma T$, between the thermal conductivity and the product σT of the electrical conductivity and the absolute temperature, according to the temperature. The electrical conductivity is deduced from measurement of the electrical resistivity using the Van der Paw technique, when the IST is capped with TiN. The measurements of the electrical resistivity are reported in Figure 74. This configuration is more appropriate with our configuration where IST is capped by Pt. On the same plot we reported the Lorentz constant L_0=2 .45x10^{-8} W.Ω.K^{-2}.

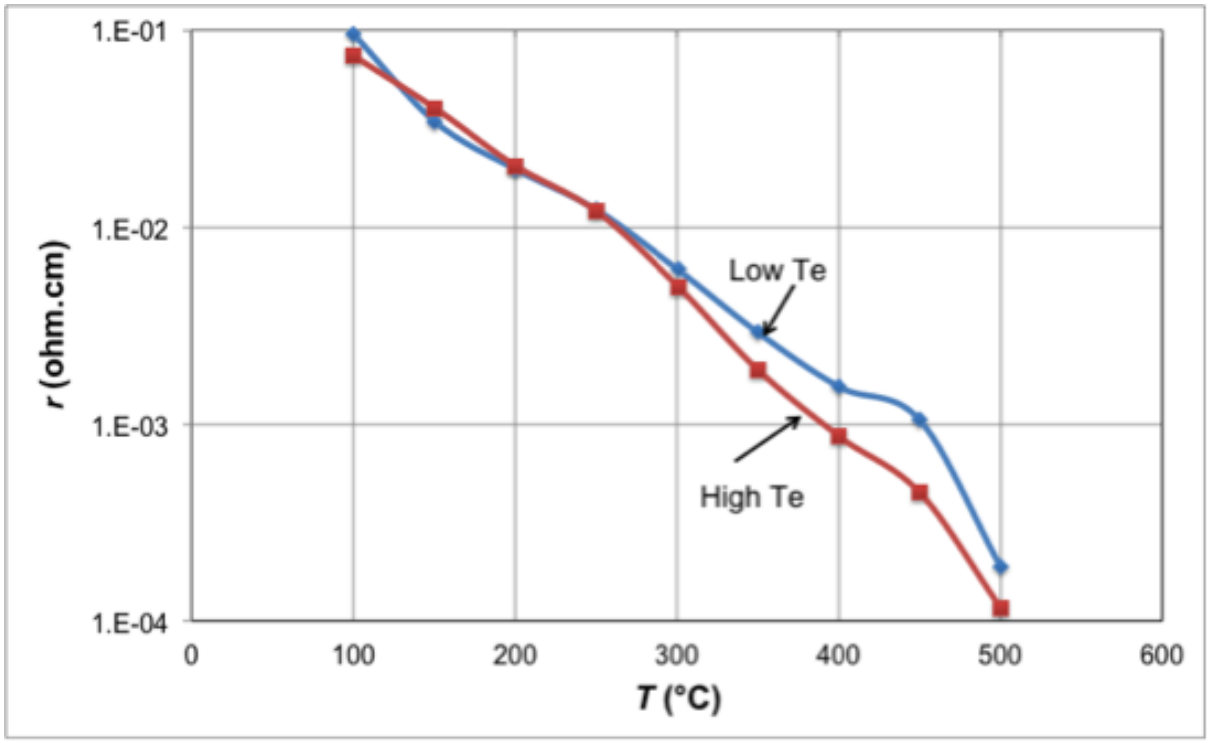

Figure 74: electrical resistivity of IST (low and high Te) using the Van der Paw method. The IST layer is capped with TiN.

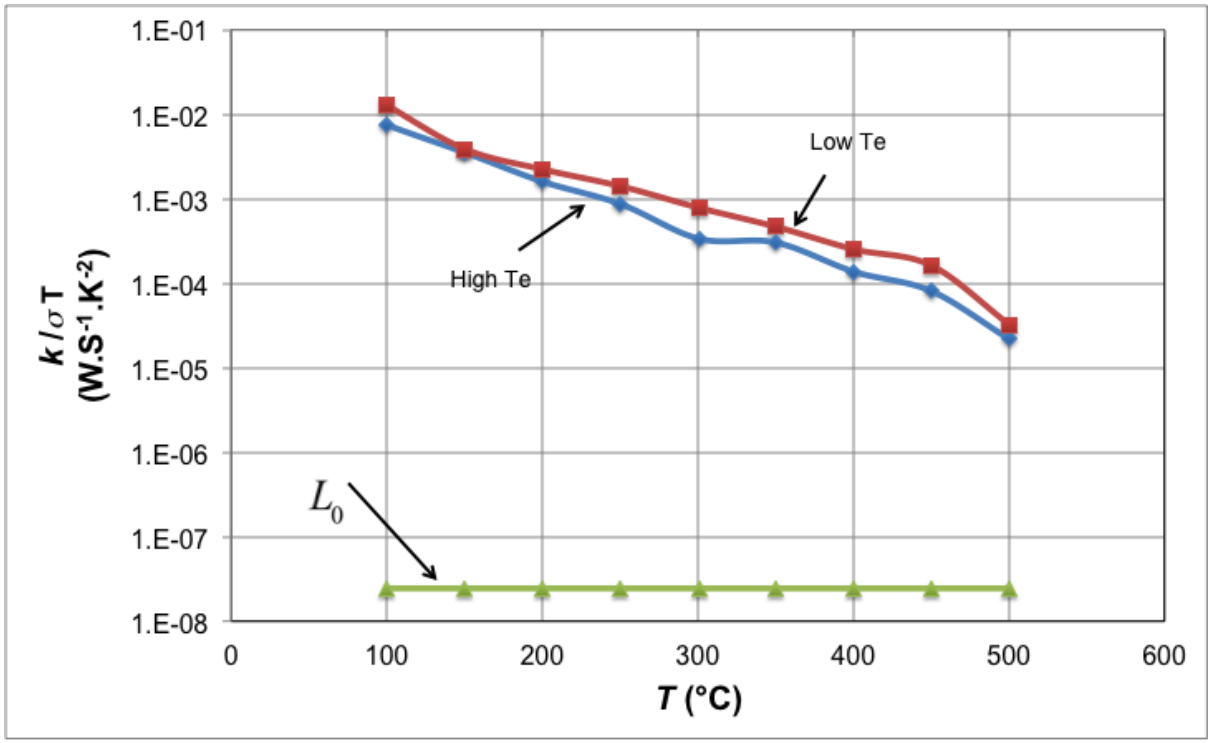

Figure 75: ration between the thermal conductivity (k) and electrical conductivity (σ) x temperature (T) vs temperature for both Te contents in the IST.

In this way the figure allows a distinction of the electronic and lattice heat transport for each temperature. Consistently with the Wiedemann Franz law (WFL), a proportional dependence between k and σT with a value close to the Lorentz number L_0=2.45x10^{-8} W.Ω.K^{-2} is expected when the change of k is exclusively controlled by the electronic contribution. As the WFL marks the upper limit of the electronic contribution, the excess in L^* over L_0 for the two alloys cannot be due to electronic effects only but also includes lattice effects. Hence, L^* provides a simple measure whether the enhancement of the transport parameters is dominated by lattice contributions ($L^* \gg L_0$). Clearly the electrons do not have a significant contribution in the thermal conductivity that is thus only related to the phonons.

4.5.5 Discussion on the TBR

The measured total boundary resistance is reported in Figure 76. As showed, the total thermal boundary resistance decreases from 10^{-7} down to 10^{-8} K.m^2/W when temperature increases from RT up to 580°C. Going back to RT, the TBR strongly increases to a value close to the initial value at RT that is about 10^{-7} K.m^2.W^{-1}. In the same figure, we reported the data obtained using the 3ω method on the as-deposited samples at RT and on those annealed at 580°C but measured at RT. Results are very consistent with those obtained by the MPTR.

The TBR can be estimated theoretically using the diffuse mismatch model (DMM) reliable at high temperature (when temperature becomes higher than the Debye temperature of the material) [51][52][54][55]. The DMM gives the expression of the thermal conductance at the interface as:

$$G_i = \frac{1}{4}\sum_s \int_0^{\omega_{\max,1}} v_{g,1,s} \frac{\mathrm{d}n\left(T=T_1\right)}{\mathrm{d}T} \hbar\omega D_1\left(\omega\right)\tau_{1\to 2}\left(\omega\right)\mathrm{d}\omega \qquad (4.25)$$

where:

$$n\left(T\right) = \frac{1}{e^{\frac{\hbar\omega}{k_B T}} - 1} \qquad (4.26)$$

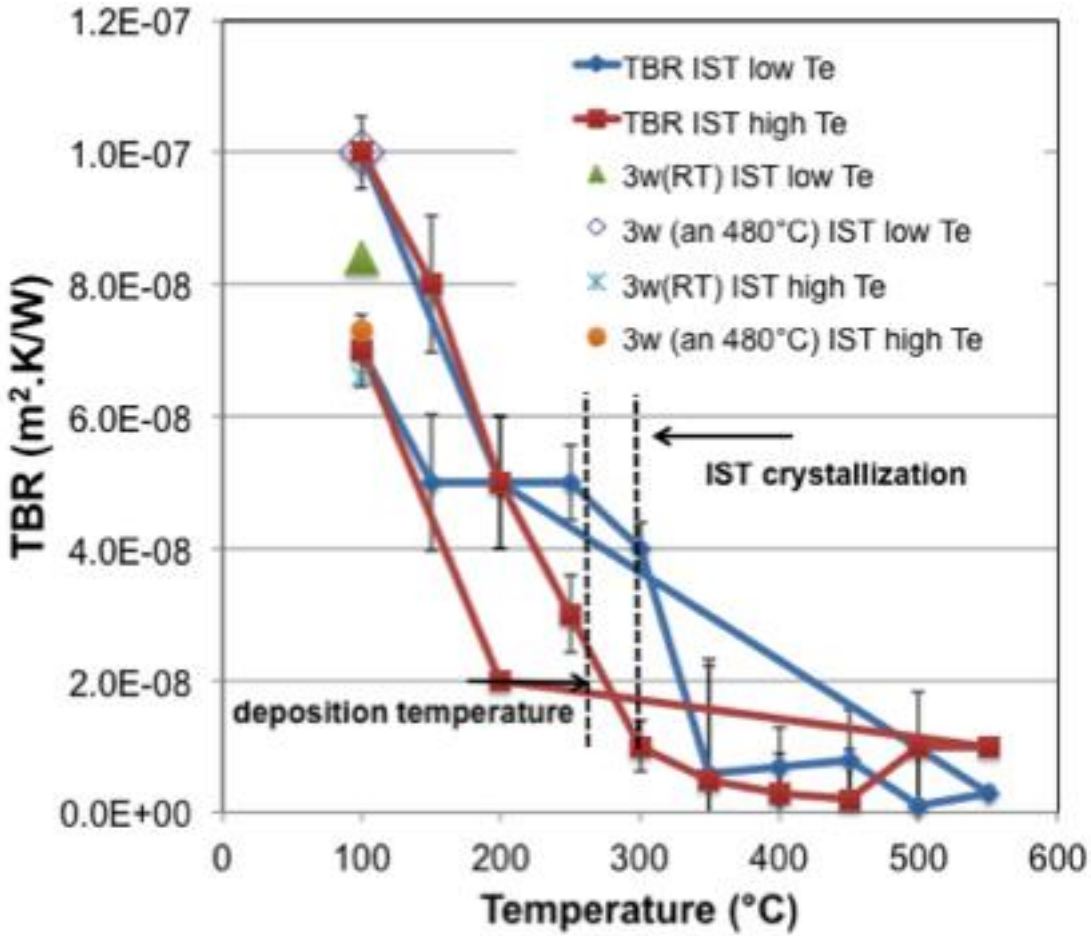

Figure 76: total thermal resistance R^i for the two Te contents as a function of temperature (blue filled square: comparison with theoretical value calculated using the DMM). The data obtained on as-deposited IST using the 3ω method for both compositions are also reported.

is the Bose-Einstein equilibrium distribution at temperature T, $D(\omega)$ is the density of states function and:

$$t_{1\to 2}(\omega) = \frac{\sum_s D_2(\omega) v_{g,2,s}}{\sum_s D_1(\omega) v_{g,1,s} + \sum_s D_2(\omega) v_{g,2,s}} \tag{4.27}$$

is the phonon transmission coefficient at the interface. In these relations $v_{g,i,s}$ is the group velocity for material i and polarization s; $\hbar = h/2\pi$ is the modified Planck constant, k_B is the Boltzmann constant, ω is the frequency.

The previous relation for G is based apon some assumptions; the most important one is that phonon scattering processes are elastic [51]. It means that elastic processes do not allow the phonon to change its frequency during the scattering.

The diffuse mismatch model (DMM) asymptotic formulation at high temperature gives the simplified expression of the thermal boundary conductance as:

$$G = 4 t_{1\to 2} c_1 r_1(T) C_{p,1}(T) \tag{4.28}$$

In this relation, material 1 is such that $\Theta_{D,1} < \Theta_{D,2}$, where Θ_D denotes the Debye temperature. In addition, c_1, r_1 and C_{p_1} are the sound velocity, the density and the specific heat of material 1, respectively. The phonon transmission coefficient t_{12} is calculated using the Debye approximation as:

$$t_{1\to 2} = \frac{c_2^{-2}}{c_1^{-2} + c_2^{-2}} \tag{4.29}$$

Relations (4.28) and (4.29) give generally very good approximations at high temperature. The DOS of the investigated materials has been calculated by Marco Bernasconi at the UMB using the density functional theory (DFT) [79]. They have been reported in Figure 77 for amorphous SiO_2, $Ge_2Te_2Sb_5$, $In_4In_1Te_3$ and Pt. For the InSbTe alloy, the cubic zinc blend phase with composition $In_4Sb_3Te_1$ (IST(431)) is closer to the experimental composition $InSb_{0.8}Te_{0.2}$ than the IST(312) compound in the cubic phase with octahedral bonding geometry. In order to have a better interpretation we reported all the data together within the same plot in Figure 78. It thus appears that the DOS for IST, GST and Pt overlap quite well

with approximately the same cut-off frequency (Brilloin zone). However we can note that the second peak in the DOS of Pt, between 150 and 200 cm^{-1}, is not covered by the DOS of IST. More particularly, the DOS for SiO_2 is largely different from that of IST and PT. It is thus expected to have the higher resistance at the interface between IST and SiO_2 and between GST and SiO_2.

The contact resistance at the interface between Si and thermal SiO_2 has been measured by [80] as: $R^{i}_{SiO_2\text{-}Si} = 4.5' 10^{-9}$ $K.m^2.W^{-1}$. We reported in Table 10 the value of the TBR $R_i = R_{Pt/IST} + R_{IST/SiO_2} + R_{SiO_2/Si}$ calculated by either the complete DMM based on the simulated DOS and the simplified DMM based on the Debye approximation.

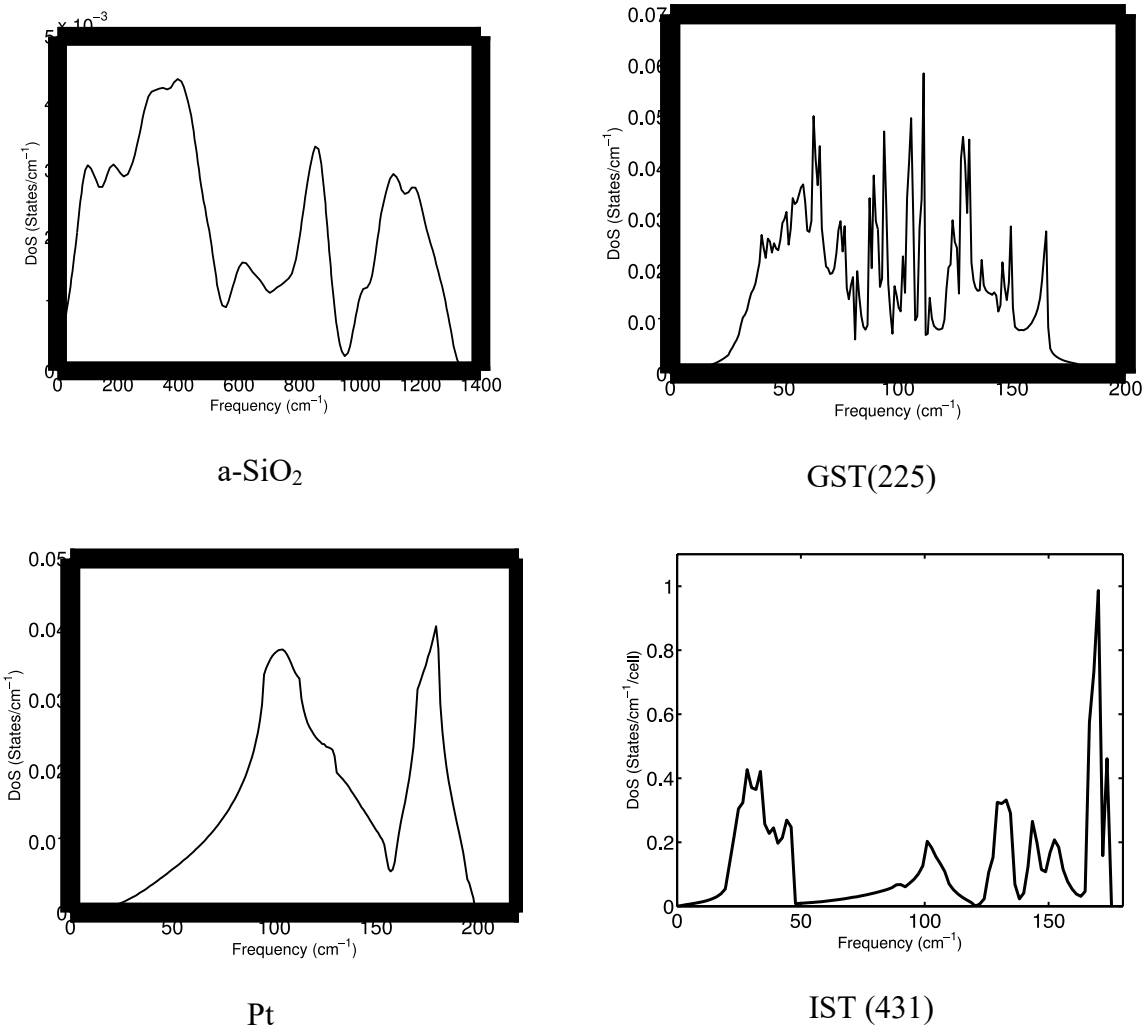

Figure 77: DOS for amorphous SiO_2, GST(225), IST(431) and Pt calculated using DFT (calculations preformed by Marco Bernasconi, UMB).

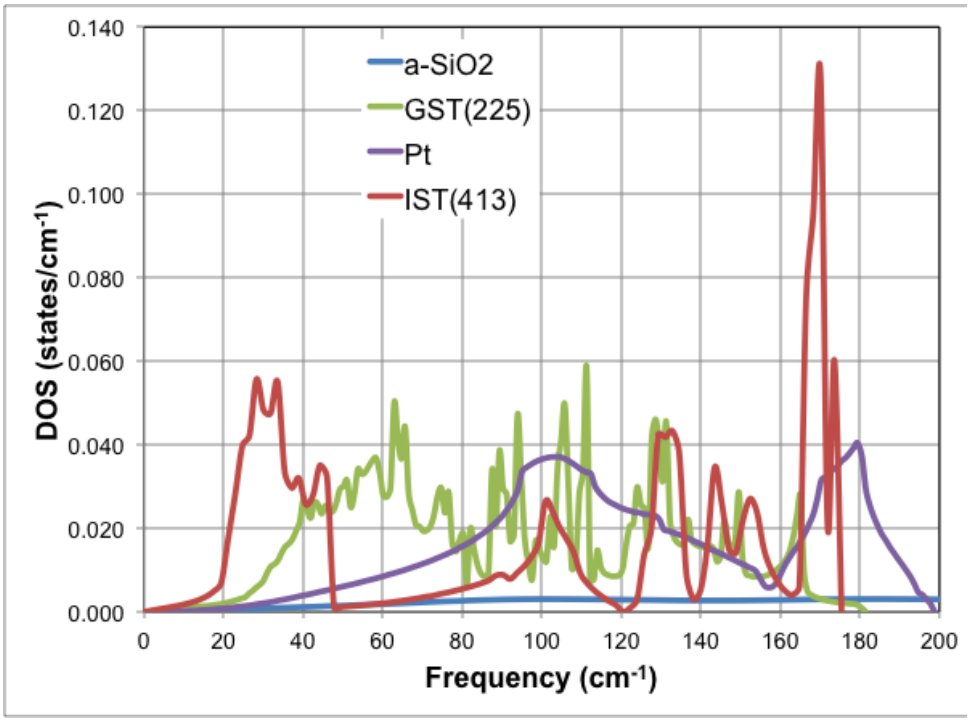

Figure 78: DOS for amorphous SiO_2, GST(225), IST(413) and Pt calculated using DFT. Volume/atom are 30.83 A^3/atom for GST, 27.63 A^3/atom for IST, 15.24 A^3/atom for Pt and 15.85 A^3/atom fo a-SiO_2 (calculations preformed by Marco Bernasconi at the UMB).

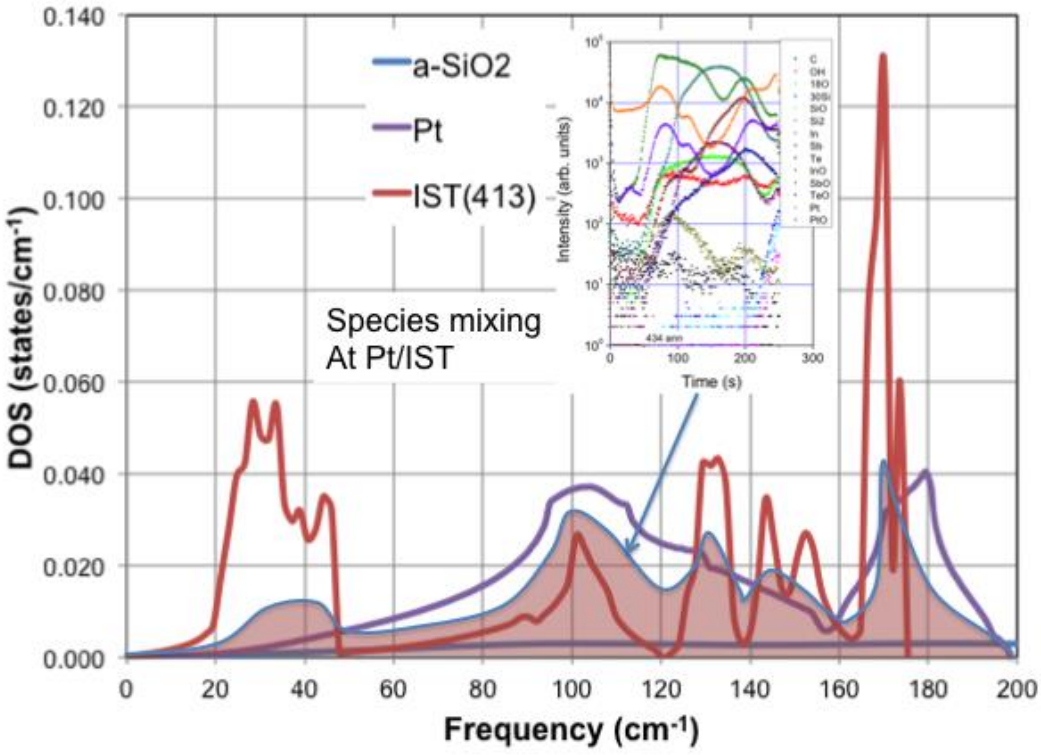

Figure 79: Overlap between DOS of IST and Pt related to the mixing at the interface observed using ToF-SIMS.

	TBR ($m^2.K.W^{-1}$)		
T range (°C)	**DMM/DOS**	**DMM/Debye**	**Measure (20%)**
RT-300	$1.3x10^{-8}$	$1.45x10^{-8}$	$1.x10^{-7}$ → $1.4x10^{-8}$
300-550	$1.3x10^{-8}$	$1.45x10^{-8}$	$1.4x10^{-8}$
550-RT	$1.3x10^{-8}$	$1.45x10^{-8}$	$1.4x10^{-8}$ → $1.0x10^{-7}$

Table 10: theoretical TBR ($R_{IST/SIO2}+R_{IST/Pt}+R_{SiO2/Si}$) using the DMM based on DFT-MD calculations and that on Debye assumption. Comparison with measurement.

Measurements are also reported in Table 6 according to three specific temperature domains. A strong discrepancy appears in the RT-300°C and 550°C-RT ranges, whereas a good agreement is found in the 300°C-500°C.

The TBR found at RT is far from expectations by at least one order of magnitude. In a lesser measure, such a discrepancy has been already observed in our previous studies with GST sandwiched between Pt and SiO_2 [40] but at a lower magnitude. Indeed, the TBR between GST and SiO_2 at RT was measured as $2.5x10^{-8}$ $K.m^2.W^{-1}$ in [41][42]. The total TBR for the Pt/GST/SiO2 stack being about $5x10^{-8}$ $K.m^2.W^{-1}$ at RT [40], it means that the TBR at the GST-Pt interface is about $2.5x10^{-8}$ $K.m^2.W^{-1}$. We found a comparable value ($2.3x10^{-8}$ $K.m^2.W^{-1}$) between GST and Al at RT, using the picoseconds time resolved thermoreflectance [78]. In addition, we can also cite that exactly the same value was found at RT by Reifenberg et *al*. [53] at the interface between GST and TiN.

However, the discrepancy between measurements and theoretical predictions at RT are larger in the case of the Pt/IST/SiO2 stack. The Debye temperature for GST (225) and IST (413) are very close (meaning the cut-off frequency is nearly the sale as evidenced in Figure 77) and the DOS are also very similar. This suggests first that the TBR should not be very different at both interfaces in the Pt/IST/SiO_2 stack than that measured for the Pt/GST/SiO_2 stack. Therefore, the only reason that could be invoked to explain such discrepancy relates to either the roughness or the adhesion between films, or both. Indeed, both the roughness (see

[56][57][58][59]) and the adhesion (see [73][74][75][76][77][78]) strongly influence the TBR value.

Measured roughness is quite low and does not involve significant constriction of the heat flux line at the nanoscale that could explain such high TBR. In addition, the data obtained using the 3ω method, although proving a linear dependence, do not exhibit a significant higher change of the TBR.

It has been observed that there is a positive effect of the mechanical adhesion strengths in order to enhance the heat transfer between two layers. Let us remind that chemical bounding at the interface is strongly related to adhesion strength. In other words, bounding enhance phonon transport/transfer at the interface. Based on the results obtained until now, it is expected that the thermal contact resistance exponentially decreases with the improved adhesion strength. Therefore, it is also expected to have weak bounding between Pt and IST or/and between IST and SiO_2.

The species inter-diffusion that has been demonstrated at the interface between Pt and IST has no positive effect on the adhesion between both layers. Indeed, strong chemical bounding would have a limitation effect on chemical diffusion. However, mass diffusion has a positive effect on the participation of anharmonic phonon scattering at high temperature as also theoretically justified by English et *al*. [68]. Indeed, mass diffusion leads to create a mixing interfacial layer with an apparent Debye temperature that can be viewed as an average of the Debye temperature for both materials [67][69][70][71][72]. This mixing can also be viewed as inserting a layer with properties allowing improving the phonon energy transfer at the interface. Thereby, it has been demonstrated that inserting a thin Ti layer between GST and TiN lead to decrease the TBR regarding that at the GST-TiN one [64]. However, this mixing seems to have a beneficial effect only at high temperature, since going back to RT it fully disappears.

As a general comment, we did not discuss about the electronic contribution in the TBR [60]. As demonstrated in others studies, this contribution is weak in the configuration of a metal/semiconductor/dielectric stack.

In conclusion, considering a sharp interface, chemical bonds (or adhesion strength) is the main parameter affecting the TBR value that is pertinent to mention in order explain the discrepancy between DMM predictions and measurements. At high temperature, the creation of a mixing layer is beneficial to the strong decrease of the TBR. This had been also demonstrated in [64] considering a Ti interfacial layer between TiN and GST.

As we demonstrated that the Pt film started to deteriorate from 300°C, we are not able to conclude on the TBR value especially when going back from 550°C annealing temperature to RT. However, as revealed in Figure 76, it was found also comparable values using the 3w method. This seems to demonstrate that mixing has no positive impact on the TBR at low temperature.

In conclusion, the previous analysis on the TBR is summarized in Figure 80.

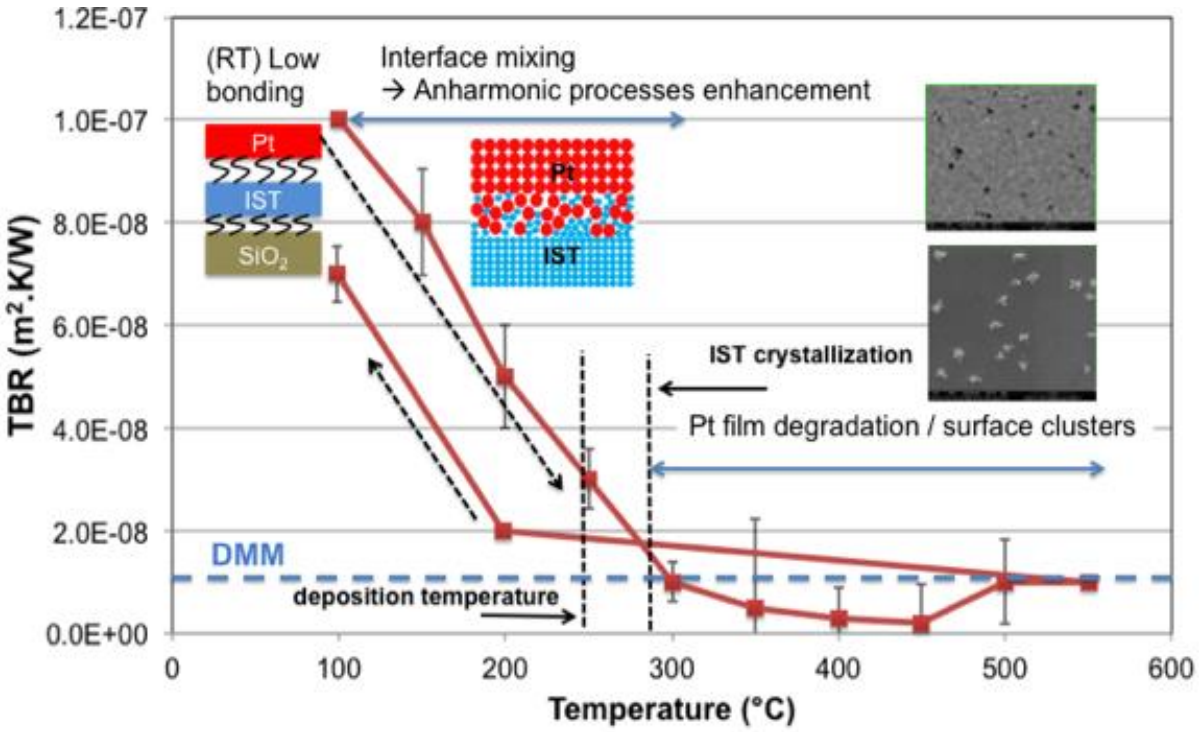

Figure 80: physical interpretation of the phenomenon that occurs at the interfaces when increasing the sample temperature. The value calculated from the DMM is reported on the plot.

4.6 Conclusion

The 3ω measurement demonstrated that the Te content would have a sizeable effect on the thermal conductivity of these IST compounds, which was twofold lower when the former increased from 12 to 17 at. %. As deposited the thermal conductivity of the IST 12% is 0.83 $W.m^{-1}.K^{-1}$ and it is 1.1 $W.m^{-1}.K^{-1}$ when annealed at 480°C (but measurement performed at RT). Likewise, the thermal conductivity of the as deposited IST 17% is 0.39 $W.m^{-1}.K^{-1}$ and it is 0.48 $W.m^{-1}.K^{-1}$ when the sample has been annealed at 480°C (but measurement performed at RT). Using the MPTR experiment, the thermal conductivity of the IST varies from 0.5 $W.m^{-1}.K^{-1}$ to 0.4 $W.m^{-1}.K^{-1}$ when Te content varies from 12 to 17 at. %. However, the trend is still consistent with that observed using the 3ω method (increasing the Te content tends to decrease the thermal conductivity of the IST) but the gap is not as high as observed preliminary. We repeated at least three times the MPTR experiments and we did an average of the results that was always found very similar at low temperature. The observed difference from the results obtained using both methods remains unclear to us. Consistently with literature reports, it was found that increasing the amount of Te content yielded a lower thermal conductivity. As a result, a more thermally resistive alloy could be achieved, which is expected to bring the advantage of a more confined heat flow in a phase change memory device. The electrical resistivity was also higher in the Te-rich alloy than in the Te-poor one, and in any case higher than that of most other Ge-based chalcogenides. Thermal conductivity of In-Sb-Te thin films decreased upon increasing Te content from 12 to 17 at. % regardless of thermal treatment, thus indicating an intrinsic property of the material. Tuning the Te amount is a viable way to achieve a more thermally resistive alloy, which brings the advantage of a more confined heat flow and lower cross talk in a phase change memory device. Thickness dependence was also detected in both IST compounds.

By performing the same measurement, using the 3ω method, on IST layers sandwiched between different dielectrics, we validated that the effect of different neighbouring layers on the thermal conductivity was negligible. This result ensures mainly that the IST structure during deposition on different substrates remains homogeneous. In that way, we thus can assert that there is no column-like structure or grain size variation according to the substrate. At high temperature we observed that the gap between thermal conductivity for both Te contents remains almost identical up to 500°C. When going back to RT, the thermal conductivity of the IST with high Te content (0.4 $W.m^{-1}.K^{-1}$) is far from the value found

using the 3ω. This is even greater for the low Te content where the thermal conductivity (3.5 $W.m^{-1}.K^{-1}$) is found three times higher than that found using the 3ω method. However, the trends are similar: thermal conductivity of the annealed sample decreases when the Te content increases. As demonstrated, we attribute such discrepancies to the fact that Pt capping layer is damaged at high temperature. The origin seems to be mainly related to the formation of crystals at the surface of the IST at high temperature. Finally, we observed that the IST thermal conductivity behaves similarly to the well-known $Ge_2Sb_2Te_5$ alloy (0.55 $W.m^{-1}.K^{-1}$ in the cubic phase) we characterized in previous works. In this regard, the use of IST is still desirable from the technological point of view, as it provides a satisfied confinement of the heat flux and lessens the thermal crosstalk between neighbouring cells; the main advantage of the IST being that the phase-change temperature is higher than that of GST.

The in-situ Raman analysis demonstrated clearly the IST structure evolution according to the temperature increase. At least four specific domains have been identified. The first one starts at 330°C where Te-Te bonds formation are identified. This fits well with the expected crystallization of the IST that is close to 300°C (this could be obviously different according to the Te content in the alloy). Between 400°C and 460°C a better organization of the IST is observed with an enhancement of the Raman peaks linked with InTe binary and Te-Te bounds. When going back to RT, it appears clearly that the structure is not stable. This result is consistent with electrical and thermal conductivity measurements.

Finally, we presented the results we obtained for the thermal boundary resistance between the IST film and surrounding layers. Using the 3ω technique, we showed that the TBR at RT is weakly sensitive to the dielectric nature (SiO_2, Al_2O_3 or Si_3N_4). This result is not surprising since the Debye temperature for these three materials are all higher than that of the IST alloy. However, our observations showed that the choice of dielectric could be a key factor in limiting the heat conduction at the boundaries. Silicon nitride yielded the roughest mean interface (1.9 nm) along with the highest TBR (11.6 $m^2.K.W^{-1}$) among all the as-deposited samples. This finding leads us to conclude that the poor thermal boundary resistance of nitride/IST arises specifically from the coupling of these two materials. On the opposite, alumina achieved the lowest TBR and lowest roughness (1.7 nm), owing to the good coverage and conformality of the atomic layer deposition as compared to sputtering. It must be noted that the lowest TBR was accomplished by the material featuring the highest mismatch between its thermal conductivity and that of IST, i.e. Al_2O_3. This consideration

further validates the hypothesis that the mismatch in thermal conductivity had a negligible effect on the TBR. Finally, the quality of the interface between IST and evaporated silicon oxide was not as good as alumina but much better than silicon nitride. Besides, the TBR of the SiO_2/IST interface is not very different from that obtained for SiO_2/Ge-Sb-Te, which might be an advantage to its implementation in actual devices.

Comparison between TBR obtained either 3ω or MPTR techniques must be carefully addressed since TBR was measured with annealed samples with the first technique whereas in-situ measurements were performed with the second method. Whatever the technique used, we found a good agreement for the measured and theoretical TBR in the 300°C-550°C temperature range. In the RT-300°C and 550°-RT ranges, measurements are far from the theoretical ones based on the diffuse mismatch model using the simulated DOS of the materials. As we explained it, this large deviation could mainly be related to two phenomena:

- The roughness slightly increased with the annealing temperature and measurement obtained using the 3ω technique demonstrated a clear, although weak, correlation with the TBR change;
- The adhesion of the IST film with Pt and/or SiO_2 is weak.

In addition, we could also have concerns with the fact that IST is deposited at a significantly high temperature (280°C). Deposition temperature is a parameter that is rarely taken into account within the TBR analysis.

Those phenomena are not taken into account within the DMM framework. Indeed, DMM assumes a perfectly and ideally strongly bounded interface. Trying to model the roughness influence as well as the bound strength effects on the TBR go beyond the objectives of this work. A strong perspective is thus to have access to the adhesion between layers in order to validate our assumptions. This could be done using the nano-indentation technique.

4.7 References

Materials properties

General database

[1] *Handbook of condensed matter and materials data,* W. Martienssen and H. Warlimont Edidors, Spinger Berlin Heidelberg New York, 2005.

[2] *Materials Science and Engineering Handbook,* Ed. James F. Shackelford & W. Alexander Boca Raton, CRC Press LLC, 2001.

[3] Simmons, G., and H. Wang, 1971, *Single Crystal Elastic Constants and Aggregate Constants* (MIT, Cambridge, MA).

α-Al_2O_3

[4] M. D. Groner, F. H. Fabreguette, J. W. Elam, and S. M. George, *Low-Temperature Al2O3 Atomic Layer Deposition,* Chem. Mater. **16**, 639 (2004).

[5] D. G. Cahill, S. M. Lee and T. I. Selinder, *Thermal conductivity of κ-Al2O3 and α-Al2O3 wear-resistant coatings,* Journal of Applied Physics **83**, 5783 (1998).

[6] P. E. Hopkins, R. N. Salaway, R. J. Stevens, and P. M. Norris, *Temperature-Dependent Thermal Boundary Conductance at Al/Al_2O_3 and Pt/Al_2O_3 interfaces,* International Journal of Thermophysics **28**, 947, (2007).

[7] A. Cappella, J.-L. Battaglia, V. Schick, A. Kusiak, C. Wiemer and B. Hay, *High temperature thermal conductivity of amorphous Al_2O_3 thin films grown by low temperature ALD*, Advanced Engineering Materials **15**, issue 11, 1046-1050 (2013).

Pt

[8] A. P. Caffrey, P. E. Hopkins, J. M. Klopf, and P. M. Norris, *Microscale Thermophys. Eng.* **2005**, *9*, 365.

α-SiO_2

[9] J. P. Reifenberg, D. L. Kencke, and K. E.Goodson, *IEEE Electron Device Letters* **2008**, *29*, 1112.

[10] D. T. Dekadjevi, C. Wiemer, S. Spiga, S. Ferrari, M. Fanciulli, G. Pavia and A. Gibaud, *Appl. Phys. Lett.* **2003**, *83*, 2148.

[11] T. Yamane, N. Nagai, S.- I. Katayama, and M. Todoki, *J. Appl. Phys.* **2002**, *91*, 9772.

α-Si_3N_4

[12] S.-M. Lee and David G. Cahill, *Heat transport in thin dielectric films*, J. Appl. Phys. 81 (6), 1997**.**

[13] B. L. Zink, F. Hellman, *Specific heat and thermal conductivity of low-stress amorphous Si–N membranes*, Solid State Communications 129 (2004) 199–204.

[14] B. Yu, D. Chen, Y. Li and Y. Jia, *Predictions of high-pressure structural, electronic and thermodynamic properties of α-Si_3N_4*, Acta Metall. Sin.(Engl. Lett.), Vol.25 No.2 pp131-140 April 2012.

[15] A. J. Griffin, Jr. and F. R. Brotzen, P J. Loos, *The effective transverse thermal conductivity of amorphous Si_3N_4 thin films*, J. Appl. Phys. 76 (7), 1994

IST (312)

[16] R. Fallica, T. Stoycheva, C. Wiemer, and M. Longo, *Structural and electrical analysis of In–Sb–Te-based PCM cells*, Phys. Status Solidi RRL, 1–5 (2013)

[17] R. Fallica, C. Wiemer, T. Stoycheva, E. Cianci, M. Longo, Huu T. Nguyen, J.-L. Battaglia, *Thermal properties of In-Sb-Te films and interfaces for phase change memory devices*, Microelectronics Engineering **120**, 3–8 (2013).

Raman spectroscopy

[18] K. Ersching, C.E.M. Campos, J.C. de Lima, T.A. Grandi, S.M. Souza and P.S. Pizani, *X-ray diffraction, Raman and photoacoustic studies of InSb nanocrystals*, Materials Chemistry and Physics **122**, 528-532 (2010).

[19] S.J. Park, M.H. Jang, S.-J. Park, M.-H. Cho and D.-H. Ko, *Characteristics of phase transition and separation in a In-Ge-Sb-Te system*, Applied Surface Science **258,** 9786-9791 (2012).

[20] J. Lee, S. Park, J. Kim, C. Yang, S. Kim, C. Seok, J. Park and E. Yoon. *Comparative analysis of oxide phase formation and its effects on electrical properties of*

SiO_2/InSbmetal-oxide-semiconductor structures, Thin Solid Films **520,** (16) 5382-5385 (2012).

[21] RRUFF Database, available on the internet at the site <http ://rruff.info/>.

[22] K.S. Andrikopoulos, S.N. Yannopoulos, G.A. Voyiatzis, A.V. Kolobov, M. Ribes, and J. Tominaga, *Raman scattering study of the a-GeTe structure and possible mechanism for the amorphous to crystal transition*, J. Phys.: Condens. Matter **18** 965-979 (2006).

[23] J. Tominaga and N. Atoda, *Study of the crystallization of GeSTte films by raman spectroscopy,* Jpn. J. Appl. Phys. **38** (3B) L322-L323 (March 1999).

[24] F.L. Faita, C.E.M Campos, K. Ersching and P.S. Pizani, *Structural, thermal and vibrationnal characterization of mechanical alloyed $In_{50}Te_{5,}$* Materials Chemistry and Physics **125,** 257-262 (2011).

[25] B.K. Rai, H.D. Bist, R.S. Katiyar, K.-T. Chen and A. Burger, *Controlled micro oxidation of CdTe surface by laser irradiation : A micro-spectroscopic study*, Journal of Applied Physics **80** 477 (1996).

[26] B.H. Torrie, *Raman spectrum of tellurium,* Solid State Communications **8** 1899 (1970).

[27] M. Yin and A. Krier, *InSb grown on $Cd_{0,955}Zn_{0,045}Te$ by liquid phase epitaxy,* Infrared physics & Technology **58,** 47-50 (2013).

[28] M.A. Nizametdinova, *Raman spectrum of InTe and TISe single crystals,* Physica Status Solidi (b) **97** (1) K9-K12 (January 1980).

[29] M. Emziane, J.C. Bernède, J. Ouerfelli, H. Essaidi and A. Barreau, *A novel method for preparing alpha-In2Te3 polycrystalline thin films*, Materials Chemistry and Physics **61** (3) 229-236 (November 1999).

[30] T.D. Golding, P.R. Boyd, M. Martinka, P.M. Amirtharaj, J.H. Dinan, S.B. Quadri, D.R.T. Zahn and C.R. Whitehouse, *Molecularbeamepitaxial growth and characterization of In_2Te_3,* J. Appl. Phys. **65** 1936-1941 (1989).

[31] E. Finkman and J. Tauc, *Lattice dynamics of tetrahedrally bonded semiconductors containing ordered vacant sites,* Physical Review B **11** (10) 3785-3793 (1975).

[32] S.M. Souza, D.M. Triches, J.C. de Lima, T.A. Grandi, and R.S. de Biasi, *Structural, optical and photoacoustic study of Sb_2Te_3 prepared by mechanical alloying*, Physica B : Condensed Matter **405** (13) 2807-2814 (2010).

[33] G.C. Sosso, S. Caravati, and M. Bernasconi, *Vibrational properties of crystalline Sb_2Te_3 from first principles*, J. Phys. : Condens. Matter **21** 6pp (2009).

[34] W. Richter and C.R. Becker, *A raman and far-infrared investigation of phonons in the rhombohedral V2-VI3 compounds Bi_2Te_3, Bi_2Se_3, Sb_2Te_3 and $Bi_2(Te_{1-x}Se_x)_3$ ($0 < x < 1$), $(Bi_{1-y}Sb_y)_2Te_3$ ($0 < y < 1$),* Physica Status Solidi (b), **84** (2) 619-628 (December 1977).

[35] M.R. Golobostanfard, H. Abdizadeh, S. Mohammadi and M.A. Baghchesara, *Carbon nanotube/indium tin oxide hybrid transparent conductive film : Effect of nanotube diameter,* Solar Energy Materials and Solar Cells **132** 418-424 (2015)

[36] M. Jothibas, C. Manoharan, S. Ramalingam, S. Dhanapandian, S. Johnson Jeyakumar and M. Bououdina, *Preparation, characterization, spectroscopic (ft-ir, ft-raman, uv and visible) studies, optical properties and kubo gap analysis of In_2O_3 thin films,* Journal of Molecular Structure **1049** 239-249 (2013).

[37] W. Yin, J. Su, M. Cao, C. Ni, S. G. Cloutier, Z. Huang, X. Ma, L. Ren, C. Hu and Wei, *$In(OH)_3$ and In_2O3 micro/nanostructures : Controllable NaOac-assisted microemulsion synthesis and raman properties*, J. Phys. Chem. C **113** 19493-19499 (2009).

[38] B.S. Naidu, M. Pandey, V. Sudarsan, R.K. Vatsa and R. Tewari. *Photoluminescence and raman spectroscopic investigations of morphology assisted effects in Sb_2O_3,* Chemical Physics Letters **474** 180-184 (2009).

GST (225)

[39] H.-K. Lyeo, G. G. Cahill, B.-S. Lee, J. R. Abelson, M.-H. Know, K.-B. Kim, S. G. Bishop and B.-K. Cheong, Appl. Phys. Lett. **89**, 151904 (2006).

[40] J.-L. Battaglia, A. Kusiak, V. Schick, A. Cappella, C. Wiemer, M. Longo and E. Varesi, *Thermal characterization of the SiO_2-$Ge_2Sb_2Te_5$ interface from room temperature up to 400 °C*, J. App. Phys. **107**, 044314 (2010)

[41] J. Lee, E. Elah Bozorg-Grayeli, Z. Li, J. P. Reifenberg, M. Asheghi, and K. E. Goodson, Proceedings of Itherm, 2010, 5501412, pp. 1–6.

[42] J. Lee, Z. Li, J. P. Reifenberg, S. Lee, R. Sinclair, M. Asheghi and K. E. Goodson, *Thermal conductivity anisotropy and grain structure in $Ge_2Sb_2Te_5$ films*, J. Appl. Phys. **109**, 084902 (2011).

IST Thermal conductivity analysis

[43] K. S. Siegert, F. R. L. Lange, E. R. Sittner, H. Volker, C. Schlockermann, T. Siegrist and M. Wuttig, *Impact of vacancy ordering on thermal transport in crystalline phase-change materials*, Rep. Prog. Phys. **78**, 013001 (2015).

[44] D. G. Cahill, S. K. Watson and R. O. Pohl, *Lower limit to the thermal conductivity of disordered crystals*, Phys. Rev. B**46** 802–8 (1992).

[45] J. Graebner, B. Golding and L. Allen, *Phonon localization in glasses*, Phys. Rev. B **34** 5696–701 (1986).

[46] W. P. Risk, C. T. Rettner and S. Raoux , *Thermal conductivities and phase transition temperatures of various phase-change materials measured by the 3ω method*, Appl. Phys. Lett. **94** 101906 (2009).

[47] T. Matsunaga, R. Kojima, N. Yamada, K. Kifune, Y. Kubota, Y. Tabata and M. Takata *Single structure widely distributed in a GeTe–Sb2Te3 pseudobinary system: a rock salt structure is retained by intrinsically containing an enormous number of vacancies within its crystal*, Inorg. Chem. **45** 2235–41 (2006).

[48] M. N. Schneider, T. Rosenthal, C. Stiewe and O. Oeckler, *From phase-change materials to thermoelectrics*? Z. Krist. **225** 463–70 (2010).

[49] T. Rosenthal, M. N. Schneider, S. Christian, M. Döblinger and O. Oeckler, *Real structure and thermoelectric properties of gete-rich germanium antimony tellurides*, Chem. Mater. **23** 4349–56 (2011).

[50] T. Siegrist, P. Jost, H. Volker, M. Woda, P. Merkelbach, C. Schlockermann and M. Wuttig, *Disorder-induced localization in crystalline phase-change materials*, Nature Mater. **10** 202–8 (2011).

General considerations on TBR

[51] E. T. Swartz and R. O. Pohl, *Thermal boundary resistance*, Rev. Mod. Phys. **61**, 605 (1989).

[52] D. G. Cahill, W. K. Ford, K. E. Goodson, G. D. Mahan, A. Majumdar, H. J. Maris, R. Merlin, and S. R. Phillpot, *Nanoscale thermal transport*, J. Appl. Phys. **93** (2), (2003).

[53] J. P. Reifenberg, K.-W. Chang, M. A. Panzer, S. Kim, J. A. Rowlette, M. Asheghi, H.-S. P. Wong, and K. E. Goodson, *Thermal Boundary Resistance Measurements for Phase-Change Memory Devices*, IEEE Elect. Dev. Lett **31** (1), (2010).

Diffuse Mismatch (DMM)

[54] S. Pettersson and G. D. Mahan, *Theory of the thermal boundary resistance between dissimilar lattices*, Phys. Rev. B **42** (12), 7386 (1990).

[55] J. C. Duda, J. L. Smoyer, P. M. Norris and P. E. Hopkins, *Extension of the diffuse mismatch model for thermal boundary conductance between isotropic and anisotropic materials*, App. Phys. Lett. **95**, 031912 (2009).

TBR and Roughness

[56] D. H. Santamore and M. C. Cross, *Effect of Phonon Scattering by Surface Roughness on the Universal Thermal Conductance*, Phys. Rev. Lett. **87** (11), 115502-1, (2001)**.**

[57] K. Termentzidis and P. Chantrenne, *Nonequilibrium molecular dynamics simulation of the in-plane thermal conductivity of superlattices with rough interfaces*, Phys. Rev. B **79**, 214307 (2009).

[58] P. E. Hopkins, L. M. Phinney, J. R. Serrano, and T. E. Beechem, *Effects of surface roughness and oxide layer on the thermal boundary conductance at aluminum/silicon interfaces*, Phys. Rev. B **82**, 085307 (2010).

[59] R. Prasher, *Predicting the Thermal Resistance of Nanosized Constrictions*, Nano Lett. **5** (11), (2005).

TBR Metal-Dielectric

[60] E. S. Landry and A. J. H. Mc Gaughey, *Thermal boundary resistance predictions from molecular dynamics simulations and theoretical calculations*, Phys. Rev. B **80**, 165304 (2009).

[61] H.-K. Lyeo and D. G. Cahill, *Thermal conductance of interfaces between highly dissimilar materials*, Phys. Rev. B **73**, 144301 (2006).

[62] R. J. Stevens, A. N. Smith, P. M. Norris, *Measurement of Thermal Boundary Conductance of a Series of Metal-Dielectric Interfaces by the Transient Thermoreflectance Technique*, J. Heat Transfer **127**, 315-322 (2005).

TBR Electron-Phonon

[63] A. Majumdar and P. Reddy, *Appl. Phys. Lett.* **2004**, *84*, 4768.

Interfacial layer

[64] J.-L. Battaglia, A. Kusiak, A. Saci, R. Fallica, A. Lamperti, C. Wiemer, *Effect of a thin Ti interfacial layer on the thermal resistance of $Ge_2Sb_2Te_5$-TiN stack*, Appl. Phys. Lett. **105**, 121903, (2015).

[65] Z. Liang and H.-L. Tsai, *Effect of thin film confined between two dissimilar solids on interfacial thermal resistance*, J. Phys.: Condens. Matter **23**, 495303 (2011).

[66] Z. Liang, H.-L. Tsai, *Reduction of solid–solid thermal boundary resistance by inserting an interlayer*, Int. J. Heat and Mass Transfer **55**, 2999–3007 (2012).

Interface mixing

[67] M. Hu, X. Zhang, D. Poulikakos , C. P. Grigoropoulos, *Large ''near junction'' thermal resistance reduction in electronics by interface nanoengineering*, Int. J. Heat and Mass Transfer **54**, 5183–5191 (2011)

[68] T. S. English, J. C. Duda, J. L. Smoyer, D. A. Jordan, and P. M. Norris, *Enhancing and tuning phonon transport at vibrationally mismatched solid-solid interfaces*, Phys. Rev. B **85**, 035438 (2012).

[69] R. J. Stevens, L. V. Zhigilei, P. M. Norris, *Effects of temperature and disorder on thermal boundary conductance at solid–solid interfaces: Nonequilibrium molecular dynamics simulations*, Int. J. Heat and Mass Transfer **50**, 3977–3989 (2007).

[70] P. E. Hopkins, K. Hattar, T. Beechem, J. F. Ihlefeld, D. L. Medlin and E. S. Piekos, *Reduction in thermal boundary conductance due to proton implantation in silicon and sapphire*, Appl. Phys. Lett. **98**, 231901 (2011).

[71] D. Kechrakos, *The role of interface disorder in the thermal boundary conductivity between two crystals*, J. Phys.: Condens. Matter **3**, 1452 (1991).

[72] T. Beechem, S. Graham, P. Hopkins and P. Norris, *Role of interface disorder on thermal boundary conductance using a virtual crystal approach*, Appl. Phys. Lett. **90**, 054104 (2007).

Bounding

[73] R. Prasher, *Acoustic mismatch model for thermal contact resistance of van der Waals contacts*, Appl. Phys. Lett. **94**, 041905 (2009).

[74] L. Hu, L. Zhang, M. Hu, J.-S. Wang, B. Li and P. Keblinski, *Phonon interference at self-assembled monolayer interfaces: Molecular dynamics simulations*, Phys. Rev. B **81**, 235427 (2010).

[75] M. Shen, W. J. Evans, D. Cahill and P. Keblinski, *Bonding and pressure-tunable interfacial thermal conductance*, Phys. Rev. B **84**, 195432 (2011).

[76] P. K. Schelling, S. R. Phillpot, and P. Keblinski, *Kapitza conductance and phonon scattering at grain boundaries by simulation*, J. Appl. Phys., **95**, 11, (2004).

[77] M. D. Losego, M. E. Grady, N. R. Sottos, D. G. Cahill and P. V. Braun, *Effects of chemical bonding on heat transport across interfaces*, Nature Mat. DOI: 10.1038/NMAT3303, (2012).

[78] J.-L. Battaglia, V. Schick, C. Rossignol, A. Kusiak, I. Aubert and C. Wiemer, *Thermal resistance at Al-$Ge_2Sb_2Te_3$ interface*, Appl. Phys. Lett. **102**, 181907 (2013).

Density of States (DOS)

[79] J. H. Los, T.D. Kuehne, S. Gabardi, and M. Bernasconi, *First principles study of the amorphous In3 SbTe2 phase change compound*, Phys. Rev. B **88**, 174203 (2013).

SiO2/Si interface

[80] O. W. Käding, H. Skurk, and K. E. Goodson, *Thermal conduction in metallized silicondioxide layers on silicon*, Appl. Phys. Lett. **65**, 1629 (1994)

Conclusions and Perspectives

The use of chalcogenide materials for electronic memory applications has gained much attention due to their strong variation in the electrical and optical properties. In the current PhD thesis work, the novel InSbTe alloys have been studied. They are expected to overcome the drawbacks of the most known GeSbTe alloys for phase change memory devices. This work has been done thanks to a collaboration between two laboratories: MDM (Italy) and I2M (France) and financial support from Université Franco-Italienne, scholarship Vinci. It is also in relation with the Synapse European project. The research carried out in this work is focused mainly on thermal characterization of InSbTe alloys. Two alloys with different Te content: at.12% and 17% have been investigated in order to observe its influence on the thermal conductivity and the total thermal resistance at the interfaces of layers.

In order to perform this characterization, two techniques: the 3-ω available at MDM and the Modulated Photothermal Radiometry (MPTR) available at I2M were used. In this framework, the measurement were carried out by using 3-ω on as-deposited and annealed samples at RT, while in-situ measurements were realized using MPTR, from RT up to 550^0C. Due to the high thermal budget received by the samples, several complementary methods of structural and chemical analysis including XRD, XRR, SEM, Raman and Tof-SIMS have been applied for checking the state of the samples during the thermal characterizations.

The measured thermal conductivity of IST is higher in crystalline phase than in the amorphous one for the two Te contents. Some discrepancies were noticed in results obtained from the two thermal characterization techniques. At RT, the thermal conductivity of the annealed IST was found much higher using MPTR than that measured by 3-ω. This difference can be attributed to the fact that Pt capping layer in MPTR is damaged at high temperature.

The results obtained from the two thermal characterization techniques demonstrate that the thermal conductivity of IST decreases when increasing the Te content. Increasing the Te content could thus lead to a more thermally resistive alloy, which is expected to bring the advantage of a more confined heat flow and limiting the thermal cross-talk in the phase change memory device.

The study of the effect of the neighbours layers on the thermal conductivity of the IST alloy was carried out using 3-ω method. It shows, that this influence is negligible in the case of SiO_2, Al_2O_3 or Si_3N_4 dielectrics.

The thermal boundary resistance between the IST film and the neighbours layer was measured. Using the 3ω technique, the TBR at RT was shown weakly sensitive to the nature of dielectric material (SiO_2, Al_2O_3 or Si_3N_4). Using the MPTR, the TBR was measured in-situ. The results are in good agreement with theoretical values from DMM model in the 300°C-550°C temperature range. In the RT-300°C and 550°-RT ranges, the measured values are far from the theoretical ones. This difference can be explained by increasing roughness of the films during annealing and a weak adhesion of the Pt capping layer on the IST film which are not taken into account in the theory.

The subject of this study is very important for the design and technology of PRAM. The thermal metrology at high temperature and nanoscale represents an important challenge and obtaining of reliable results is very delicate. For this reason, some perspectives issuing from the present work can be addressed.

Concerning in-situ MPTR experiments, an improvement of the thermal/optical transducer on the top of the sample should be researched. The thickness of the Pt transducer can be optimized and/or another kind of metallic layer can be tested. The objective being the application of a transducer having a good adhesion to the studied film, supporting high temperatures and characterized by appropriate for PTR optical properties. On the other hand, a better control of the noble gas atmosphere (Ar, N_2) should be ensured in order to prevent the samples from any oxidation at high temperatures.

Concerning the adhesion of the Pt transducer used in the present study, the evaluation of this parameter, using for example the scratch test or the nano-indentation technique will be useful in comprehension of the results on TBR.

Finally, application of other techniques for thermal characterization can be considered. We think about the thermoreflectance technique permitting to explore the shorter characteristic times and thus to reach the TBR by measuring one sample without estimation of the total thermal resistance of different thicknesses samples. It would give the possibility to confirm the reliability of the results obtained in this work.

Appendix A: Methodologies for structural and interface characterization.

6.1 Introduction

As mentioned in chapter 1, various thin film / multilayered materials are currently being developed and produced for use in functional devices such as Phase Change Memory (PCM). These materials (PCMs) undergo structural and chemical changes during annealing at high temperature (~ 550°C in the present work). Besides the methods described in chapter 2 for the thermal characterization, it remains necessary to examine the influence of thermal annealing on the structural and chemical changes. For that reason, several complementary experimental methods have been implemented to achieve a thorough structural and chemical characterization of the films grown using MOCVD. Those methods are assumed to meet the following conditions:

- They are non-destructive,
- They allow to deal with relative and absolute measurements of the parameters of interest,
- They allow measurements of the variation at the micro and nano scales,

We present in this annex the following techniques that are well suited for the micro scale analysis of annealed PCMs:

- Scanning Electron Microscopy and X-ray microanalysis by Energy Dispersive Systems (EDS) and Wavelength Dispersive Systems (WDS).
- X-Ray Diffraction and Reflectivity Techniques
- Raman spectroscopy
- ToF-SIMS spectroscopy

6.2 Scanning Electron Microscopy and X-ray microanalysis.

A Scanning Electron Microscope (SEM) typically relies on a set of three electromagnetic lenses / condensers to focus on the sample surface (Figure 81) a thin beam of accelerated primary electrons (from less than 1kV up to 30 kV). The spatial lateral resolution permitted by our Field Emission Gun Environmental Scanning Electron Microscope (FEG E-SEM), a FEI QUANTA 250 FEG, is about 1.5 nm. This high resolution compared to that of an optical

light microscope is due to (1) the wavelength of the electron beam which is thousands of times smaller than the wavelength of light and (2) the much smaller numerical aperture of the electron beam.

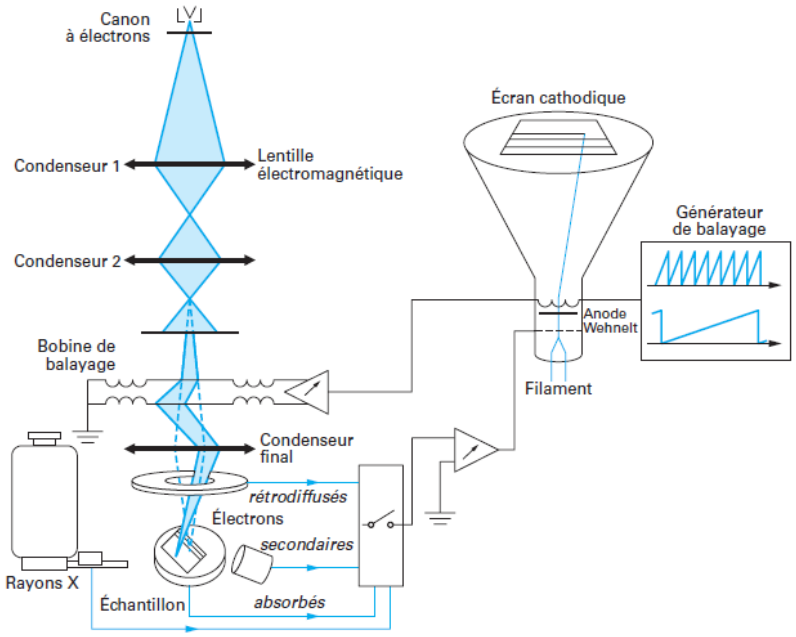

Figure 81: Schematic drawing of a SEM. From Paqueton and Ruste (2006).

As the incident primary electron beam penetrates / hits the sample surface, it undergoes elastic and inelastic interactions leading to various emissions including but not limited to:

- An emission of Secondary Electrons (SE) of low energy (< 50eV),
- An emission of BackScattered Electrons (BSE) whose energy is close to that one of the incident primary beam,
- An emission of energetic photons (X-rays) that form (1) a continuous non characteristic spectrum due to the slowdown of the incident electrons by the electric field of the atoms and (2) X-rays characteristic of every type of atoms present in the sample (which are produced by the ionization of the atoms by the incident electrons and their subsequent relaxation). Such characteristic X-rays are used for the elemental chemical analysis.

Every type of emission is collected by dedicated detector(s). The SE emission produces images of topographic contrast, while the BSE emission leads to images of both topographic

and atomic number contrasts of the scanned surface. On our equipments, the X-rays emission listed above can be detected / collected by two systems:

- an EDAX Energy Dispersive Spectrometer (EDS) equipped with an Apollo XL Silicon Drift Detector (SDD) of 30 mm^2, with a resolution of about 130eV,
- an EDAX TEXS Wavelength Dispersive System (WDS) with a much finer resolution ranging from a few eVs to about 20eVs depending on the elements of interest.

Both X-rays spectrometers can be used for qualitative and quantitative analysis of the sample chemical composition, weight % and/or atomic %, (spectrum, line-scan and X-ray cartography. Note that WDS X-ray elemental (2D) maps cannot be quantified because the information is collected on a single eV channel. Any chemical element, starting at bore (B) can be detected.

Samples can be observed in high vacuum (chamber pressure ~ 10^{-4} Pa), in low vacuum (pressure < 200 Pa), or in ESEM mode (pressure < 2600 Pa, in conditions referred to as "wet conditions"). The analysis can be performed on a fitted Peltier stage (from -25°C to 55°C) , or on a fitted hot stage (up to 1000°C).

For illustrative purposes Figure 82 and Figure 83 show at different magnifications IST 435 and IST 438 (50 nm) samples, both coated with Pt. Figure 82 and Figure 83 were collected using our Beam Deceleration Module (BDM) and the vCD detector (low voltage, low Current Detector). The BDM facility actually allows increasing the lateral resolution and the topographical contrast at very low voltages. In this operating mode, low angle BSE, generally not seen by the vCD detector, are actually collected. These figures allowed us to appraise the degree of alteration of the films surface after annealing at high temperature.

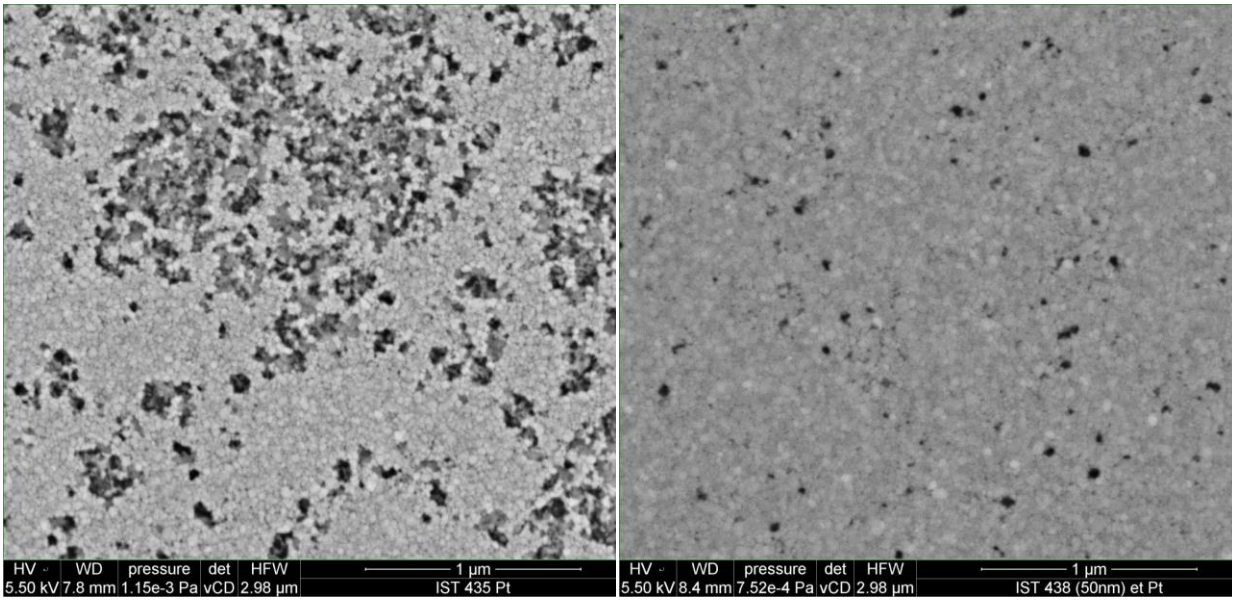

Figure 82: On the left, IST 435 coated with Pt. On the right, IST 438 (50nm) coated with Pt. The samples surface is clearly altered, especially for sample IST 435

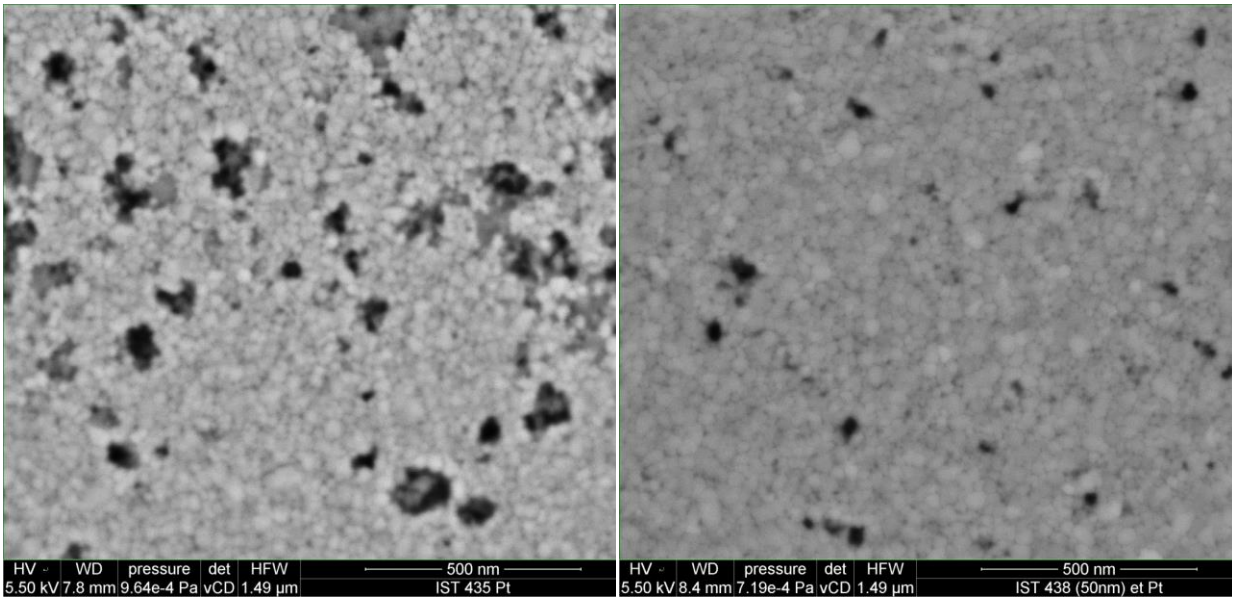

Figure 83: Same as in Figure 82 at a higher magnification.

Figure 84 shows an example of EDS spectrum in the case of sample IST 434 as-deposited. Using a ZAF matrix correction, we quantified this EDS spectrum and found the following composition: $In_3Sb_{2.6}Te_{0,62}$ which shall be compared to the theoretical (known) composition of this sample: $In_3Sb_{2.7}Te_{0.8}$.

Given the resolution of about 130 eV of this Energy Dispersive System, this quantification is quite satisfying.

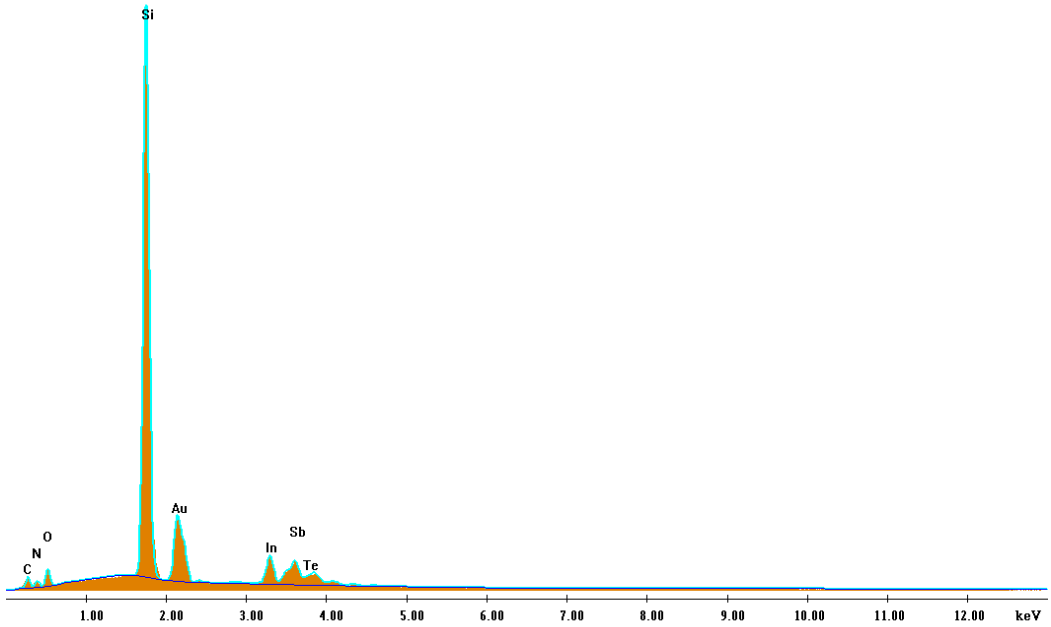

Figure 84: X-ray elemental chemical microanalysis: EDS spectrum of sample IST 434 « as deposited » coated with a thin film of Au.

Figure 85 is another example of SEM views (taken at room temperature) in the case of a sample of IST 439 which was previously heated in situ at 460°C.

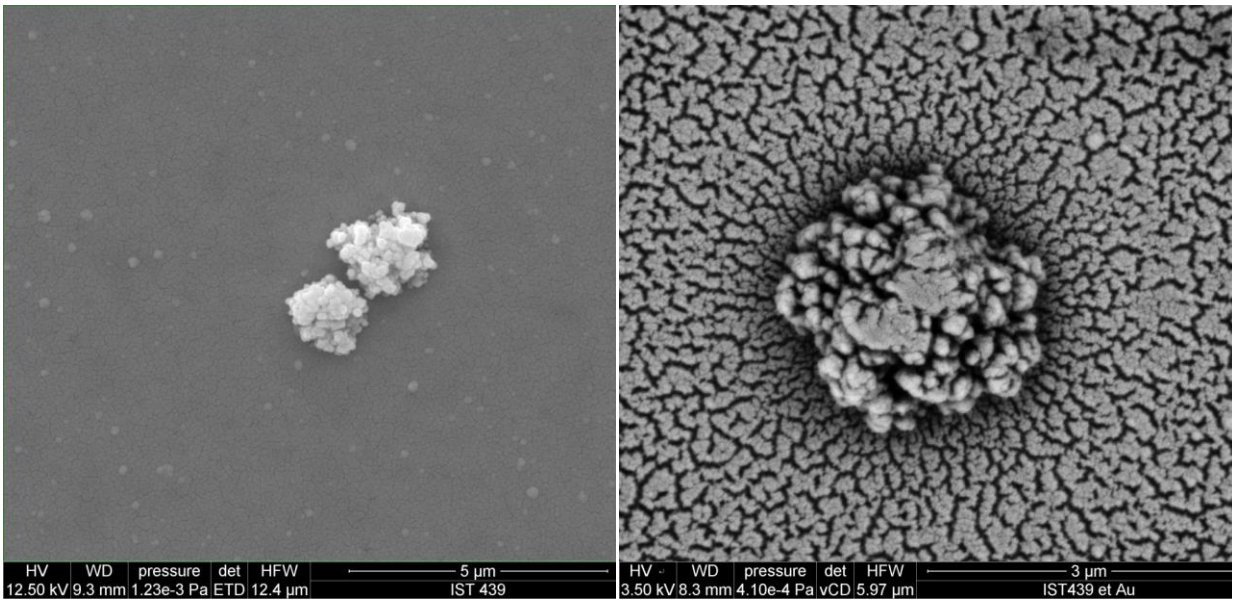

Figure 85: Observation at room temperature of sample IST 439 which has been heated in situ up to 460°C. On the left, SE image using our standard Everhart-Thornley

Detector (magnification x24,000). On the right, low angle BSE image using our vCD detector in BDM mode (magnification x50,000). The sample is coated with 5 nm of Au.

Figure 86 shows an example of EDS and WDS spectra measured on a micron-sized grain that typifies sample IST 439 (previously heated in situ at 460°C) (see left view in Figure 85). .

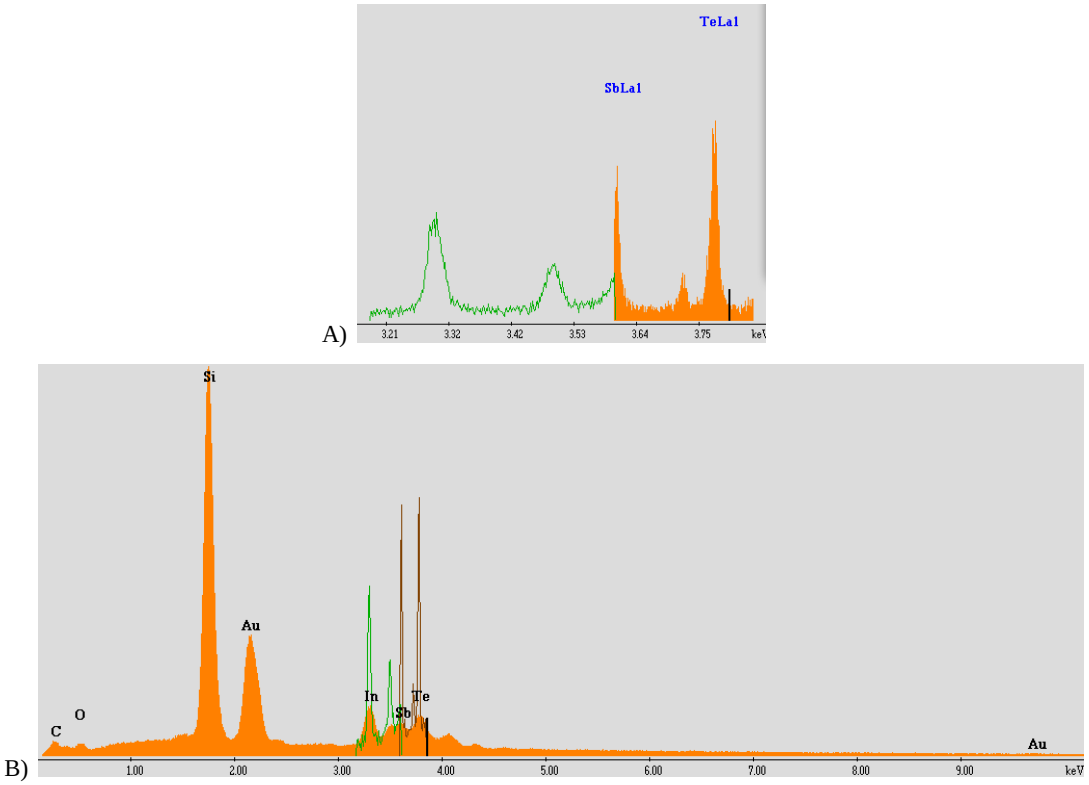

Figure 86: IST 439 sample which was previously heated in situ up to 460°C. WDS spectrum (A) and EDS spectrum (B) acquired on a GRAIN (see right view in Figure 85. The WDS spectra acquired with diffractor 1 (orange) diffractor 5 (green) are not normalized. In view B), the EDS and WDS spectra are superimposed, which allows to clearly see the much higher resolution of the WDS system. .

The pure intensities, required for a quantification with standards, were measured with the EDS and the WDS systems on pure samples (Sb) and composite (InAs, HgTe, et SiO2) certified for X-ray micro-analysis.

The quantification obtained from the EDS spectrum gives a chemical composition of $\mathbf{In_3Sb_{0,7}Te_3}$ for the micro-sized grain shown in the right view of Figure 85. The quantification obtained with the much higher resolution of the WDS spectrometer gives a composition of $\mathbf{In_3Sb_1Te_{2.3}}$, which confirms that after an in-situ heating (460°C), IST samples include locally a phase of highly crystallized $\mathbf{In_3Sb_1Te_2}$ (as confirmed independently by XRD analyses).

This clearly illustrates that **the high resolution of a WDS system is perfectly suited to study IST samples**.

References:

Paqueton H, Ruste J, 2006. Microscopie électronique á balayage - Principe et équipement. Techniques de l'Ingénieur, **P865**, 16 p.4

6.3 X-Ray Diffraction and Reflectivity Techniques

X-Ray Diffraction (XRD) is widely used for estimating the parameters of the crystalline structure (interplanar spacings) of the most varied samples. From this information (interplanar spacings), the different (crystalline) phases making a sample can be identified. Relying, for example, on a Rietveld method, the relative proportions of every phase can be also inferred (the result remains semi-quantitative).

The underlying principle of X-Ray Diffraction (XRD) is this one : when a monochromatic and parallel X-ray beam interacts with matter, a coherent radiation showing the same wavelength is emitted in all directions (Rayleigh diffusion). Due to the presence of crystallographic cells, these coherent waves interfere (this is the diffraction phenomenon). The directions where interferences are constructive (referred to as X-ray diffractions peaks) follow an empirical law called the Bragg's law :

$$\text{Bragg's law: } n\lambda = 2d\sin\theta$$

where, the integer n is the diffraction order, λ is the wavelength of the incident X-ray, d is the distance between two crystallographic planes (the d-spacings), and θ is the angle of incidence of the X-ray.

The Bragg's law is geometrically justified by Figure 87. Interferences are at a maximum for a deviation 2θ (at which the additional distance $2d\sin\theta$ travelled by the ray that hits the lower plane introduces a phase shift multiple of 2π and is therefore multiple of λ). The wavelength λ is known, θ (or rather the deviation 2θ) is measured and can the d-spacing is deduced.

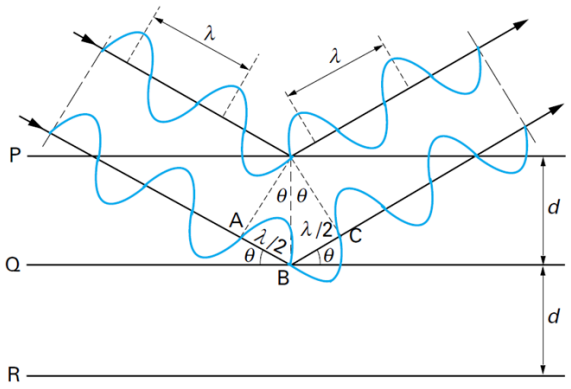

Figure 87: X-Ray diffraction. From Broll (1996).

Grazing incidence (GI) XRD was actually performed. The X-ray tube is positioned at a low incidence angle. The diffracted beam is collected by a fixed circle shaped detector (Schick, 2011). This technique is well suited to the analysis of thin polycrystalline films. Here samples are not reduced to powder and are not isotropic. The monocrystalline Si substrate (100) is specifically positioned / orientated so that its peaks do not show up on the X-ray diffractogram. GIXRD patterns were simulated by the Rietveld method and the crystallographic phase composition, the lattice parameters, the dimension of the diffracting domains and the presence of preferential orientations were analyzed.

In this study, besides X-Ray Diffraction (XRD), X-Ray reflectivity (XRR) was also implemented.

XRR is a technique used to characterize surfaces, films and multilayers. If an X-ray beam impinges upon an interface where the electron density changes, some x-rays are reflected in the specular direction, while others rest go through the interface and may next impinge on a deeper interface where the same process of specular reflection can occur. Because interfaces are not perfectly sharp, the reflected intensity can change with the incident angle.

These variations can be analysed to obtain the density profile of the interface normal to the surface, layer thicknesses....

Figure 88 shows experimental and simulated of selected XRR patterns for a dielectric/IST/dielectric stack.

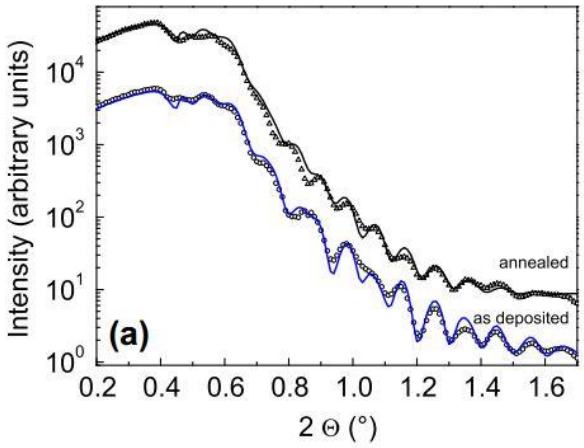

Figure 88: XRR patterns for a dielectric/InSbTe/dielectric stack. XRR data (symbols) and simulations (lines) of as deposited and 480°C annealed 70 nm thick IST sandwiched between SiO_2.

In this study, a parallel beam of Cu Kα source, 40kV was used. XRR spectra were collected using a NaI scintillator detector. The simulation of the XRR curves was performed by modeling the stack structure with different layers of appropriate thickness, roughness and electronic density and by performing a simulation based on weighted least square minimization. The simulations are based on the matrix formalism corrected by a Croce-Nevot factor.

References:

Broll, N. 1996. Caractérisation de solides cristallisé par diffraction X. Techniques de l'Ingénieur, PE1 080.
Schick V, 2011. Caractérisation d'une mémoire a changement de phase. Mesure de propriétés thermiques de couches minces à haute température. Thèse, Université de Bordeaux.

6.4 Raman Spectroscopy

Raman spectroscopy is a powerful technique designed to observe the vibrational modes of the molecules that form the matter. The sample is subjected to an electromagnetic radiation that interacts with the matter, which leads to a quantitative information on this vibrational dynamics (Barbillat et al., 1999). The main part of the photons that form the incident radiation is reflected or absorbed. Part of the incident beam is also scattered in all directions due to the polarizability of the molecules. The scattered radiation includes :

- a major component with the same frequency ν_0 as that of the incident/ radiation corresponding to elastic diffusion (Rayleigh diffusion),

- a much smaller component diffused in a non elastic manner with frequencies $\nu_0 + \nu_V$ (anti-Stokes diffusion) and $\nu_0 - \nu_V$ (Stokes diffusion) where ν_V the denotes the vibration frequencies of Raman active molecules. This inelastic diffusive process is referred the Raman effect (Barbillat et al., 1999).

The Raman effect is complementary to Fourier Transform Infra Red (TF-IR) spectroscopy. In both cases, vibrations are studied but the selections rules for identifying a specific vibration differ. The principle of Raman spectroscopy may be introduced in an intuitive manner as follows: the electric field of an incident (monochromatic) laser beam deforms the molecules of the sample: the barycenter of the electrons slightly shifts from that one of the positive charges, hence the appearance of an electric dipole moment that radiates elastically in all directions. The thermal agitation/motion of the molecules and their internal vibrations modulate this Rayleigh radiation introducing therefore wavelength shits (or Raman sits) characteristic of the bonds of the molecules.

Our Raman system couples a Renishaw Raman confocal INVIA spectrometer to an optical Leica DM2500 microscope. This Raman system is fitted with two exciting laser radiations : 532 nm and 785 nm. These laser sources are vertically polarized. Our system allows studying Stokes diffusion only.

Raman spectra can be collected from small volumes (at best micron-sized or slightly less in the O_x and O_y Cartesian directions and a few hundred on nm in the z-direction). Such a spatial resolution is comparable to that one reached in X-ray microanalysis (EDS and WDS).

A distinctive feature of our Raman equipments is the ability to run Raman spectroscopy in-SEM (532 nm). Only three groups in France (I2M included) own this utility referred to as SEMSCA (for Scanning Electron Microscope Structural and Chemical Analyzer).

References:

Barbillat, J., Bougeard, D., Buntinx, G., Dehlaye, M., Dhamelincourt, P., & Fillaux, F. 1999. Spectrométrie Raman. Techniques de l'Ingénieur, P 2 865, 31 p.

6.5 Time of Flight Secondary Ion Mass Spectroscopy (ToF-SIMS)

Time of Flight Secondary Ion Mass Spectroscopy (ToF-SIMS) is a type of the mass spectrometry often used for thin film and surface characterization. This technique offers several advantages such as: all elements can be detected, a high mass resolution with trace level sensitivity, submicron spatial resolution and sub-nm depth resolution. Therefore, in the

framework of InSbTe thin films, ToF-SIMS was performed to observe the concentration of the chemical species as a function of depth as well as their migration into the surface layer of the material that may occur during thermal cycle measurement from room temperature up to 550^0 C.

The experiments are carried out by sputtering the specimen from the surface with a sputtering ion beam (current few nA) and analyzing the exposed surface with a Ga focused primary ion beam (current few pA). The secondary ions produced in the sputtering process are emitted from the sample surface into the time-of-flight mass spectrometer. In the Figure , the principle of Tof-SIMS technique is shown. The majority of the emitted particles is neutral in charge, and cannot be detected by the spectrometer but a fraction is positively or negatively charged.

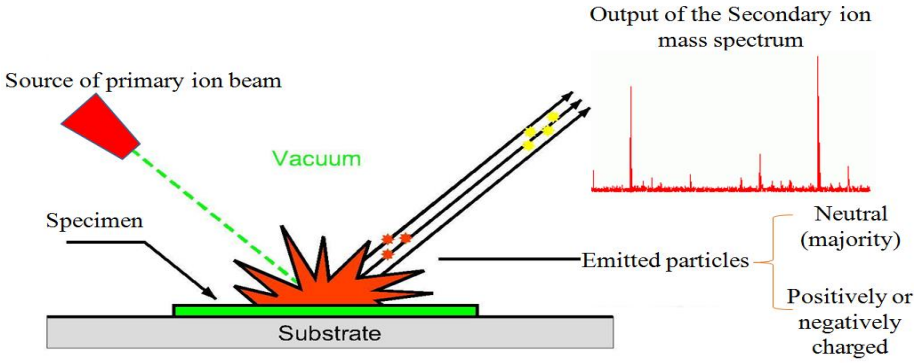

Figure 9: Decription of ToF-SIMS principle

These secondary ions are dispersed in time according to their velocities which are proportional to their mass/charge ratio m/q. The m/q ratios of these secondary ions are measured by a mass spectrometer in order to determine the elemental, isotopic, or molecular composition of the exposed surface to a depth typically less than 2 nm. In order to observe a depth profiling contribution, O_2+ and Cs+ are widely used as sputtering ions species at impact energies from 250 eV to 2 keV (up to 15 keV for bulky specimens), depending on the analysis task. As the sensitivity of a SIMS measurement is strongly depending on the ion bombardment conditions and the composition of the matrix, non-reactive ion beams such as Ar+, Xe+, and Ga+ generate secondary ion yields from matrices, which are orders of magnitude lower than those measured with reactive beams such as O_2+ or Cs+. Because of the shallow structures requirement, the use of low energy primary ion beams to minimize ion-beam-induced mixing of the sample and to improve depth resolution is necessary. In general,

secondary ions of at least the dopant and a signal corresponding to the substrate (matrix signal) are measured as a function of time during the depth profile. The ratio of the measured dopant signal strength to the strength of the matrix signal is then converted to a dopant concentration by applying a normalization factor called a relative sensitivity factor. Likewise, the profile shape of the dopant is derived by also applying a calibrated/measured sputter rate to the measured data curves.

Sufficient mass separation of the secondary ion signals is required so that the ion species monitored during a depth profile are in fact due to the dopant. The relation of the ability to separate two atoms or molecules of the same charge at mass m, which differ in mass by the amount Δm is described by the mass resolution as follow:

$$SIM - mass - resolution = \frac{m}{\Delta m}$$

The secondary ions always travel along the same path through the analyzer and moreover the mass separation is only due to flight time differences from the sample to the detector, therefore, a ToF analyzer is capable of detecting any secondary species of given polarity over a mass range 1 amu to some 10 kamu and $m / \Delta m$ up to 15,000 in parallel.

In this work ToF-SIMS was employed to characterize the chemical composition of a phase change material throughout their entire thickness with extremely high depth resolution (<1 nm) and high sensitivity depending on the experimental conditions and on the chemical species under analysis. ToF SIMS depth profiles were acquired in negative polarity on an ION-TOF IV instrument using Cs+ ions at low energy for sputtering and Ga+ ions at 25 keV for analysis.

References:

Caractérisation d'une mémoire à changement de phase. Mesure de propriétés thermiques de couches minces à haute température. Thèse de Vincent Schick, Université de Bordeaux, 2011.

Appendix B: Growth MOCVD technique for In-Sb-Te thin film deposition

Since the great contribution of semi-conducting industry, along with the use of thin films (and recently wires) at the nanoscale for electronic application, the need of a powerful growth technique has always been a challenge task. Indeed, a key enablement to scale the confined-cell PCM device architecture is the use of conformal deposition processes. In the recent years, the Metal-Organic Chemical Vapor Deposition (MOCVD) has emerged as a well-established manufacturing technology that has a demonstrated capability of uniformly fabricating thin films of high quality and excellent conformality at a high throughput rate. In addition, MOCVD shows several advantages over sputtering for alloy/dopant tuning in that it offers run-to-run tuning of composition through flow control, as compared to the need to obtain new sputtering targets and to re-setup and qualifying the tool for sputtering; thus greatly speeding the development process and reducing the cost. In this study, the In-Sb-Te layer thin films were deposited on Si substrates by mean of the powerful MOCVD growth technique. The term MOCVD accounts for two main aspects: *) It is a specific method that was initially developed from the Chemical Vapor Deposition (CVD), **) Uses organometallic compounds and hydrides as precursors for the deposition process. By heating the substrate to the growth temperature, the precursors are dissociated inside the growth chamber, thus making the reacting species available for the vapour → solid transition under super saturation conditions. Ultra-pure precursors are used to preserve the final purity of the grown film/structure. Particularly, MOCVD reactors are viable for large scale deposition at industrial level, where the so called showerheads deposition chamber can process up to fifty-eight 2'' or three 12'' diameter wafers at a time.

The self-assembled thin films growth was performed by mean of a thermal MOCVD AIX 200/4 reactor at the laboratory MDM (belonging to the CNR, Italy).

The MOCVD reactor at CNR-IMM, Agrate Brianza, Italy

The MOCVD facility was manufactured by AIXTRON SE (Germany as shown in the Figure) having several advantages such as: up to four precursor lines plus two lines for dopants, infrared-lamps heated growth chamber; 4 ” wafer substrate holder with rotating disk (to enhance uniformity); nitrogen gas glove box; and vacuum pumping system. In order to perform the MOCVD process, the precursors are heated up to a suitable given temperature and pressure when they are inside a proper container (bubbler), in which the carrier gas (nitrogen) is compelled to flow, thus becoming saturated with the precursor vapors. The bubbler temperature, internal pressure, and gas mass flow ultimately set the concentration and amount of precursor that are taken into account during the reaction. The mixture of carrier gas and precursor vapors is used to transport the reactants from the bubbler to the deposition chamber, controlling the molar flow of each precursor with a precision of the order of μ mol/min.. The whole MOCVD deposition process is controlled by a computer and. This reactor is well-adapted to for both thin films and nanowires materials. Instead of using hydrogen, hydrides, or ammonia, the use of N_2 brings the advantage of simpler leading safer operating conditions. However, as N_2 is inert at the growth temperature employed, the activation rate of the deposition is remarkably lower than normal.

In the present work, In-Sb-Te films were grown at CNR-IMM, Agrate Brianza, Italy by MOCVD at 260^{o}C, 10^4 Pa, on a Si (100) wafer 550 μm thick, covered with several dielectric materials such as SiO_2, Si_3N_4, Al_2O_3, obtained by thermal oxidation of the substrate. Electronic grade solution trimethylindium $In(CH_3)_3$, trisdimethylaminoantimony $(N(CH_3)_2)_3Sb$ and diisopopyltelluride $(C_3H_7)_2Te$ were used as In, Sb and Te metal-organic

precursors, respectively. We obtained two compositions of In-Sb-Te: $In_3Sb_{2.7}Te_{0.8}$ (A) and $In_3Sb_{2.5}Te_{1.2}$ (B), corresponding to a Te content of 12 at.% and 17 at.%, respectively. The thermal characterization required having different In-Sb-Te film thicknesses.